2020

Reconstruction of the 2018 Anak Krakatau collapse using PlanetScope imaging and numerical modeling

Davide Saviano

RECONSTRUCTION OF THE 2018 ANAK KRAKATAU COLLAPSE USING
PLANETSCOPE IMAGING AND NUMERICAL MODELING

By

Davide Saviano

A THESIS

Submitted in partial fulfillment of the requirements for the degree of

MASTER OF SCIENCE

In Geology

MICHIGAN TECHNOLOGICAL UNIVERSITY

2020

This thesis has been approved in partial fulfillment of the requirements for the Degree of MASTER OF SCIENCE in Geology.

Department of Geological & Mining Engineering & Sciences

Thesis Co-Advisor: *Dr. Simon A. Carn*

Thesis Co-Advisor: *Dr. Gianluca Groppelli*

Committee Member: *Dr. Roohollah R. Askari*

Department Chair: *Dr. John S. Gierke*

Table of Contents

Abstract

The study was focused on the Anak Krakatau sector collapse that occurred on 22 December 2018 in the Sunda Strait (Indonesia). The goal of the study was to monitor and analyze changes of the volcanic edifice and to try to understand causes that may have predisposed and triggered the sector collapse.

The use of different remote sensing techniques allowed the acquisition of thermal data, SO_2 emission data, structural data and the identification and analysis of the eruptive events that occurred on Anak Krakatau in the period from 1° January 2016 to 28 February 2019. The acquisition of 1221 thermal data and 1156 SO_2 emission data was performed using MODIS and OMI. Anak Krakatau began a new and intense activity phase on 30 June 2018 which continued in the following six months preceding the lateral collapse of the SW flank of the volcanic edifice, reaching its climax in September. The activity subsequently followed a decreasing trend, ending shortly after the collapse. The thermal data and the use of PlanetScope images allowed the identification of 8 lava flows, 7 of which developed between July and November 2018, exactly in the months that preceded the collapse. Almost all the lava flows affected the SW, S-SW and S slopes of the volcanic cone. These events led to an increase of the lithostatic load on the area subsequently collapsed. Precisely, their volume is equal to 6.8×10^6 m^3. The volumes of all the lava flows were calculated considering an average thickness of 10m, obtaining a total volume equal to 8.2×10^6 m^3. Further analysis of the satellite images highlighted a shift of the summit crater mainly towards the area subsequently collapsed and the generation of different curvilinear fractures which can be grouped in three main strikes' groups: NW-SE; E-W and NNE-SSW. The structures with NW-SE strike agree with regional tectonics while those with E-W and NNE-SSW direction delimit the subsequent collapse. What has been observed indicates that there were precursory signs of structural instability. Finally, based on the collected data, bibliographic information regarding the extent of caldera-forming ignimbrite and deep surveys, it was possible to create the first pre-collapse 3D model representing the area present before the 2018 collapse. This model is a key element for a possible simulation of the sector collapse that occurred on Anak Krakatau.

The model allows to test three hypotheses of possible predisposing causes in future studies: 1) Increase of the lithostatic load on the SW side of the volcano generated by the deposition of all products erupted during the last phase of activity, considering also its high inclination (> 20 °); 2) Dike intrusion into the shallow portion of the volcanic edifice; 3) External factors which are common predisposing causes that influence the stability of the volcanic slopes such as a failure plane, zones of weakness, hydrothermal activity and mechanical weakening by alteration.

The study shows that the collapse of Anak Krakatau could have been anticipated through continuous monitoring of the volcano and its activity using different remote sensing techniques. Finally, we believe that the combination of 3D models, representing areas with signs of instability, and remote sensing techniques is an important method for predicting potentially disastrous events, and Anak Krakatau is an example.

1 Introduction

Indonesia has over 130 active volcanoes, more than any other nation in the world. Volcanoes constitute the axis of the Indonesian island arc system produced by the northeastward subduction of the Indo-Australian Plate beneath the Eurasian plate. Many of these volcanoes lie along with the two largest Indonesia's islands, Java and Sumatra. These two islands are separated by the Sunda Strait.

One of the most famous volcanos in the world lies in the Sunda Strait with latitudinal values equal to 6.102° S and with longitudinal values equal to 105.423° E, it is Krakatau. This volcano is a caldera, it lies in the Indonesian province of Lampung and this name is also used for the surrounding volcanic island group (Krakatoa Archipelago) comprising four islands: Panjang, Sertung, Rakata and Anak Krakatau. The thesis work was carried out considering the island of Anak Krakatau, a small volcanic island located in the central north of the Krakatau archipelago and it is 157 km from Jakarta. This island is 260 m high, it extends for about 2 km in length and it has a width of 2,40 km. Inside of the island numerous eruptive events and modifications of it have been observed until the southwest flank collapse occurred on 22 December 2018.

Anak Krakatau (or child of Krakatau) is a post-calderic cone and it is very active from the volcanic point of view. The birth of Anak Krakatau is dated 29 December 1927, initially a submarine cone, emerged for the first time from the sea surface in 1928, alternating periods of intense activity with periods of rest in the following decades. This volcano erupted 44 years after the famous Krakatau eruption happened on 26-27 August 1883. The 1883 eruption was a caldera collapse, it was the second largest in Indonesia and one of the two deadliest volcanic events in historic time after the great Tambora eruption (1815). The eruption caused more than 36.000 fatalities, most as result of devastating tsunamis that swept the adjacent coastlines of Sumatra and Java. (Bani et al., 2015).
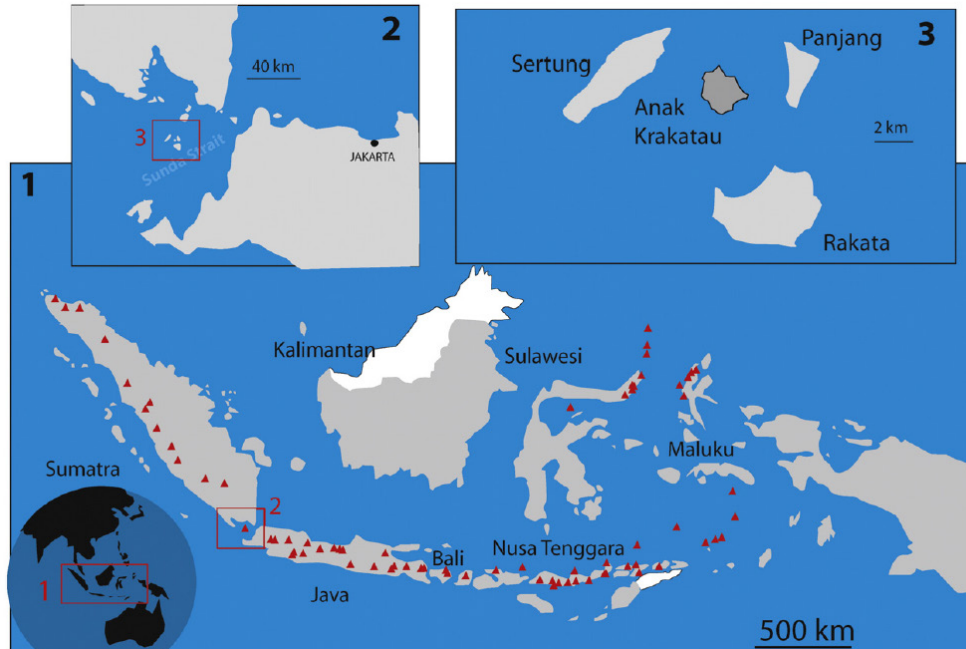
Figure 1: (1), The red triangles show the position of every active volcanoes in Indonesia. (2), Anak Krakatau is located in the Sunda Strait between Sumatra and Java. (3), Anak Krakatau, a new cone that emerged from the sea after the Krakatau island was pulverized by the eruption in 1883 (Bani et al., 2015).

The study was focused on the Anak Krakatau flank collapse occurred on 22 December 2018, precisely the goal of the study was trying to understand the evolutions and the causes that generated it through creating sequential mappings of subsequent events occurred on the island and the generation of a digital pre-collapse 3D model of the analyzed area. We worked in detail considering a time window from 1° January 2016 to 28 February 2019. In this interval we considered all events (eruptions, new fractures, change in island's shape etc) that were observable from Satellite imagines of PlanetScope and we mapped all of these events to try to understand what the trigger of the flank collapse was. Another porpoise of the work was to consider the thermal data and the sulfur dioxide emission data respectively collected from MODIS and OMI within the time window specify before, to detect all events happened on the island (also events not reported by satellite images) in order to build the best trend of the volcanic activity of Anak Krakatau.

2 Geodynamics and geological setting

2.1 Geology of Indonesia

Indonesia is an archipelago of more than 18.000 islands extending more than 5000 km from east to west, it is formed over the past 300 million years by reassembly of fragments rifted from the Gondwana supercontinent that arrived at the Eurasian subduction margin, it is a geologically complex region located at the southeastern edge of the Eurasian continent and it is bordered by tectonically active zones characterized by intense seismicity and volcanism resulting from subduction (Hall, 2009). Indonesia is situated at the boundaries of three major plates: Eurasia, Indo-Australian and Pacific Philippine plates (Hamilton, 1979). The Indo-Australian Plate moves northward and is being subducted beneath the Eurasian Plate (Abdurrachman et al., 2018). The convergence rate of the Indian plate and the Philippine sea plate relative to Eurasia, is respectively 7 and 10 cm/yr; For the Australian plate instead, the convergence rate relative to the Pacific plate is 11 cm/yr (Hall, 2009).
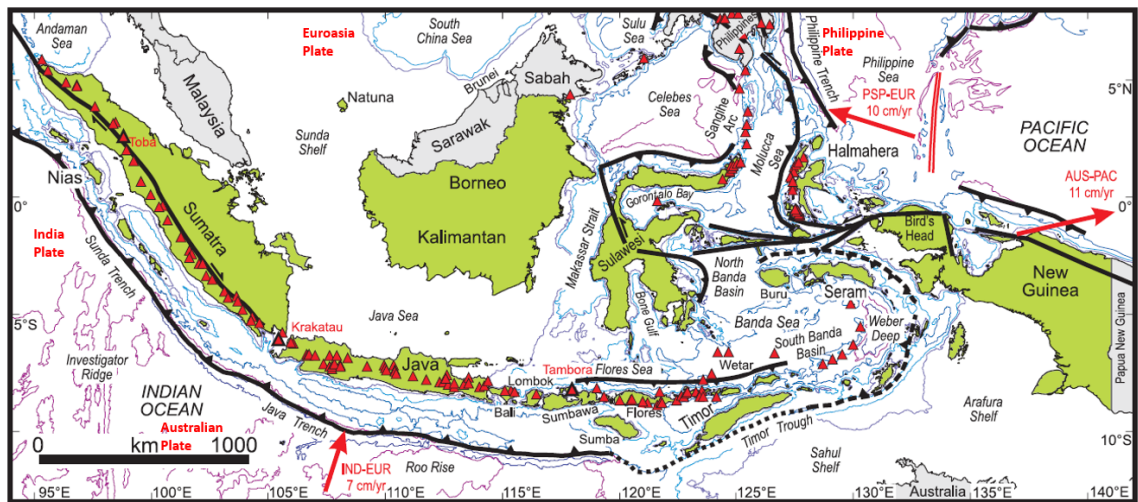
Figure 2: Geography of Indonesia and surrounding regions with the tectonic boundaries and volcanic activity. Indonesia is shaded green; neighboring countries are shaded in grey. The location of the three most famous explosive eruptions known from Indonesia are shown in red. Red arrows show plate convergence vectors for the Indian plate (IND-EUR) and the Philippine Sea plate (PSP-EUR) relative to Eurasia, and for the Australian plate relative to the Pacific plate (AUS-PAC) (Hall, 2009).

The subduction zone is divided in Sumatra and Andaman subduction systems and is one of the most seismically active regions in the world (Engdahl et al., 2007). It is a long convergent belt that extends from the Himalayan front southward through Myanmar, continues south past the Andaman and Nicobar Islands and Sumatra, south of Java and the Sunda Islands, and then wraps around to the north. This trench accommodates the northward motion of the Australian plate into Eurasia and a part of this convergent belt is the subduction zone southwest of Sumatra (McCaffrey, 2009).
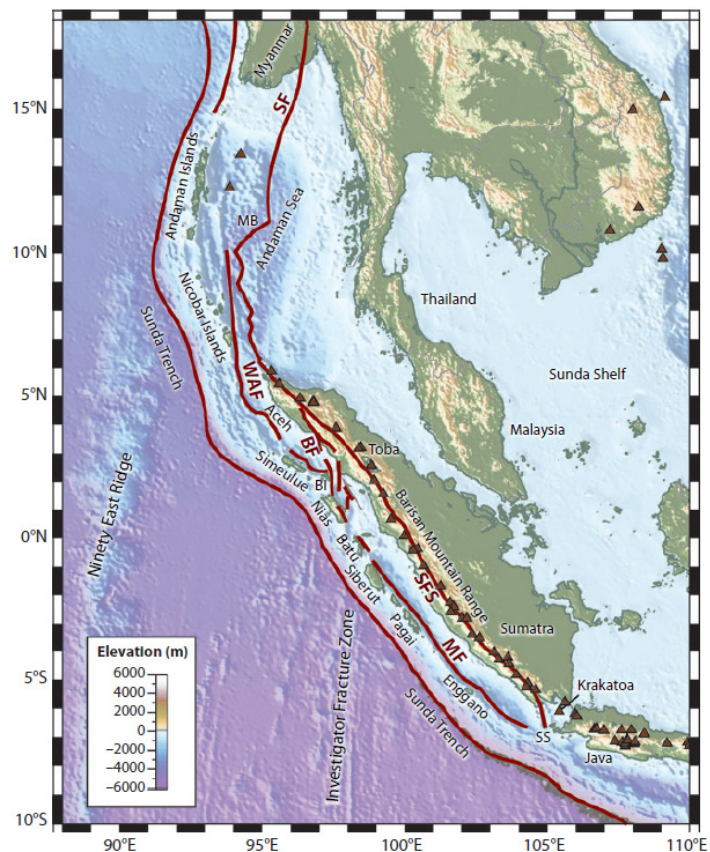
Figure 3: Physiographic map of the Sumatran region. Triangles: active volcanoes; Red lines: faults. Data from the Global Volcanism Program. BI: Banyak Islands; BF: Batee fault; MB: Mergui Basin; MF: Mentawai fault; SF: Sagaing fault; SFS: Sumatran fault system; SS: Sunda Strait; WAF: West Andaman fault (McCaffrey, 2009).

Indonesia can be divided into the western and eastern sides. Western Indonesia is largely underlain by continental crust, but in eastern Indonesia, there is more arc and ophiolitic crust and several young ocean basins (Hall, 2009).

In western Indonesia, the boundary between the Eurasian and Indian plates is the Sunda Trench. Parallel to this in Sumatra there is the right-lateral strike-slip Sumatran Fault (SFZ) which results from the partitioning of oblique plate convergence into normal convergence at the trench and trench-parallel movement further north, due to the presence of the oblique subduction (figure 4) (Hall, 2009). The NW–SE trending Sumatra fault zone (SFZ) is the most pronounced shear zone of the Eurasian plate within the volcanic arc and it accommodates most of the right-lateral stress of the relative plate motion between the Indo-Australian and Eurasian plates and it is seismically active (Schluter et al., 2002). According to (Katili et al., 1967; Natawidjaja et al., 1994) the SFZ is composed of several segments with differing slip rates ranging from 1.1 cm/yr to 2.8 cm/yr (Baroux et al., 1998) and most of these segments are less than 100 km long (Sieh et al., 2000). The SFZ links the Sunda Strait to the Andaman transform fault system in the Andaman Sea (north of the island of Sumatra) and to the south it disappears into the Sunda strait (figure 4) (Huchon et al., 1984).
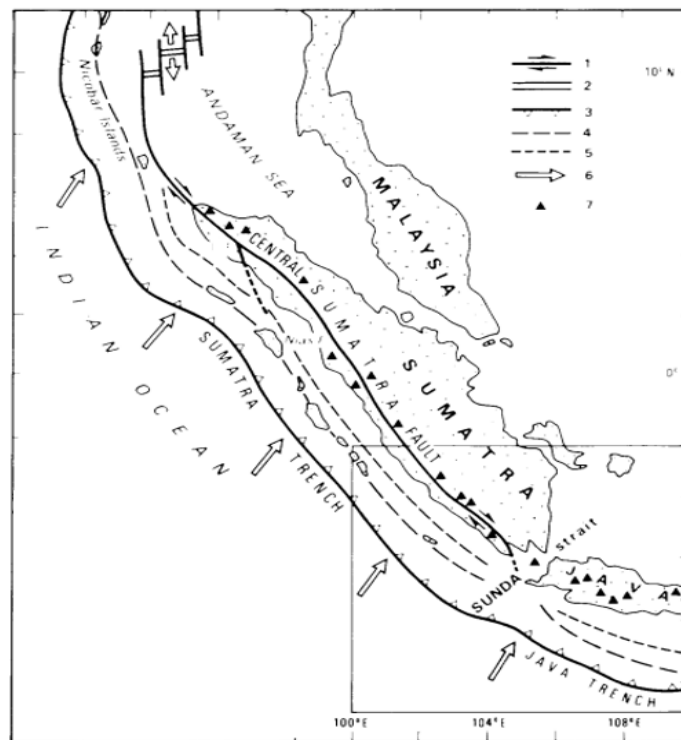

Figure 4: Location of study area and its geodynamic context. (1), strike slip fault; (2), spreading center; (3), subduction trench; (4), axis of outer ridge; (5), axis of fore-arc basin; (6), direction of relative motion; (7), active volcano (Huchon et al.,1984).

As (McCaffrey.,2009) explain, in some cases of oblique subduction where the two plates do not converge at a right angle to the strike of the trench, it requires smaller overall shear force to share the shearing (trench-parallel) component of the relative motion between two separate faults instead of on one fault. In this case of study, one fault is the Subduction thrust and the second fault is the Sumatra fault. The subduction thrust (Sunda trench) and strike-slip fault (Sumatran fault) isolate a wedge of forearc called the Sliver plate (Figure 5). Precisely, the oblique motion of the subducting plate under the overriding plate (Eurasian plate) imparts along-strike shear stress at its base, which can detach the leading edge of the overriding plate forming the wedge of forearc. The Sliver plate slides laterally relative to the upper plate along a strike-slip fault and thrusts over the subducting plate (Huchon et al.,1984; McCaffrey,2009).
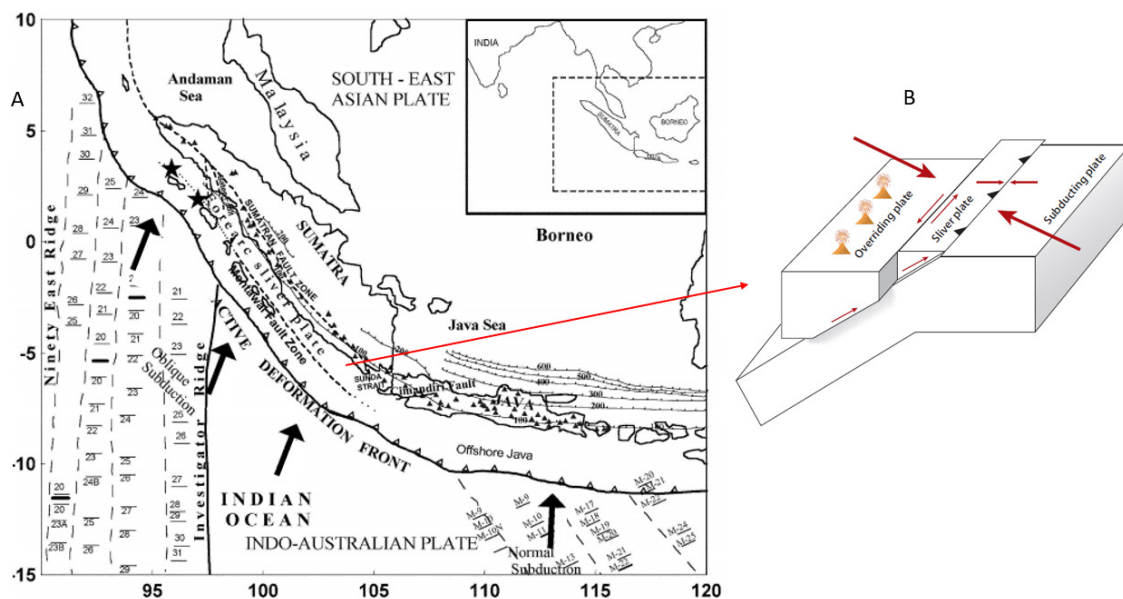
Figure 5: Tectonic sketch of the study area. (A), Tectonic map of the Sumatra–Java trench-arc region in eastern Indian Ocean; Hatched line with numbers indicates depth to the top of the Benioff Zone (after Newcomb et al., 1987); Magnetic anomaly identifications have been considered from (Liu et al, 1983 and Krishna et al., 1983); Magnitude and direction of the plate motion is obtained from (Sieh et al., 2000); Stars show location of the recent major earthquakes (26 December 2004, 28 March 2005); (B), Block diagram showing the geometry of the Sliver plate and its motion under conditions of oblique subduction(Lasitha et al., 2006; McCaffrey, 2009).

The Seismic reflection data (Lasitha et al., 2006) show the forearc Sliver plate which is 300 km wide and reveal also a 600 km long strike-slip fault parallel to the SFZ called the Mentawai Fault Zone (MFZ), just east of Mentawai islands. The MFZ is a zone of weakness that separates the oceanic and continental crust and, considering (Sieh et al, 2000), there are evidence that this system is inactive. Observing the boundary of the Forearc Sliver plate in the Sunda Strait, its motion is thought to be much slower than at its leading edge in the Andaman Sea (Huchon et al., 1984; Curray et al., 1979), and it is norward motion would explain the opening and the extensional patter of the Sunda strait (Diament et al., 1992).

2.2 Sumatra – Java subduction zone

The subduction zone southwest of Sumatra is a convergent boundary between the Indo-Australian plate and the southeastern part of the Eurasia plate (Diament et al., 1992). It is well defined by seismicity and by the volcanic arcs (Sunda arc, Banda arc, the Sangihe arc and Halmahera arc), which stretch about 6000 km from Sumatra to the Molucca Sea (western Pacific Ocean) (Widiyantoro et al., 1997).

The convergence rate of the Indo-Australian and Eurasia plate increases from Sumatra to the East with values between 6.7 cm/yr to 7 cm/yr (Tregoning et al., 1994) and the directions of relative convergence, deduced from the India/Eurasia pole of the global model of (Minster and Jordan., 1978), are N24°E off Java and N23°E off Sumatra. More recently a study of slip vectors of intraplate earthquakes indicates the N-S direction as a new relative convergence direction between the two plates (Jarrard, 1986a; 1986b; Newcomb et al., 1987; McCaffrey, 1991). As a result, the subduction between Java and Sumatra is different; there is a frontal subduction along Java with the development of typical fore-arc basins and there is an oblique subduction along Sumatra, results in partitioning of the convergent motion into thrust and strike-slip faulting (Lasitha et al., 2006; Diament et al., 1992).
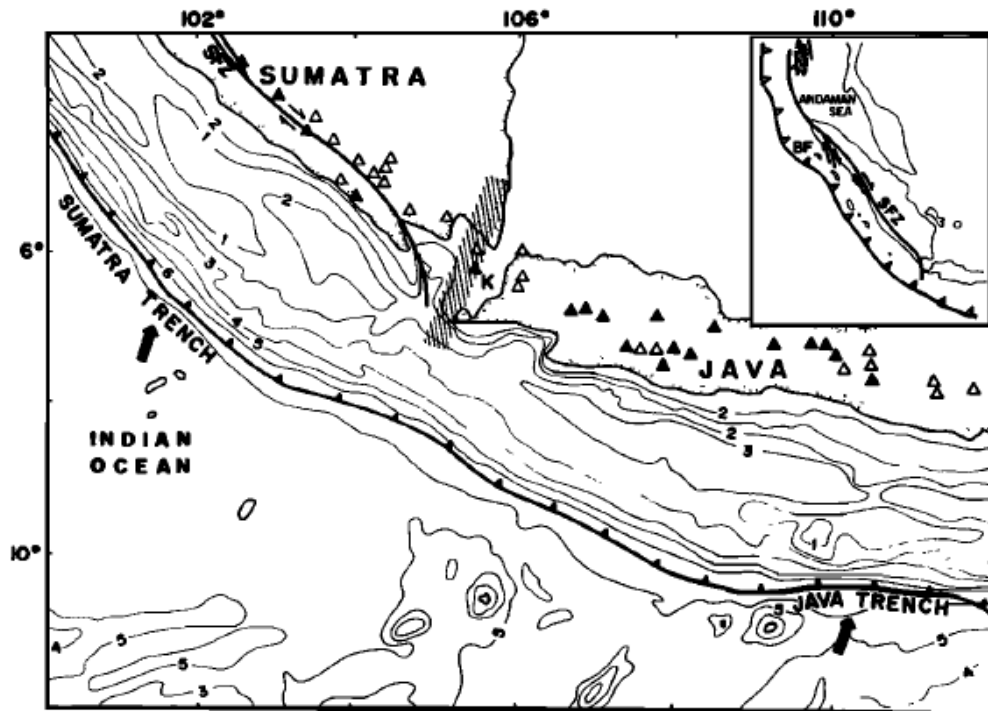
Figure 6: Geodynamics setting of Sumatra – Java trench system. Solid and open triangles represent active and inactive Volcanoes. (SFZ), Sumatra fault zone; (K), Krakatau complex (Harjono et al., 1991).

The age of the subducted plate varies laterally, it is relatively young beneath Sumatra with value around 40 Ma but moving south the age increase, in fact below Krakatau, the age of the subducted plate is around 80 Ma, and it becomes significantly older, reaching up to 130 Ma in Eastern Java (Abdurrachman et al., 2018). The lateral variation of nature and age of the subducted plate influences the style of deformation and subducted angle along Sumatra to Java, which may produce a thinning in the subducted slab between Sumatra and Java (Cloetingh & Wortel, 1986).

The character of subduction-related seismicity changes abruptly from Sumatra to Java; Seismicity does not exceed a depth of 300 km beneath Sumatra, except for some small events in the southeastern part of the island, but earthquakes occur at depths of up to 670 km below Java to the east (Figure 7) (Widiyantoro et al., 2011).
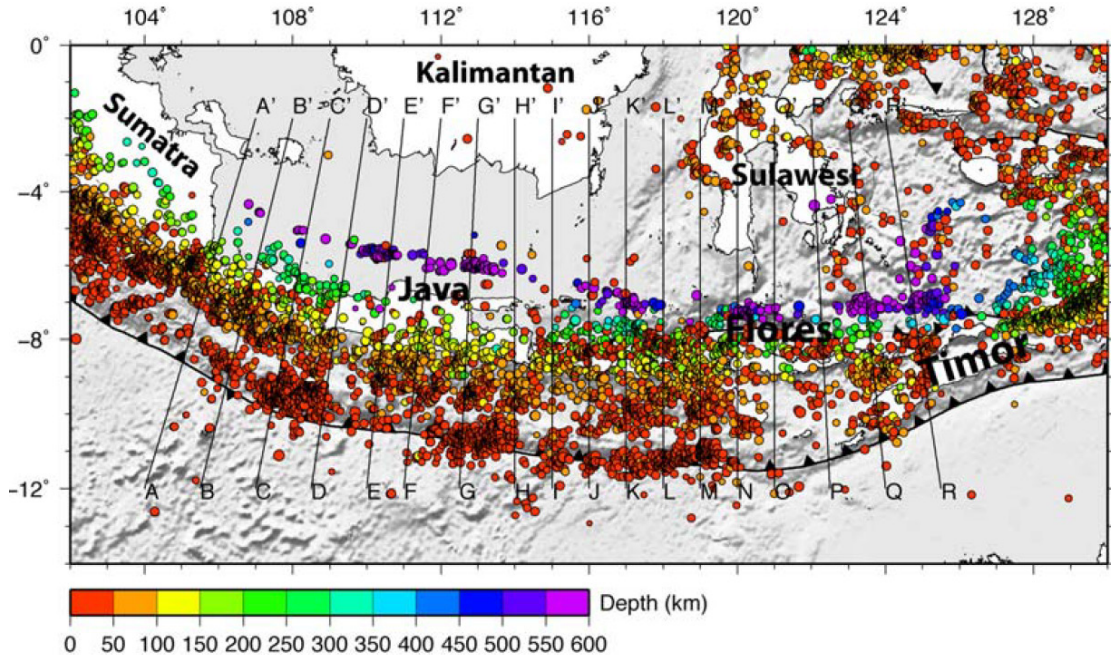
Figure 7: *Seismic Map. Circles depict the epicenters of relocated events (Engdahl et al., 1998, 2007) in the region occurring between 1964 and 2007, with colors denoting the hypocenters depths (Widiyantoro et al., 2011).*

2.3 Sunda Strait

The Sunda Strait lies between the islands of Java and Sumatra, has a roughly NE–SW orientation with a minimum width of 24 km and it is part of the convergent Sunda Island arc. It marks the transitional zone between two different models of subduction: from nearly frontal subduction of the oceanic Indo–Australian Plate beneath Java to oblique subduction beneath Sumatra (Hamilton, 1979; Huchon et al., 1984; Malod et al.,1995; Baroux et al.,1998).

The main structural features present in the Sunda strait are: The Java and Sumatra trench system, the Semangko fault system, and the volcanic line going from Panaitan island to Sukadana through the Krakatau complex, Sebesi, Sebuku and Rajabasa (Harjono et al., 1991). This setting implies that the Sunda Strait region is a key to the understanding of the geodynamic processes involved in this area (Figure 8).

9
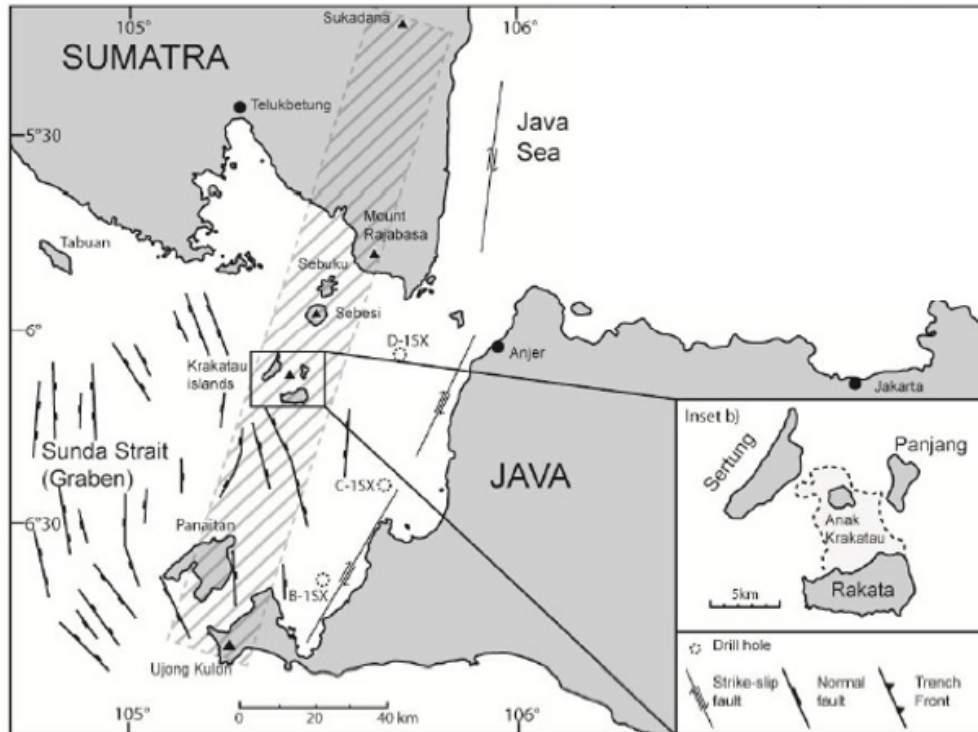
Figure 8: Simplified geological and structural map of the Sunda Straits, based on (Mandeville et al., 1996a; Schlüter et al., 2002; Lunt et al; 2009; Susilohadi et al., 2009). The locations of volcanoes that together with Anak Krakatau define a north-south trending volcanic lineament from Panaitan to Sukadana are marked with triangles. The hatched area in the center represents the volcanic lineament of quaternary volcanoes. Inset (b), shows details of Krakatau (Dahrèn et al., 2012).

The area of the Sunda Strait is mostly covered by Quaternary volcanic product. Nine wells were drilled during hydrocarbon exploration by Pertamina/Aminoil in the S and E part of the Sunda Strait (Noujiam 1976; Mandeville et al. 1996a). The closest of these drilled wells (C-1SX) is located ~30 km southeast of Anak Krakatau (Figure 8). The C-1SX well penetrated an apparently continuous sequence of sediments and sedimentary rocks of Quaternary to upper Pliocene age. The upper part (0-600m) consists of unconsolidated marine clays followed by clay-dominated siliciclastic rocks interbedded with volcanoclastic material to a depth of at least 3000 m (Nishimura et al., 1992; Mandeville et al. 1996a). Findings by (Lelgemann et al., 2000) suggest that the extension and rapid subsidence of the Sunda Strait have created space for up to

6 km of graben fill. Thus, the total depth of the sediments and sedimentary rocks in this part of the Sunda Straits can be constrained to between 3 and 6 km. The Pertamina-Aminoil wells all failed to reach the basement below the sedimentary sequence, but other wells to the southeast of Sumatra and northwest of Java have drilled Cretaceous granites and quartz-monzonites (Hamilton, 1979). The assumption of a sedimentary sequence underlain by a plutonic basement below Krakatau complex (Harjono et al., 1991) is supported by the presence of sedimentary (Mandeville et al. 1996b; Gardner et al., 2012), granitic (Oba et al., 1982) as well as dioritic, gabbroic and meta-basic xenoliths (Oba et al., 1982; Gardner et al., 2012) in Krakatau lavas and pyroclastic flows.

Some authors like (Ninkovich, 1976; Zen, 1983) proposed that the opening of the Sunda strait was related to the clockwise rotation of Sumatra by 20° relative to Java with an axis of rotation lying close to the Sunda Strait during Late Cenozoic time. (Huchon et al., 1984) ruled out the idea of the Sunda Strait opening by rotation; He first underlined the role of the Sumatra fault and suggested that the strait was formed by extension due to the north-westward displacement of the southwest Sumatra block (Sumatra forearc Sliver plate) along the Sumatra Fault Zone (Jarrard, 1986). (Susilohadi et al., 2009) confirmed this idea thanks to their structural data obtained in the Sunda strait; their data discredited the idea that the Sunda Strait opened due to the relative rotation of Sumatra against Java.

In addition, GPS studies suggest that the core of Sundaland, which consists of Sumatra, Malaysia, southwest Borneo and the western part of Java, is characterized by a stable tectonic block with minor internal deformation (Michel et al., 2000; Simons et al., 2007). (Lasitha et al., 2006) proposed also the opening direction for the Sunda Strait; they observed that the area is subjected to NW–SE extension because of the motion of the Sliver plate along Sumatran Fault and NE–SW compression because of subduction.
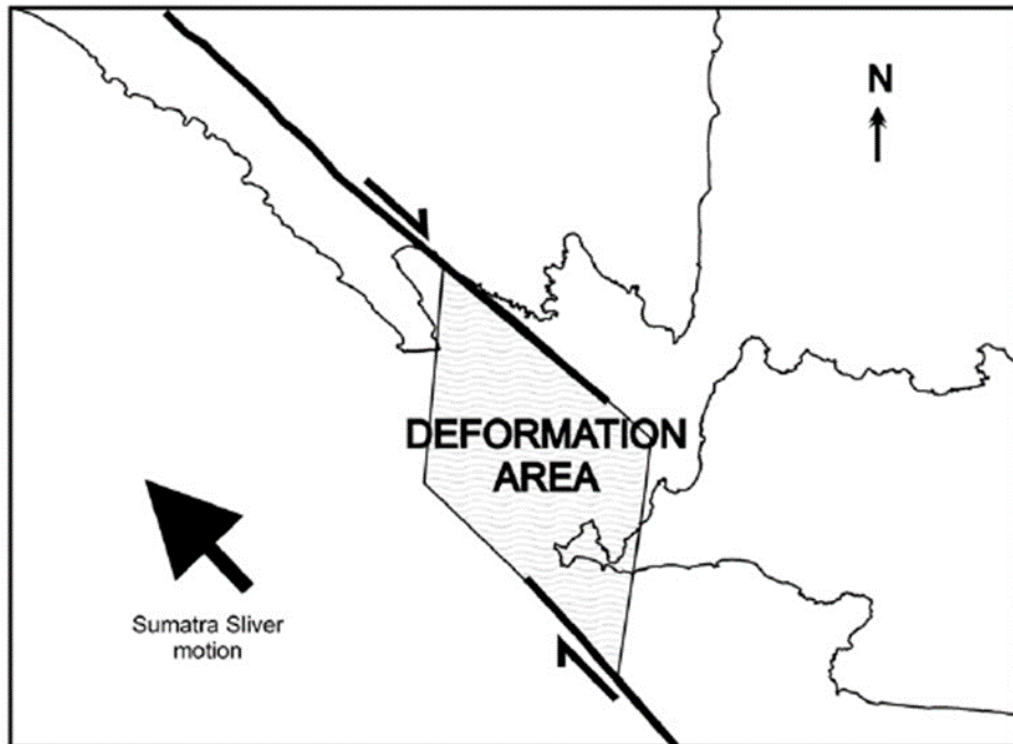
Figure 9: Simplified diagram of the Sunda strait evolution. Black harrow shows the Sumatra Sliver motion. (Susilohadi et al, 2009).

(Susilohadi et al, 2009) proposed also that, during the evolution of the Sunda Strait, some grabens have been generated since Late Miocene. Recent High-resolution bathymetry data, collected in the Sunda Strait, reveal two sub-basins separated by a basement ridge, a shallower domain to the east and a deeper graben to the west. These are connected by secondary transverse grabens cutting the basement ridge into discrete blocks (Lelgemann et al., 2000). The deeper western graben trends N-S along 104.8°E, exhibits an average water depth of 1800 m in the central part and lies at the southern termination of the Sumatra Fault. It is bounded to the west by a steep flank, which becomes more subdued at 6.5°S and disappears to the south. The eastern flank is more disturbed and cut by several canyons. Both flanks of the graben are tectonically active and display extensional patterns which are also evident in the seismic data (Harjono et al., 1991; Lelgemann et al., 2000).
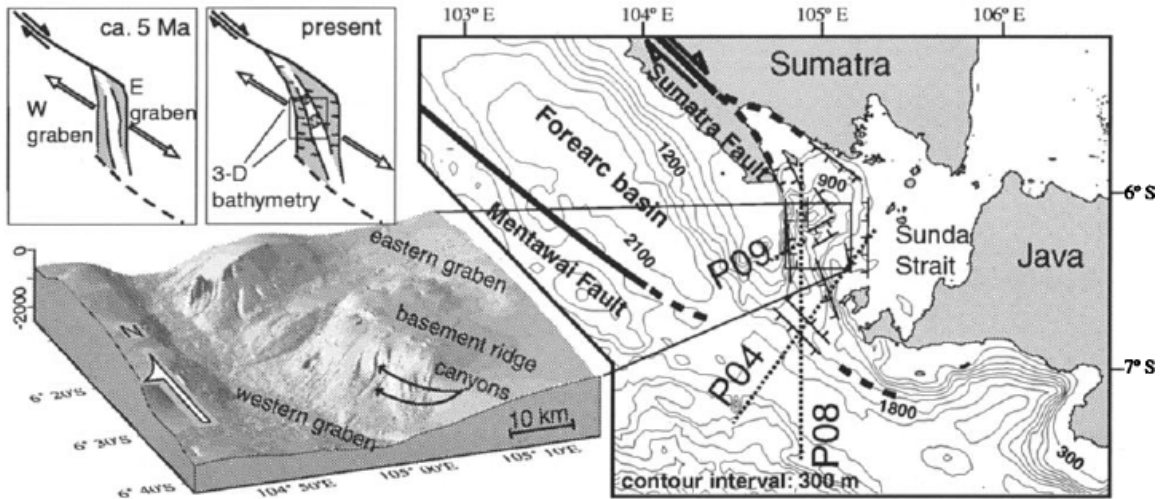
Figure 10: *Geodynamic setting of the Sunda Strait showing major faults. The 3D high resolution bathymetric image displays graben structures and basement blocks in the western Sunda Strait. The N-S trending deep western graben lies at the southern termination of the Sumatra Fault along 104.8°E. The upper inlay displays the evolution of the large-scale basin with two sub-basins* *(Lelgemann et al, 2000).*

Analyzing crustal earthquakes in the Sunda Strait area, (Harjono et al., 1991) clustered them into three groups: (1) beneath the Krakatau complex where they are typically of tectonic origin, (2) inside a graben in the western part of the strait, and (3) in a more diffuse zone south of Sumatra (Figure 11A).

Considering only shallow earthquakes (depths less than 60 km) with magnitudes greater than 4.5 was possible to observe that the seismicity highlights a N-S seismic belt, which coincides with the Krakatau volcanic line. This signifies that the lineament is a fracture zone.; Anak Krakatau is the only volcano that is still active in this volcanic line (Figure 11B). (Nishimura et al., 1992; Harjono et al., 1991).
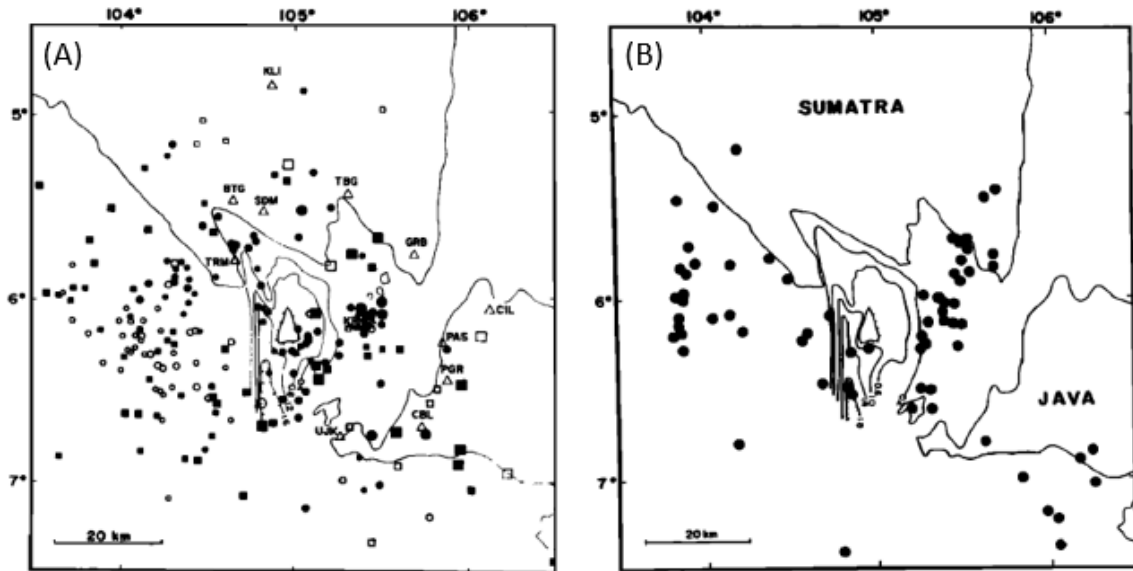
Figure 11: *(A), Map of seismic event recorded between 1964-1981; Full and open circles correspond to the depth of 0-20 km and 20-50 km respectively and the full and open squares correspond to 50-100 km and more than 100 km. Size of symbols corresponds to the class of accuracy (High accuracy – larger size symbols, medium accuracy -intermediate size symbols, low accuracy – small size symbols). Triangles show the stations used. (B), Shallow earthquakes (depth < 60 km) in the Sunda strait area (Harjono et al, 1991).*

Considering at the end, the individual and composite focal mechanisms of the events inside the strait, they show an extensional regime. A stress tensor, deduced from the individual focal mechanisms of the Krakatau group, shows that the tensional axis has a N 130° E orientation (Harjono et al. 1991); this confirm the opening direction proposed by (Lasitha et al., 2006). According also to (Camus et al., 1984; Nishimura et al., 1986), the Sunda straits correspond to a zone of crustal distension in which the volcanic axis would be a consequence of dilatational fractures. The amount of extension of the Sunda Strait is estimated to 50–70 km (Malod et al., 1996) and presumably occurred during the Pliocene (Diament et al., 1992). These studies confirm that the Sunda Strait is under a tensional tectonic regime.

3 Volcanic activity and evolution of Krakatau

The Krakatau volcanic complex is part of an NNE-SSW trending lineament of quaternary volcanic edifices which lies approximately perpendicular to the Java trench (Nishimura at al., 1992).

In the middle of the Krakatau complex there is Krakatau, an active volcano located at the junction of Sumatra and the Java Islands (Špičák et al., 2002) and it marks the changing of the subduction system from oblique along Sumatra to perpendicular along with Java (Abdurrachman et al., 2018). This volcano is situated at the intersection of the N20° volcanic line with a fault oriented N50° that links Krakatau to the Sunda Strait graben (Harjono et al., 1988; Deplus et al., 1995; Diament et al., 1990).
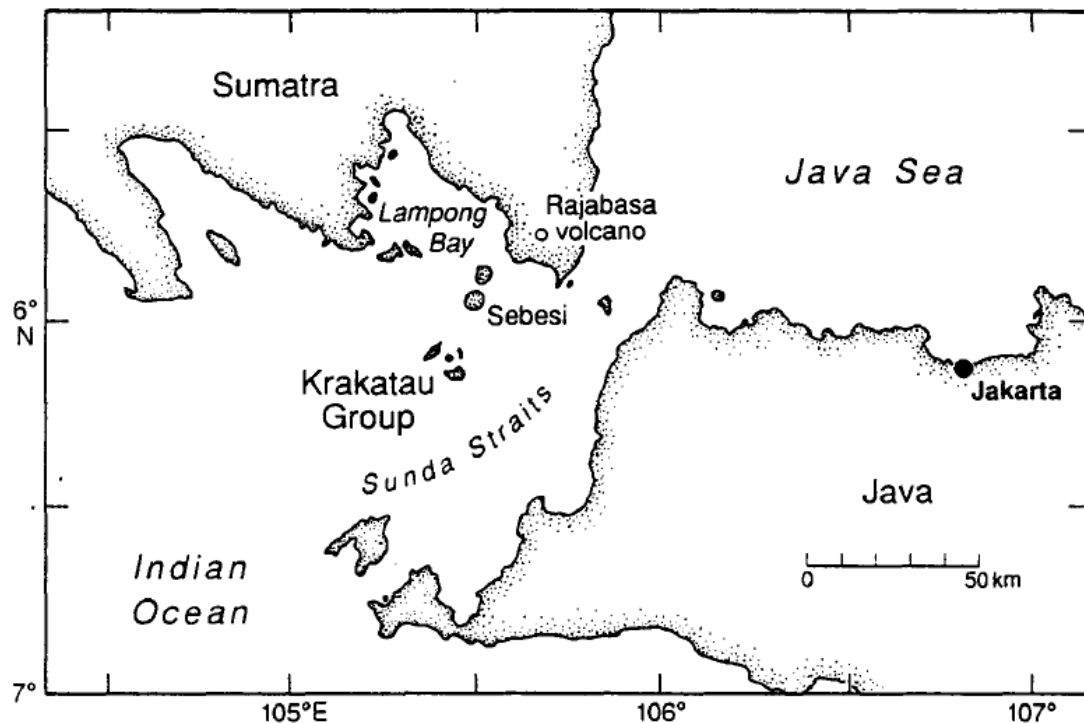
Figure 12: *Location map of Krakatau group (Self et al., 1992).*

The history of the volcanic activity of Krakatau can be divided into four main periods: Proto Krakatau, Krakatau, 1883 eruption and emergence of Anak Krakatau.

3.1 Proto Krakatau

Proto Krakatau was a shield volcano about 2000 m high and 10-12 km in diameter according to (Verbeek, 1885) and (Escher, 1919). Destruction of the primitive volcano would have resulted in the formation of a large sub-marine caldera which diameter is approximately 7 km (unknown age, perhaps in 416 or 535 CE; (Smithsonian Institute)). The prehistoric caldera was also confirmed by (Harjono et al, 1991) through a seismic study closes to Krakatau; the epicenters highlighted the prehistoric caldera and the one generated after the 1883 eruption (figure 13A). The confirmation of the presence of a prehistoric caldera is also given by the surrounding smaller islands of Sertung, Panjang (Rakata Kecil) and Rakata; remnants of the rim of the prehistoric caldera (figure 13B) (Wiliams, 1941).
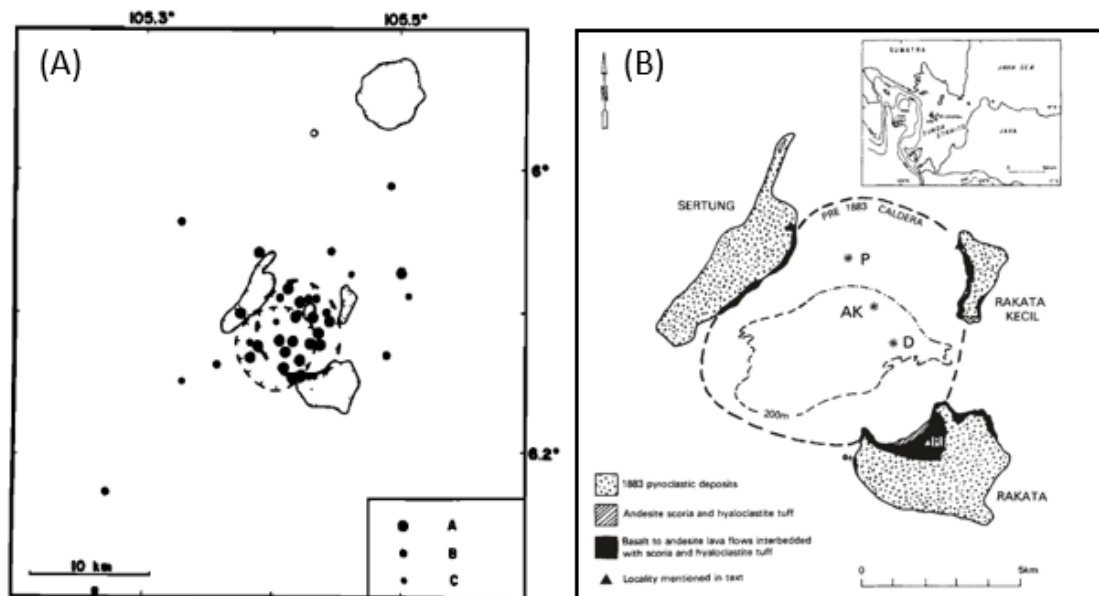
Figure 13: Sketch maps of Krakatau archipelago with calderas. (A), epicenters close to the Krakatau complex which shown the calderas; Thick line shows the older caldera; Thin line resulting from the 1883 explosion (redrawn from Camus et al., 1983). Size of symbols corresponds to the class of accuracy. (Harjono et al, 1991). (B), prehistoric caldera and possible 1883 caldera outline (200-m isobath, lighter dashed line, dash dot where conjectural). R, Rakata cone; P and D, Perbuwatan and Danan vents on pre-1883 Krakatau Island; AK, vent of Anak Krakatau. Outline of islands is from Indonesian Geological Survey map (1940) (Self et al., 1981).

3.2 Krakatau

After the destruction of Proto Krakatau, a new formation of 812 m basaltic cone developed on the edge of the prehistoric caldera and it covered the Rakata remnant. Then, followed a growth of two andesitic cones, Danan (450 m a.s.l) and Perboewatan (120 m a.s.l.) within the caldera (Deplus et al., 1995; Neumann van Padang, 1933b). These volcanic edifices developed until the 1883 eruption (Simkin et al., 1983).
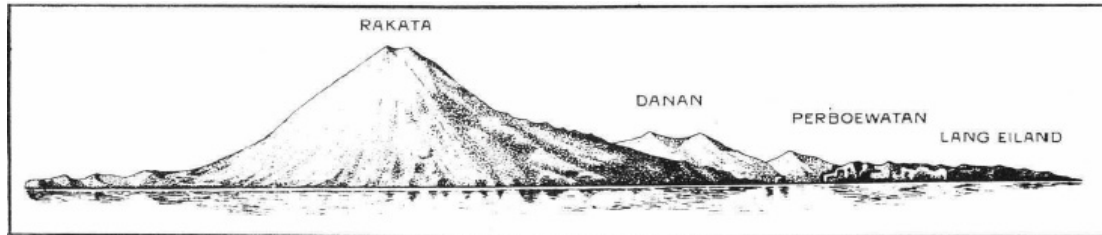
Figure 14: The islands of Krakatau in 1836, as sketched by Muller (1844), seen from the southeast, Pepper Bay (Neumann van Padang, 1933b).

The island constructed of these three volcanoes (Perbuwatan, Danan and Rakata) is Krakatau, a large island 9 km long and 5 km wide situated along a fissure within the prehistoric caldera (Williams, 1941); All these main cones and the other smaller cones and craters were apparently aligned on an NNW trending fissure (Simkin et al., 1983).
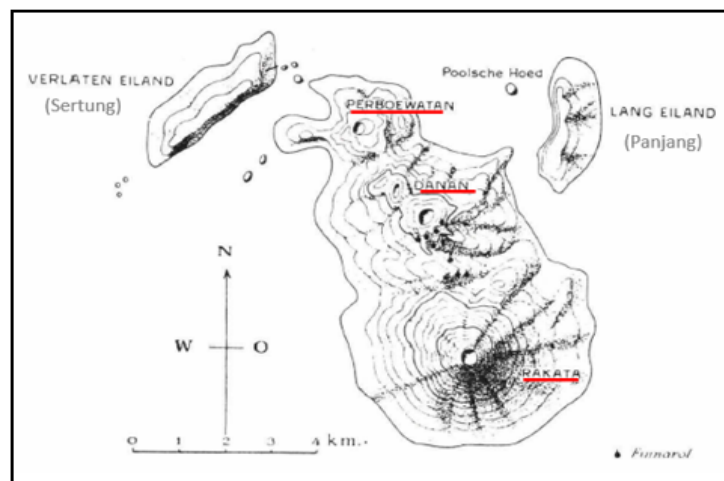
Figure 15: The islands of Krakatau according to the topographical sketch of Captain Ferzenaar, the sketch of (Müller, 1844) and the data of Verbeek. The red lines identify the positions of the three craters. (Neumann van Padang, 1933b).

3.3 1883 eruption

The 1883 eruption is one of the largest volcanic explosions that has occurred in human history. Volcanic activity was first observed on the 20th of May 1883 and it continued intermittently during the next few months until the 27th of August when activity reached its peak (Nomanbhoy et al., 1995).

During the catastrophic activity enormous quantities of ash and pumice were thrown out, on 20 May 1883 Mt Perboewatan began to emit pumice and ash, in June also Mt Danan began to erupt and in August three craters were active (Neumann van Padang, 1933b). The consensus of opinion is that the main vent for the 1883 eruption lay between the vents of Perboewatan and Danan (Self et al., 1981).
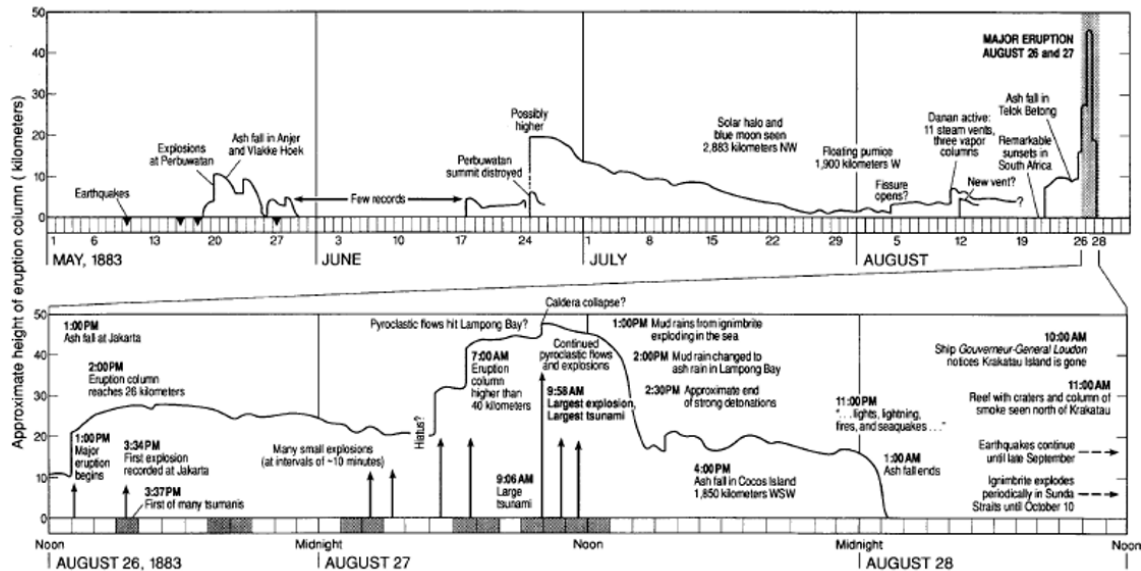
Figure 16: *Diagrammatic representation of the 1883 eruption sequence at two scales: Upper: the whole eruption sequence from May to August. Lower: the climactic phases from 1:00 pm on 26 August to 1:00 pm on 27 August (stippled on upper diagram) and other phenomena. Adapted from (Francis et al., 1983). Major recorded explosions shown by arrows; major tsunamis by shading in bottom bar. Many smaller explosions and tsunamis omitted.*

The eruption event went through several stages, including a lengthy, intermittent vulcanian to subplinian phase from May to August 25, a 13 to 14 hours plinian phase on 26-27 August, and an 8 hour-long ignimbrite producing phase on August 27 (Self et al., 1992). (Camus et al.,1983a, b; Vincent et al., 1986; Camus et al., 1992; Deplus et al., 1995) proposed a flank failure of the volcano to explain the drastic change from plinian to ignimbritic activity.

During the eruption, precisely on 26 August, the greater part of the main island disappeared (figure 17), according to (Verbeek, 1885) by collapse, forming a submarine basin. The emitted material covered Lang Island (Panjang), Verlaten Island (Sertung) and the remaining part of Rakata.
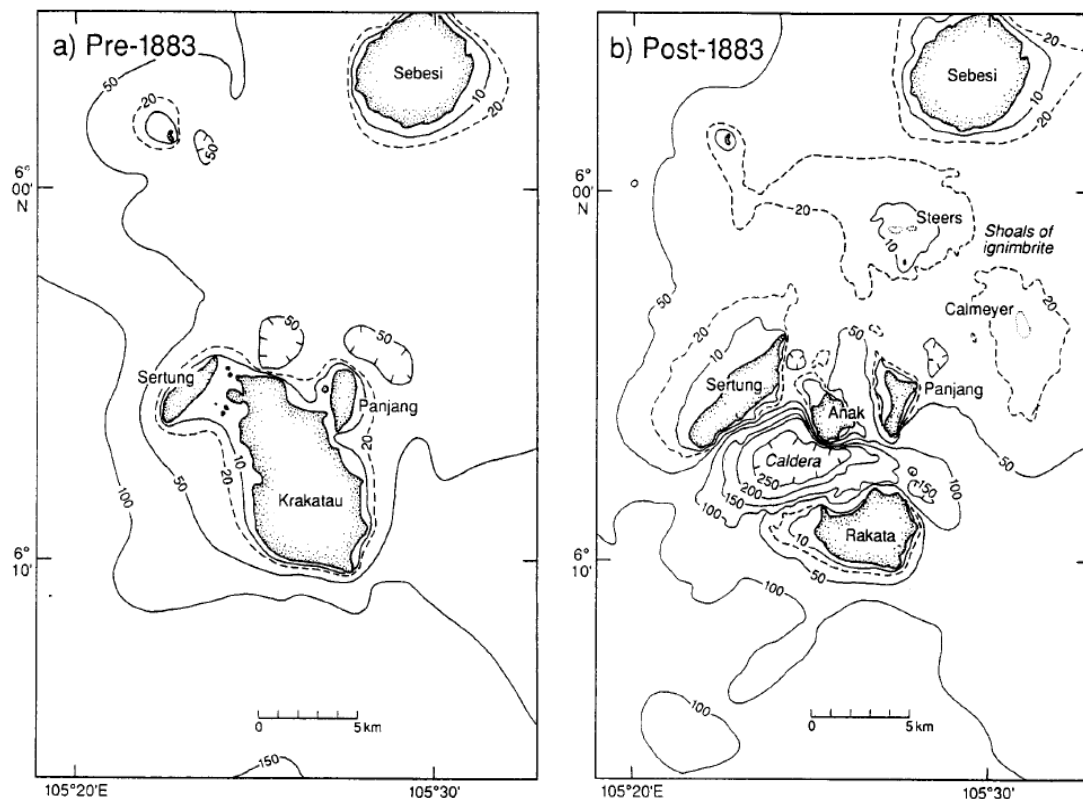
Figure 17: Simplified maps of Krakatau volcano and bathymetry of the local area in Sunda Straits. (a), before and (b), after the 1883 eruption. From (a) Dutch surveys conducted in the Straits (Verbeek 1885; Simkin et al., 1983); (b) (Sigurdsson et al., 1991); Submarine contours in meters.

The explosions generated by Plinian phases on 26 August, produced fall units of dacitic pumice up to 20 m thick that are exposed on the islands of Panjang and Sertung and pyroclastic surge deposits founded interstratified with the fall units which indicate that minor eruption column collapse during this stage of the eruption produced the low-density turbulent pyroclastic surges (Paris et al.,2014; Fischer, 1979). In the early morning of 27 August 1883, activity shifted from a convecting to a collapsing column, thus producing massive accumulations of pyroclastic flow deposits (Ignimbrite) (Paris et al., 2014) and, during their eruption, much vitric dust was dispersed in the atmosphere and formed a fine ash-fall deposit, the co-ignimbrite ash, with a volume estimated equal to 2.3 km^3 (Mandeville et al., 1996; Verbeek 1886). All these events reported are shown in the sedimentary sequence obtained by (Self et al., 1981).

Figure 18: Composite stratigraphic section of the 1883 pyroclastic deposits compiled from several location on Panjang, Sertung and Rakata islands (Self et al., 1981).

The Krakatau pyroclastic flows (Ignimbrite) apparently moved preferentially to the north and north-east and covered the islands and surrounding sea floor with dacitic ignimbrite. Deposition of ignimbrite also extended Sertung and Panjang Islands and the southern and eastern parts of Rakata (Self et al., 1981) and some of the deposits were initially emergent and formed the two shallow islands of Steers and Calmeyer (6.5 m maximum elevation). These islands had disappeared below sea level by the fall of 1886 (Mandeville et al., 1996).

(Self et al., 1981) propose that the large pyroclastic flows were erupted before major collapse of the volcano because the 250 m deep caldera was apparently not extensively filled with deposits of 1883 ignimbrite and (Verbeek, 1884) proposed that the submarine pyroclastic flows largely filled the 30-40 m deep basin in the sea floor; this explain the shallowing of the sea floor as far as 15 km to the north of Krakatau.
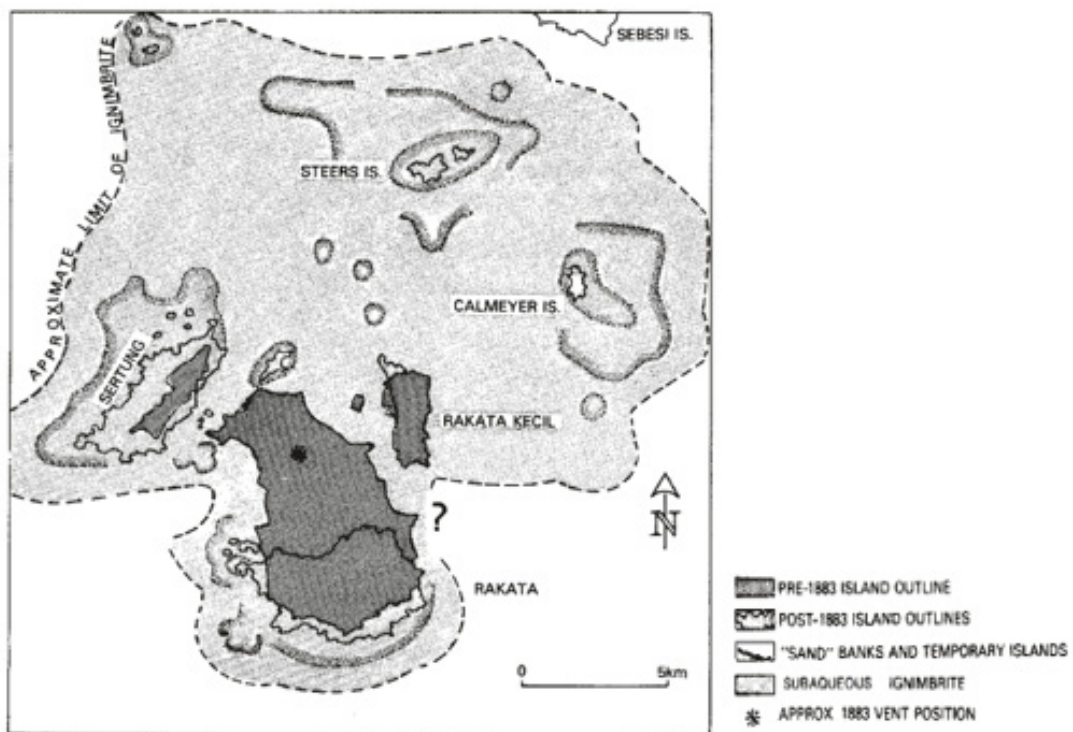
Figure 19: Submarine distribution of the 1883 ignimbrite. Stippled pattern shows extent of ignimbrite. Also shown are temporary islands and shallow banks where ignimbrite protruded above sea level (Self et al., 1981).

Thanks to (Verbeek, 1884; Verbeek 1885) was possible to obtain the total volume erupted; the total bulk volume of the 1883 Krakatau deposits was estimated as 18-21 km^3. More recently (Yokoyama, 2015) proposed a new value for the total amount of pyroclastic material equal to 19.3 km^3 (DRE). Instead, the volume of ignimbrite was roughly estimated as 16 km^3 (Self et al., 1992) and the conservative estimate of total erupted mass was approximately 3.0 x 10^{16}g (Mandeville et al., 1996b).

Possible triggering mechanisms for the 1883 Krakatau eruption are: increasing volatile concentration, over-saturation during crystallization of the dacite magma body (Williams, 1941; Blake, 1984), and hydrofracturing due to ingress of seawater, but a lack of evidence for large scale magma-water interaction in the Krakatau pyroclastic products, such as very fine grained may indicate that hydrofracturing was not an important eruption-triggering mechanism at Krakatau (Self, 1983). More recently was proposed by (Self et al., 1992) that the 1883 eruption may have been triggered by the injection of basaltic magma into a dacite magma body under Krakatau. (Camus et al., 1987) supported this idea and proposed that the process of Magma mixing could account for the heterogeneity of the products ejected from Krakatau. Evidence for magma mixing, observed by (Mandeville et al., 1996b), includes banded pumices, glass inclusions (that are more mafic than whole rock) and matrix glass compositions.

The 1883 Krakatau eruption was accompanied also by tsunamis that harassed the coasts of Bantam and South Sumatra, killed nearly 37 000 human beings and destroyed 297 villages completely or partly (Neumann van Padang, 1933b). The tsunamis were produced by a hydrovolcanic explosions and the associated shock waves and pyroclastic flows (Mader et al., 2006). Considering the evidence reported by (Verbeek, 1884, Verbeek, 1885, Symons, 1888), (Self et al., 1992) proposed as main cause for tsunamis the impacts between several cubic kilometers of pyroclastic flow material and the sea immediately after each of the large explosions (figure 20).
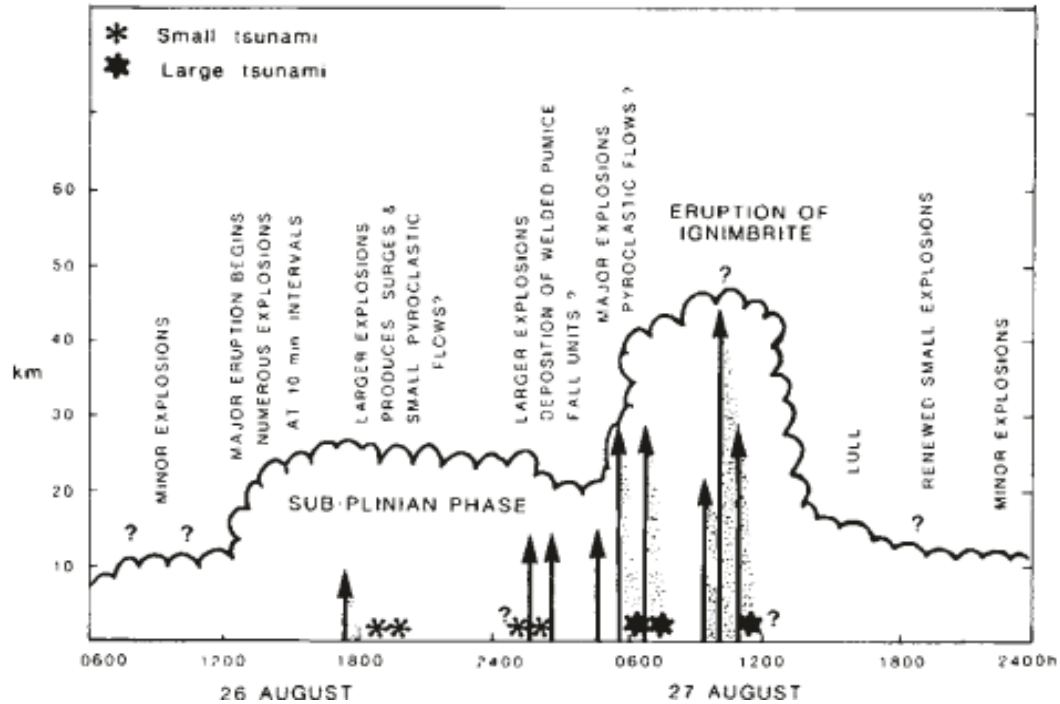
Figure 20: *Sequence of reported explosions and tsunami during 26-27 August 1883 (all times are local). Data from (Verbeek, 1884, Verbeek, 1885, Symons, 1888). Relative magnitudes of explosions, as recorded by the Batavia gasometer, are indicated by lengths of arrows. Approximate eruption column heights given at left are not accurate to more than ± 5 km. Travel times of tsunami from Krakatau to Java and Sumatra coasts estimated at between 30 min and 1 h (Symons, 1888).*

3.3.1 1883 caldera

Following the 1883 eruption there were significant bathymetric changes that took place around the Krakatau islands; As mentioned before, much of the original island of Krakatau was destroyed and, in its place, a deep submarine caldera was formed (Carey et al., 2000). (Williams, 1941) suggested that the 1883 caldera lies within the prehistoric Krakatau caldera (7 km diameter) and seems to be a graben-like feature. Considering (Deplus et al., 1995), the 1883 caldera depression is elongated in shape with two main directions: southwest-northeast and west-east; the deepest part is located southwest of Anak Krakatau and has a rectangular shape with a flat bottom (240 m below sea level) and steep linear walls.

23

The north and south walls of the deepest part are oriented N70° with slopes of about 20°, the east and west walls are oriented N 150°, and the slope on the western one is smaller of about 7°. The N150° azimuth corresponds to the direction on which Danan and Perbuatan vents were lying and also where Anak Krakatau had its eruptions during its emersion (six craters in line) (Deplus et al., 1995; Stehn, 1929).
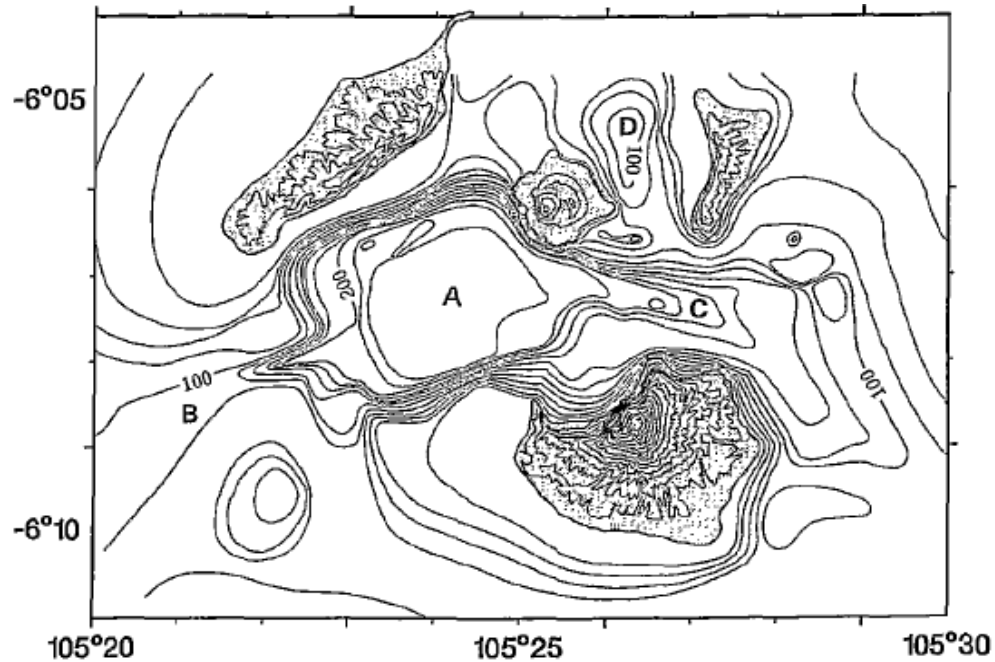
Figure 21: Detailed bathymetric map of the 1883 caldera drawn from data gathered during the MENTAWAI cruise (1990) and digitized data from existing bathymetric maps. Isolines are drawn every 20 m and solid lines represent curves - 100 and – 200 m. A, B, C, D indicate the identify bathymetric depressions (Deplus et al., 1995).

There are also bathymetric depressions to the southwest and to the east of the caldera (B and C) with deep more than 100m; for (Deplus et al., 1995), the southwest depression corresponds to the termination of the fault oriented N50° mentioned before. (Deplus et al., 1995) proposed also that this N150° is a tectonic weakness zone that could have guided both the development of the volcanic activity and the caldera emplacement during the 1883 eruption. This major weakness zone passing through the summit line of the pre 1883 Krakatau volcano and created a significant disruption surface of the volcanic edifice.

The same authors also noticed that southwards prolongation of the N150° line intersects the Rakata coastline at its northern cape and separates two slump events (recognizable by morphological signs), to the west and to the east of the island. This idea allows to understand the particular shape of Rakata island; the missing part of the cone has probably slumped into the sea along two collapse zones located on each side of the N150° line and it confirms the previously idea exposed by (Williams, 1941) which proposed that the caldera collapse was controlled by pre-existing structures.
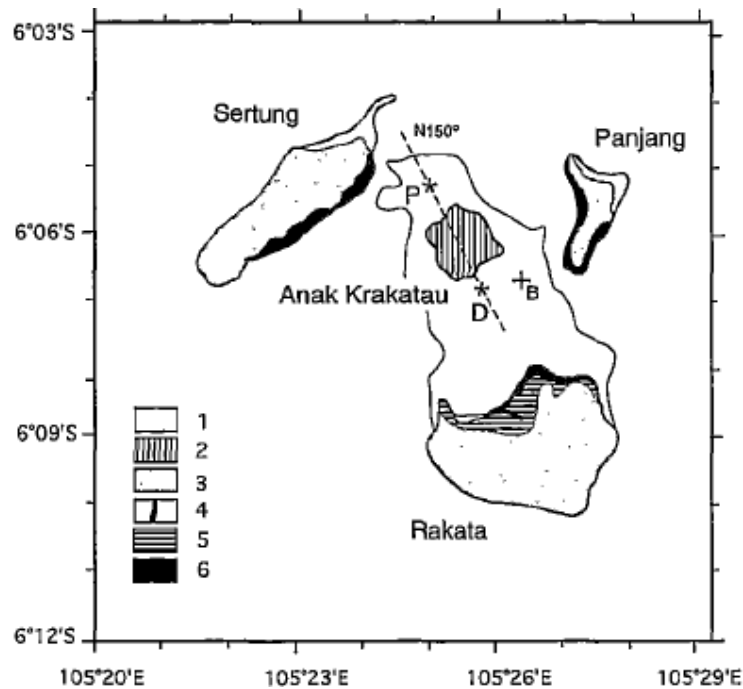
Figure 22: *Geological map of the Krakatau volcanic complex (from Geological Survey of Indonesia). 1=alluvial deposits; 2=recent volcanic products of Anak Krakatau (basalt and andesite); 3=pyroclastic deposits of the 1883 eruption; 4=Rakata basaltic dyke; 5=Rakata basaltic rocks; 6=old volcanic substratum of the proto-Krakatau (trydimite andesite). B=Bootmans rock. Light solid line indicates the coastline of Krakatau island before 1883: P=Perbuatan crater, D=Danan crater (Deplus et al., 1995).*

There is a controversy on the mechanism of formation of the caldera; (Verbeek, 1885) proposed a mechanism of collapse preceded by internal melting of the cones, (Judd, 1888) proposed that the Krakatau caldera had been formed by explosive decapitation

25

of the volcano during the paroxysm, (Escher, 1919; 1928) as quoted by (Williams, 1941) explained the caldera as the result of an explosive coring of an inner cylinder and a sliding of the cones along funnel-shaped glide planes and (Yokoyama, 1981) follows a similar line of thought (Scandone, 1990). In this last model proposed, lithics and juveniles' fallback products (caldera deposits), filling the caldera bottom and would be responsible for a negative gravity anomaly due to their contrast of density with the surrounding rocks (Scandone, 1990).

For (Yokoyama, 2015) the caldera depression is 5.1 km^3 and it was formed by disruption of 2/3 parts of pre-existed Krakatau Island and excavation of the seabed to a depth of 250 m. The same author assumed caldera deposits of low density immediately beneath the caldera depression and estimated their volume at roughly 13 km^3 bulk (Yokoyama, 1981; Yokoyama, 2014). According to Yokoyama, (Deplus et al., 1995) obtained a model that shows this low-density body (Figure 23b) and interpreted it as a mix of juvenile products of the 1883 eruption and lithic remnants of the destructive volcano filling up the 1883 caldera (Figure 23a). The same authors obtained also a model to consider the high-density body that is around the caldera depression (interpreted as volcano substratum of the proto Krakatau). In their models they considered that the density contrast with respect to a reference value of 2.1 g/cm^3 are about + 0.5 g/cm^3 for the dense substratum (old proto Krakatau) and - 0.2 g/cm^3 for the caldera infill.
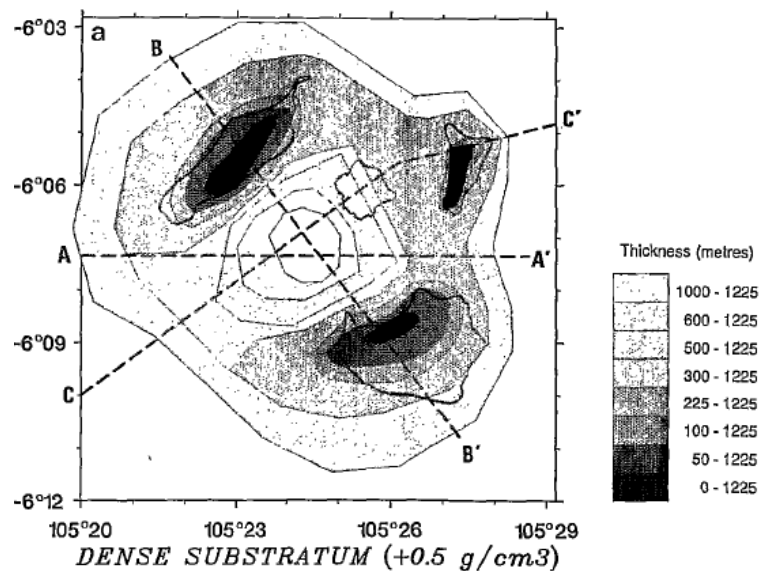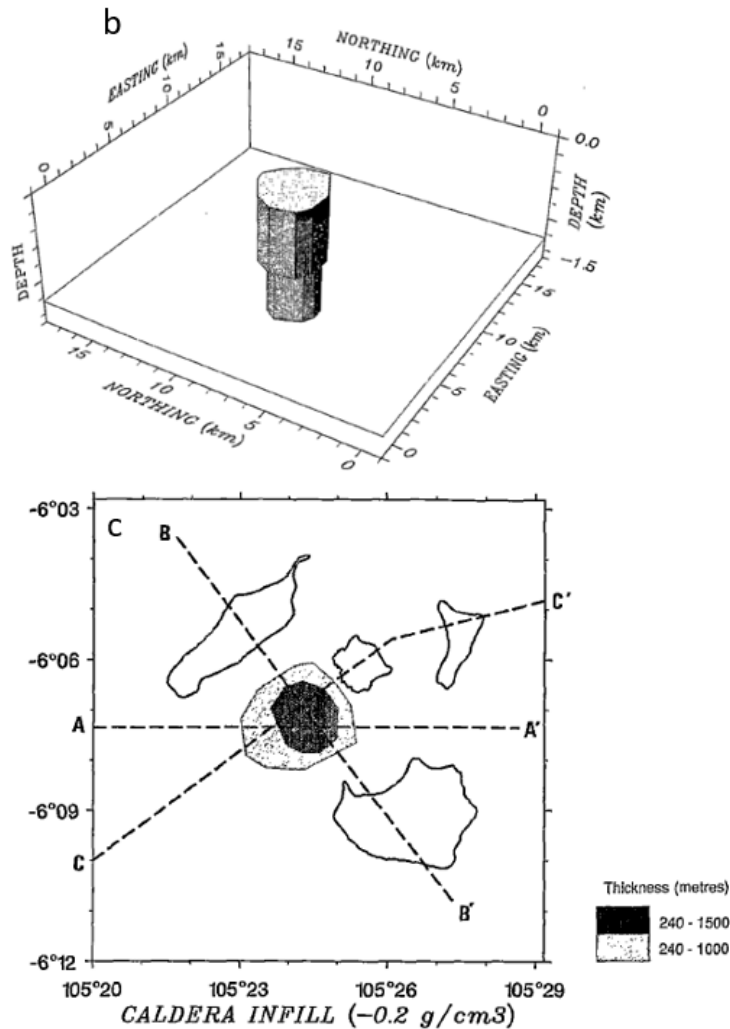
Figure 23: Physical models showing the 1883 caldera; (a), Horizontal geometry of the model. The grey color scale indicates the thickness of the density body below the sea surface; (b), Low-density body (density contrast of - 0.2 g/cm3) interpreted as a mixing of juvenile products of the 1883 eruption and lithic remnants of the destructed volcano filling up the 1883 caldera; (c), Low density body: Caldera infill (Deplus et al., 1995).

Considering these models, (Deplus et al., 1995) were able to obtain the thickness and the shape of the low-density body and the volcanic substratum. The substratum is sub-cylindrical with a hole in the center, its thickness is on average 1000 m, its flat bottom lies at a depth of about 1225m b.s.l., its top lies at 225m b.s.l. except beneath the outer islands where it forms their basement and it has two distinct slopes.

The upper one is moderate, prolongs the inner parts of Rakata, Sertung and Panjang islands and it is covered with 2.1 g/cm^3-density material. (might be a result of pre-historical collapse before the 1883 eruption). The deeper slope is located just below the flanks of the rectangular part of the bathymetric depression SW of Anak Krakatau island and it limits the area filled up with 1000-1500 m of low-density material. Observing also, the residual gravity anomaly obtained by (Oemaiya et al., 2019) is possible to notice the shape and the localization of the caldera depression; These data agree with (Deplus et al., 1995) regarding the idea that the underground structure is smaller in diameter than the bathymetric outline of the morphological depression.
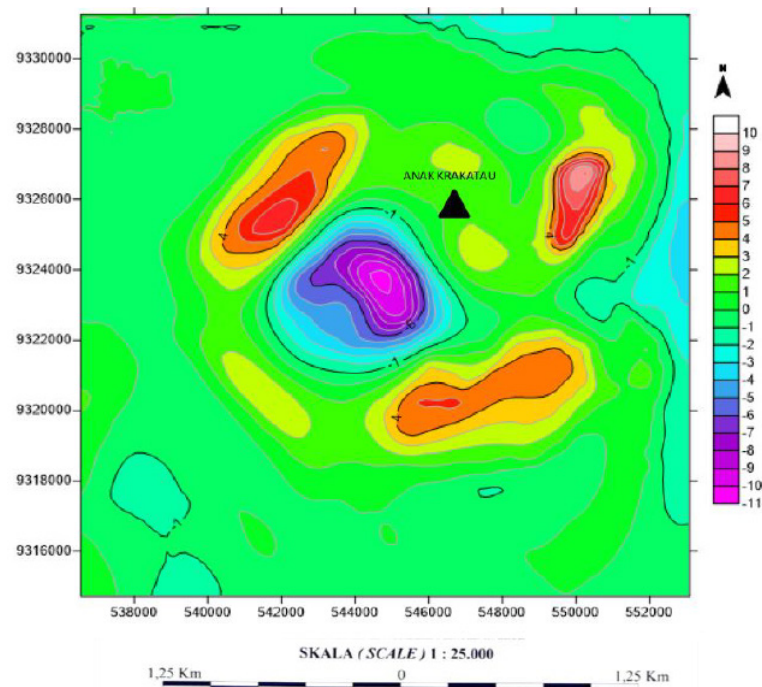
Figure 24: Residual Anomaly Map of Krakatau archipelago (Oemaiya et al., 2019).

In conclusion, (Scandone, 1990) suggested that the shape of the gravity anomaly allows to discriminate between piston-like or chaotic collapse and the observed gravity anomalies over Krakatau better fit the chaotic model. Considering this idea (Deplus et al., 1995) proposed two models; one considering a piston collapse and the second one considering the chaotic collapse but, according to their data, they cannot discriminate between both mechanisms.

3.4 Emergence of Anak Krakatau

After a quiescence of less than half century the post collapse cone of Anak Krakatau, also called child of Krakatau, was constructed in strong disequilibrium on the edge of the steep NE wall of the 1883 caldera at a point between the old cones of Danan and Perbuwatan (Camus et al., 1983b; Description from Smithsonian Institute). The birth of Anak Krakatau was noticed for the first time on December 29th 1927, grew as a submarine cone and between 1928 – 1930 receded and reappeared three times until it established itself permanently above sea level. The crater edge appeared for the first time above the sea level on January 28th 1928; thereafter, periods of intense surtseyan activity alternated with intervals of rest, up to Febuary 28th 1929. The result of this two-year period of activity was a sickle-shaped island, reaching 38 m a.s.l., and 275 m in length (Stehn, 1929; Camus et al., 1987, Giacchetti et al., 2012).
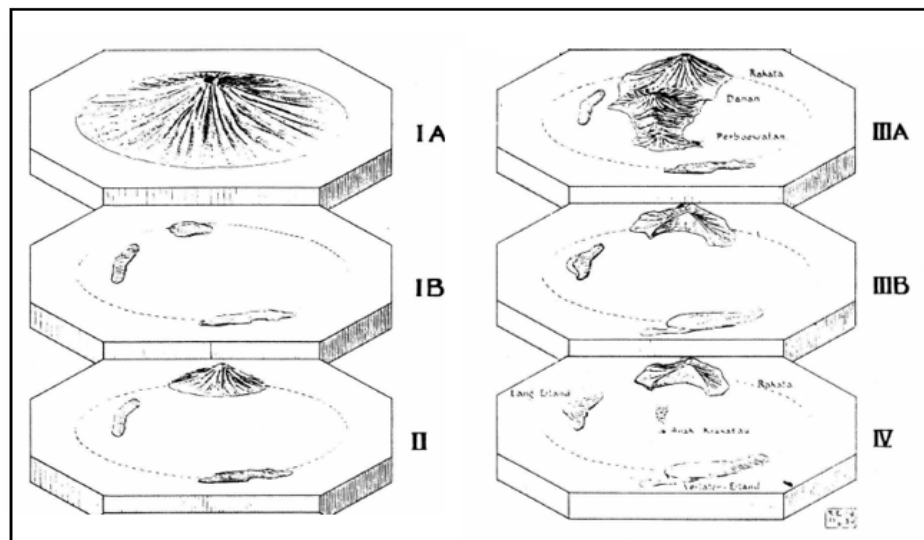
Figure 25: The history of the volcano Krakatau, as sketched by (Escher, 1931b); IA, The hypothetical big original volcano; IB, Three small islands, remnants of the foot of the original volcano, remained on the border of a large caldera; II, A basaltic volcano, Rakata, originated on the southern border of the caldera; IIIA, North of Rakata, the andesitic volcanoes Danan and Perboewatan originated; IIIB, Situation after the catastrophic eruption of 1883, showing the sea above the new caldera; IV, This figure was added in 1930 after the origin of the eruption center Anak Krakatau in the middle of the caldera.

This was followed between 1930 and 1959 by a new stage characterized by development of a complete 152 m high hyaloclastic tuff-ring in which a lake developed within its crater (Sudradjat, 1982).

During the 1959-1960 activity an inner cone began to grow at the place of the crater lake; by that time, Anak Krakatau was a definite subaerial vent (Decker and Hadikusumo, 1961). The eruption style from Surtseyan become Vulcanian until 1960 and then shifting to Strombolian explosions that created a cone reaching 200 m a.s.l on 1981 (Oba et al., 1982). In 1981, a Vulcanian eruption marked a southwestward shift of Anak Krakatau activity (Sudrajat, 1982) with more differentiated volcanic products (acid andesites, dacites) than previously erupted (mainly basalts and andesites) (Camus et al., 1987) and resulting in further growth of the edifice over the cliff and toward the deep submarine caldera basin (Self et al., 1981).

(Sudradjat, 1982) emphasized a shift of activity towards the southwest possibly related to the sea-floor configuration and (Giacchetti et al., 2012) proposed that this shift of the volcanic activity could bring a possible landslide from the south-western side of the island and the corresponding generation of a tsunami. After 1981, the volcano remained active with intermittent ash and lava flows events and strombolian explosions until the recent activity beginning on October 2007 which is still ongoing intermittently (Smithsonian Institute). At the time of writing, the latest eruption, reported by (Smithsonian Institute), started from February with Intermittent Surtseyan explosions increased in frequency and continued through July 2019.

4 Anak Krakatau

Anak Krakatau is located in the center of the Krakatau volcanic complex at a latitude of 6.102° S and a longitude of 105.423° E. It is actually one of the most active volcanoes in Indonesia with 45 eruptions (explosive and effusive) from its emersion with VEI values between 1 and 3 (Smithsonian Institute). The birth and evolution of Anak Krakatau (reported before) underlines that this volcano is only a part of the cyclical nature of the growth and destruction of Krakatau volcano.

(Abdurrachman et al., 2018) is the author who shows the most recent geological map of Anak and reported that the volcano is constructed of alternating layers of 18 lava flows and 18 pyroclastic deposits that have been built since 1927.
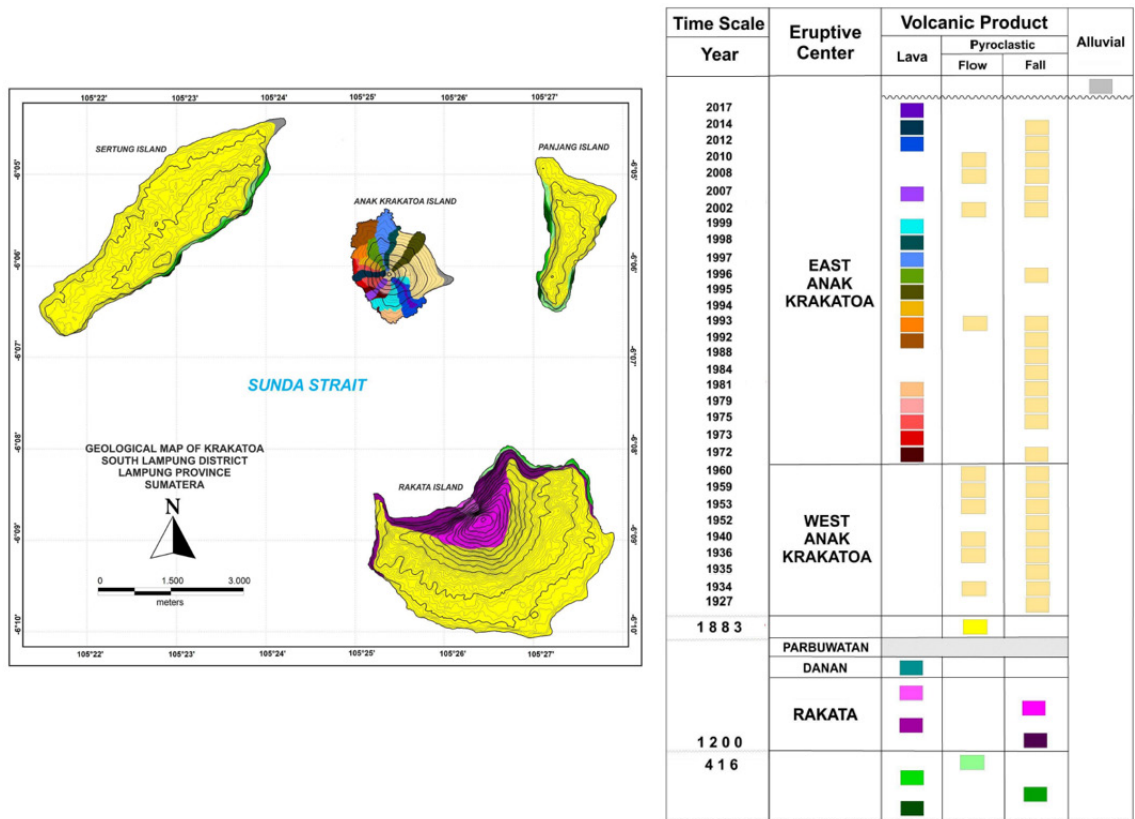
Figure 26: *Geological map and stratigraphy of the Krakatau volcanic complex (Abdurrachman et al., 2018).*

Considering Anak Krakatau products, (Camus et al., 1987) made an accurate analysis; Products in the tuff-ring and lava flows are basic andesite, without noticeable variation between 1927 and 1979. The rocks are highly porphyritic with 35% of phenocrysts and microphenocrysts. The distribution of ferro-magnesian phases is varied: olivine phenocrysts are found in bombs of the tuff-ring (2.5%), while it can be nearly absent in some lava flows. Either clinopyroxene or orthopyroxene can be dominant, but the amounts of pyroxene phenocrysts do not exceed 3%.

Products of the 1981 vulcanian eruption are more differentiated; Plagioclase is the main constituent as phenocrysts (23%) and microlites. Pyroxene phenocrysts are well represented as cpx (3%) and opx (3.5%), Oxides (2%) are both Magnetite and Ilmenite. Olivine is exceptional and destabilized (Camus et al., 1987). The same authors note also the absence of hydrous minerals in all recent Krakatau products.

(Van Bemmelen, 1942) suggested a cyclic activity for Krakatau (valid also for Anak-Krakatau), with the succession of each cycle being: basalt, basic andesite, acid andesite, dacite. The last of these corresponds to the cataclysmic eruptions. For (Bani et al., 2015), the birth of Anak Krakatau marked the onset of a new eruptive cycle.
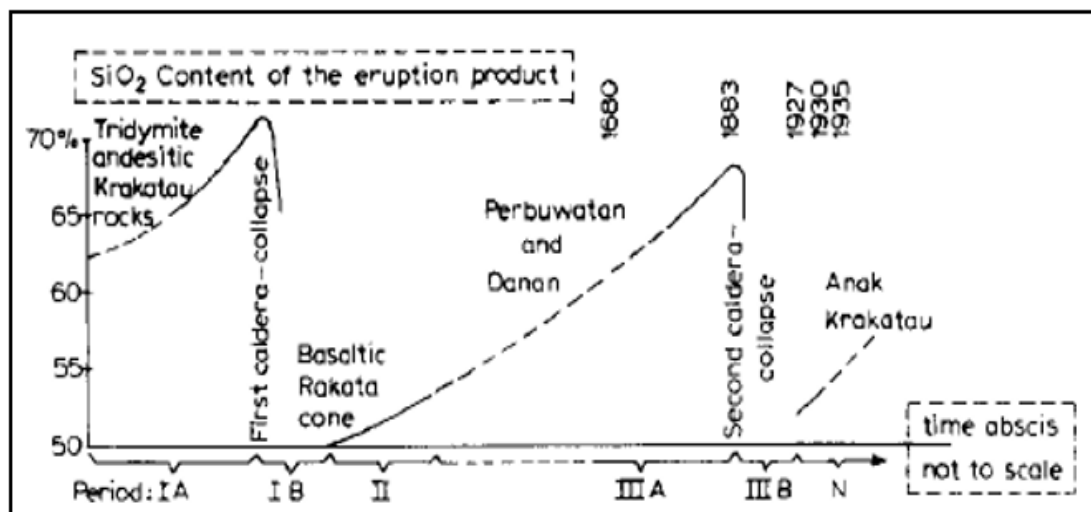
Figure 27: *SiO$_2$ content of the eruption products by (Van Bemmelen, 1942).*

From the chemical point of view, the Anak lavas (Oba et al., 1982, 1983a, b; Camus et al., 1987) constitute two groups separated by a gap (Figure 28): (a) The basalts and andesites with an SiO_2 content <57.5% are characteristic of the 1927-1980 period; (b) The differentiated lavas that are characteristic of the 1981 eruption. Thus, the Anak cycle is representative of the cyclicity of the entire volcano.
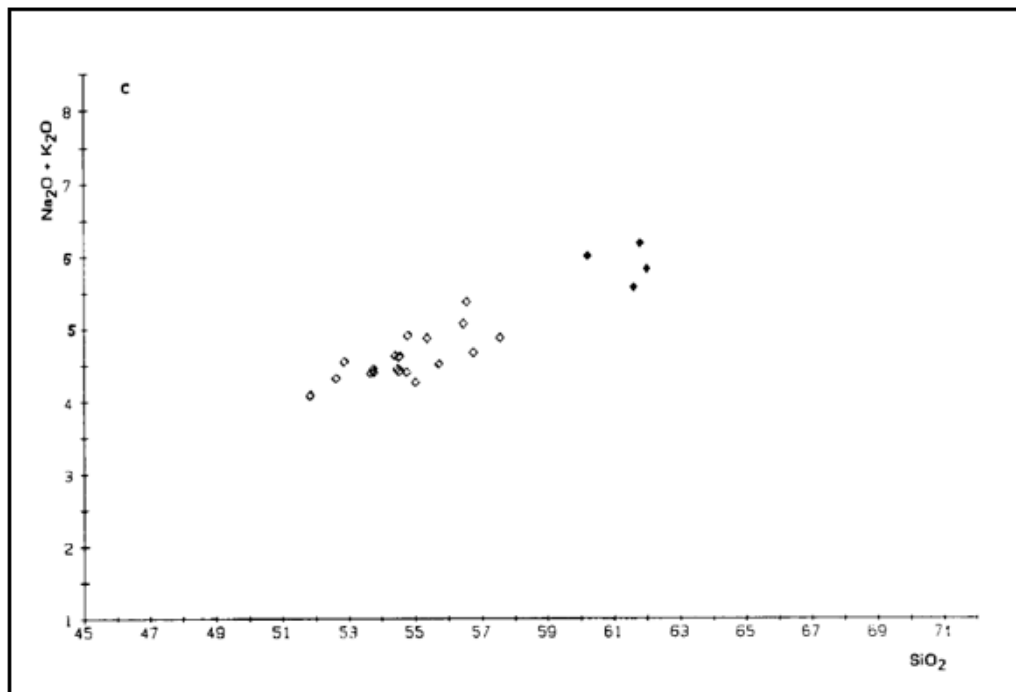
Figure 28: *K_2O + Na_2O versus SiO_2 diagrams; Anak lavas (Camus et al., 1987).*

This evolution trend is also confirmed by (Allard et al., 1981; Gardner et al., 2012); they reported that the composition of Anak Krakatau erupted products evolved from initial basalts, similar to Krakatau basalts to more differentiated products as basaltic andesites, andesite and occasionally dacites. For these authors this evolution implying crystal fractionation in a relatively shallow and/or small magma reservoir.

Recently (Jaxybulatov et al., 2011), through seismic tomography, proposed a complex feeding system underlies Krakatau complex, system that feed also Anak Krakatau. The most interesting result of their study is the distribution of Vp/Vs ratios in the vertical section (figure 29).

Beneath the Krakatau complex they observed a highly heterogeneous structure with two clearly distinguished zones of extremely high Vp/Vs ratio; this fits with an idea of several levels of chambers/reservoirs beneath Krakatau.
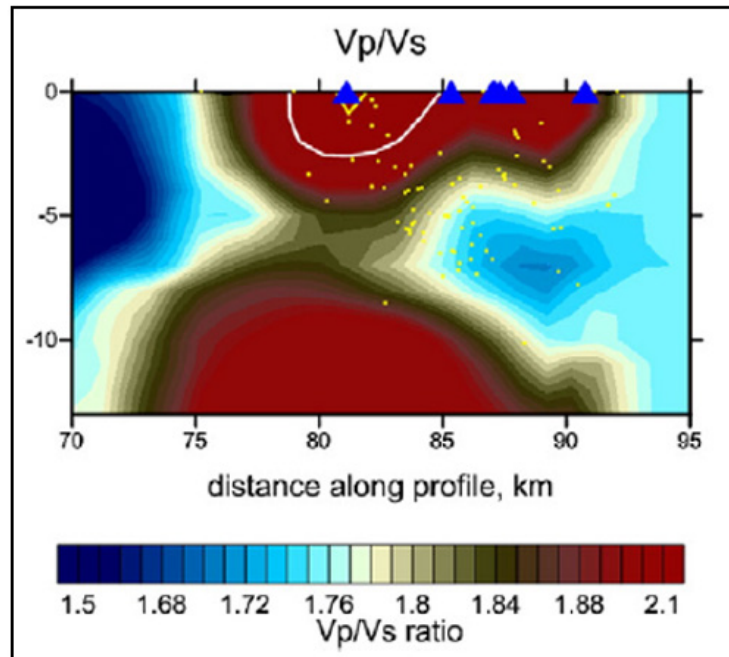
Figure 29: *Vertical sections of the distributions of Vp/Vs ratio obtained from real data inversion; Blue triangles, seismic stations; Yellow dots, final locations of the sources. Zones of anomalously high Vp/Vs ratios are indicated by the white contour line (Jaxybulatov et al., 2011).*

This study was also supported through recent petrological studies by (Dahrén, 2010; Dahrén et al., 2010); they analyzed the mineral chemistry of clinopyroxene and plagioclase in basaltic-andesites erupted from Anak Krakatau. The clinopyroxene-melt and plagioclase-melt geobarometers resulted in two separated sets of depth estimates with very little overlap in-between. This is indicative of at least two broad, but distinct magma crystallization (storage) regions. Considering also the computed depths of plagioclase and clinopyroxene crystallization by (Jaxybulatov et al., 2011), the system appears to consist of two magma reservoirs, one at only 4–6 km depth and a deeper one at 8–12 km. The upper reservoir is made up of multiple discrete and small magma bodies in which crystal fractionation could rapidly occur and influence the composition

of erupted products (Gardner et al., 2012). For (Oemaiya et al., 2019), multi magma-chambers may been created because Krakatau is located in the intersection of frontal subduction collision of Java and oblique collision of Sumatra, then it may made numerous significant fractures.
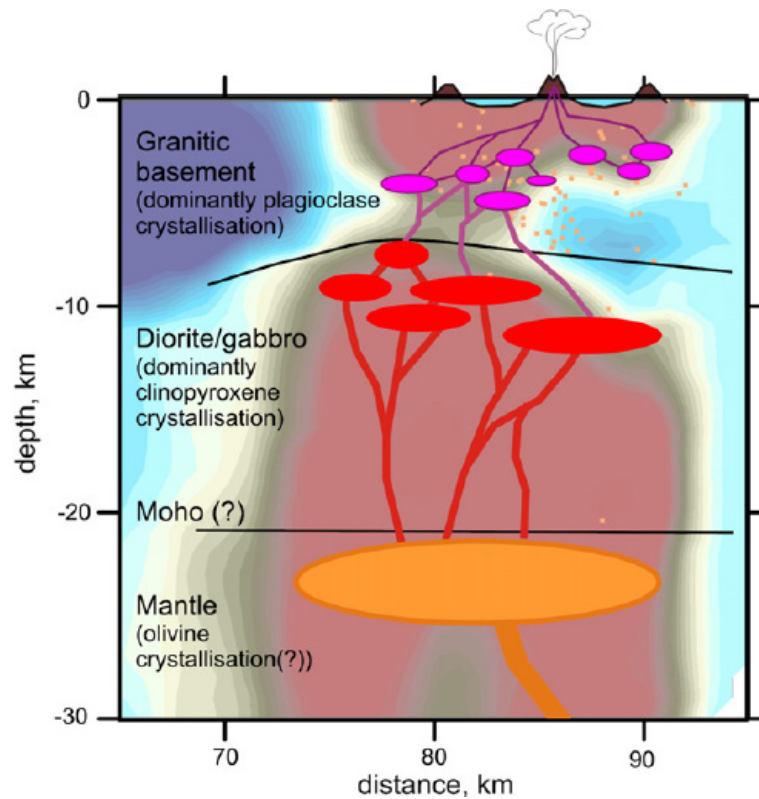
Figure 30: *Interpretation cartoon for the distribution of magma chambers beneath the Krakatau complex. Location of the caldera and the active Anak Krakatau is schematically shown. The background is the distribution of Vp/Vs ratio in the vertical section; Red dots depict the seismicity around the section (Jaxybulatov et al., 2011).*

The depth calculated for plagioclase crystallization (4–6 km) fits well with previously calculated plagioclase crystallization depths (Camus et al., 1987; Mandeville et al., 1996a) and the zone of clinopyroxene crystallization (8–12 km), coincide with the findings of the microseismic study in (Harjono et al., 1989), which identified a magma chamber system at a depth of 9 km. These zones agree remarkably well with lithological crustal boundaries inferred for the bedrock below Anak Krakatau based on

evidence from drill holes (see above), xenoliths and micro-seismic studies (Camus et al., 1987; Hamilton, 1979; Oba et al., 1982; Harjono et al., 1989; Harjono et al., 1991; Mandeville et al., 1996b; Dahrén, 2010; Gardner et al., 2007).

The micro-seismic study by (Harjono et al., 1989) identified three boundaries in the crust below the Anak Krakatau, therefore valid also for the Krakatau complex, with unique crustal velocities which should correspond with lithological boundaries. The upper boundary at 4 km represents the sedimentary-plutonic transition. The boundary at 9 km represents a density contrast that implies a change in lithology from low density (granite) to a higher density plutonic rock (diorite or gabbro) and the lowermost boundary at 22 km represents the Moho.
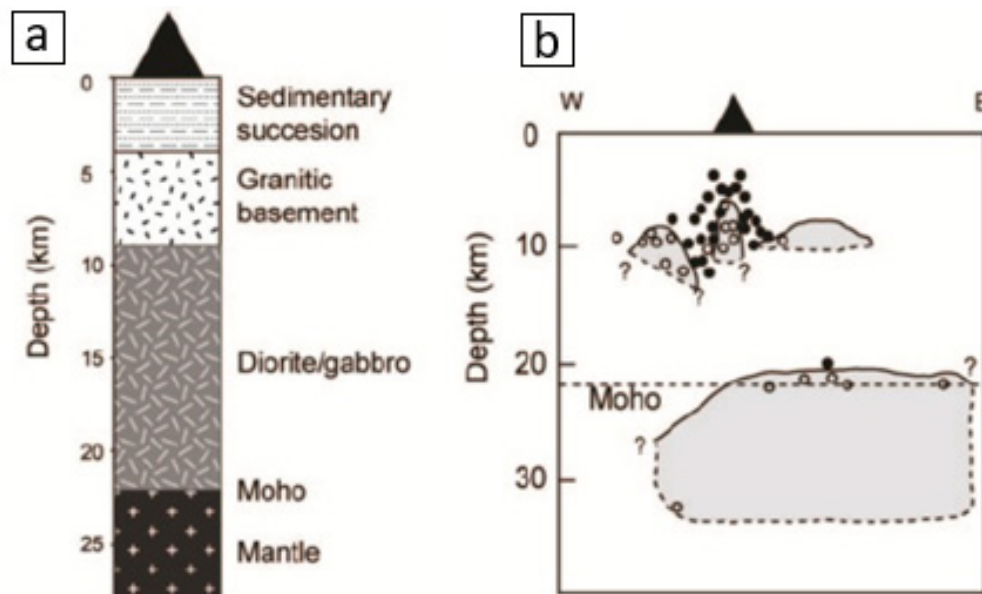
Figure 31: Stratigraphy and cross-section of Anak Krakatau; (a), Inferred stratigraphy of the bedrock below Anak Krakatau. The lithologies are constrained by data obtained from xenoliths (Oba et al. 1982; Camus et al. 1987; Mandeville et al. 1996b; Gardner et al., 2012), drill holes, and seismic studies (Harjono et al. 1989; Kopp et al. 2001); (b), Cross-section through the crust shows seismic attenuation zones detected below Anak Krakatau (redrawn from Harjono et al. 1989); Circles represent earthquake with (open circles) and without (filled circles) S-wave attenuation. The inferred magma storage regions are represented by the grey shapes (Dahrén et al., 2012).

(Dahrén et al., 2012), considering their work and the results obtained by (Camus et al. 1987; Harjono et al., 1989; Mandeville et al., 1996a; Gardner et al., 2007; Gardner et al., 2012; Jaxybulatov et al., 2011), confirmed that magma emplacement and storage at Anak Krakatau volcano coincides with the major lateral lithological boundaries in the crust at 4, 9 and 22 km depth. Density contrasts between the different lithologies is likely a controlling parameter, causing ascending dense magma to stall. Below each of these lithological boundaries, lateral transport will cause magma pockets to grow and evolve further.

The same authors proposed also five steps to explain the Anak Krakatau magmatic plumbing system:

1) Partial melting of the mantle wedge producing a primary basaltic magma, followed by transport of magma to the mantle – crust boundary (22 km depth). For (Harjono et al., 1989), the initial melt composition may be influenced by decompressional melting, due to the extensional character of the Sunda Strait. At this level, crystallization of high anorthite plagioclase and olivine takes place.

2) Ascent of basalt takes place when the density of the magma decreases due to fractionation and became less dense of the lower crust or when there is a new injection of fresh basaltic magma which release volatile in the chambers.

3) The ascending magma then stalls at a mid-crustal level (9 km depth) when it finds the next major density contrast (Granite – diorite transition). At this level, the dominant phase of crystallization of clinopyroxene takes place and all clinopyroxenes analyzed by (Dahrèn et al., 2012) shown euhedral habitus and homogenous composition; for the authors this indicate a sizeable and stable storage region with a semi-continuous supply of magma.

4) Subsequence ascent of magma is triggered by continued crystal fractionation and possibly also assimilation/mixing with felsic crust/magmas. This leads to a new magma density decreases until it became less dense than a density of the middle crust. After this, magma will begin to rise again.

5) At a depth of 4 km, the magma ascent is stalled once more, this time at the granite-sedimentary lithological boundary. At this level, a major phase of An56-76 plagioclase crystallization takes place.

This shallow storage is made up by small and interconnected pockets of magma dispersed in the crust and this pattern is confirmed by (Jaxybulatov et al., 2011) results. For (Dahrèn et al., 2012), at this level that magma evolves to its final pre-eruptive composition.
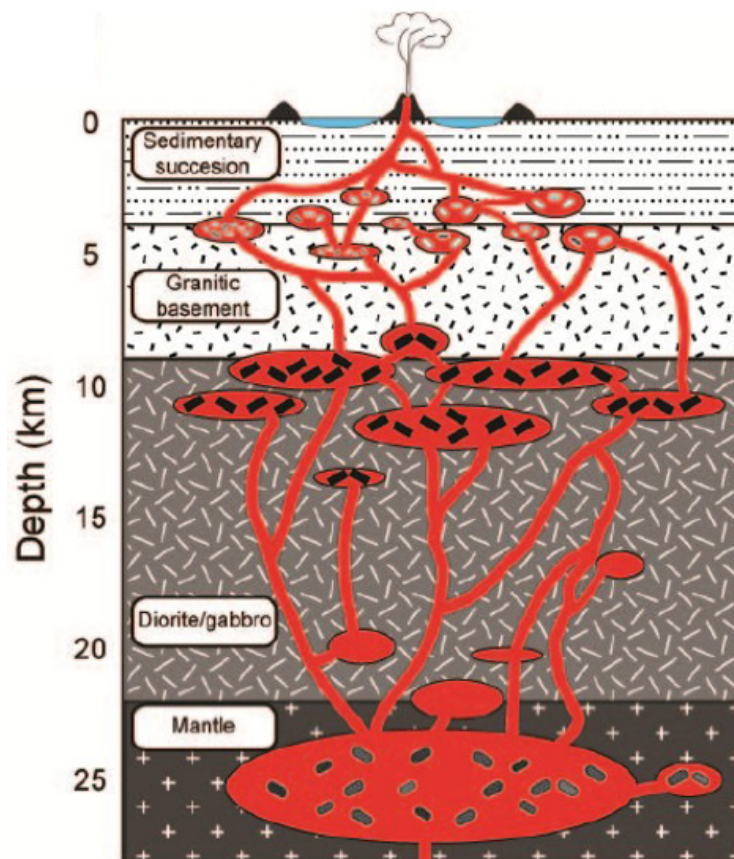
Figure 32: Schematic illustration of the magma plumbing system at Anak Krakatau based on thermobarometric and geophysical data (Dahrèn et al., 2012).

All this additional information confirm that the magma storage regions detected beneath Anak Krakatau coincide with major lithological boundaries in the crust and this is implying that magma ascent at Anak Krakatau is in part controlled by crustal discontinuities (Dahrèn et al., 2012).

4.1 2018 flank collapse

The recent eruption of Anak Krakatau started on 23 October 2007 with minor eruptions that created ash clouds and Plumes and continued with variable eruptive activity until October 2018 when the volcano became more active with strombolian and explosive events (Smithsonian Institute). Satellite monitoring and ground observations reveal that Anak Krakatau was in an elevated stage of activity throughout 2018; an analysis of infrared data recorded by MODIS indicates that a new intense eruptive phase initiated at Anak Krakatau on 30 June 2018. This eruptive phase continued for 175 days until 22 December 2018, when the activity suddenly evolved into a sector collapse and destroyed most of the edifice (Walter et al., 2019). This flank collapse happened at 13:56 (UTC), 115 seconds after the high frequency seismic even (2–8 Hz) recorded by seismic stations and it generated a volcanogenic tsunami with wave propagated in all directions. (Smithsonian Institute; JRC Emergency reporting – European commission, 2018; Walter et al., 2019).
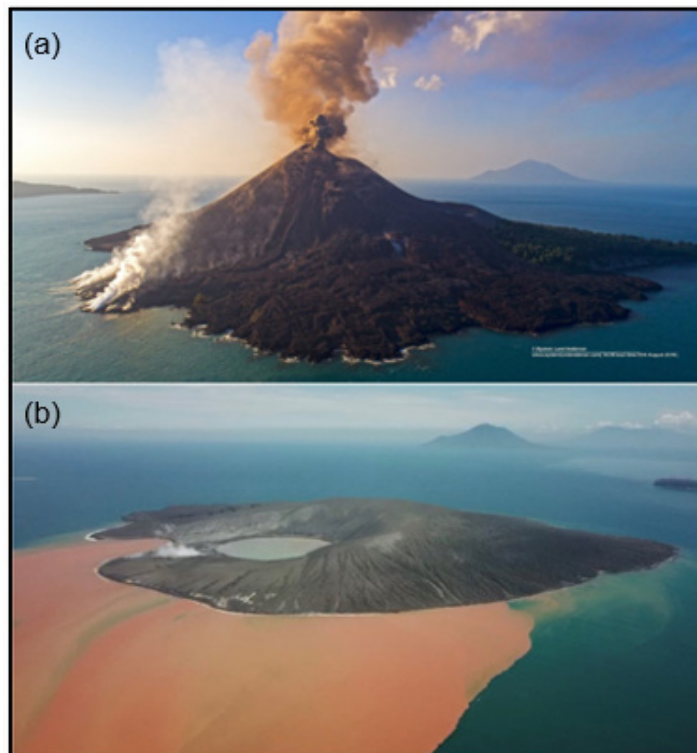
Figure 33: Anak Krakatau before and after the 2018 sector collapse; (a), before; (b), after. (Smithsonian Institute).

The flank collapse was captured in unprecedented detail by remote sensing satellites. The first observation of Anak Krakatau following the flank failure was made by the Sentinel-1A Synthetic Aperture Radar (SAR) satellite, which imaged the volcano at 05:33 on 23 December 2018 (22:33, 22 December 2018 UTC), only 8 hours after the tsunami impacted the coast (Williams et al., 2019).
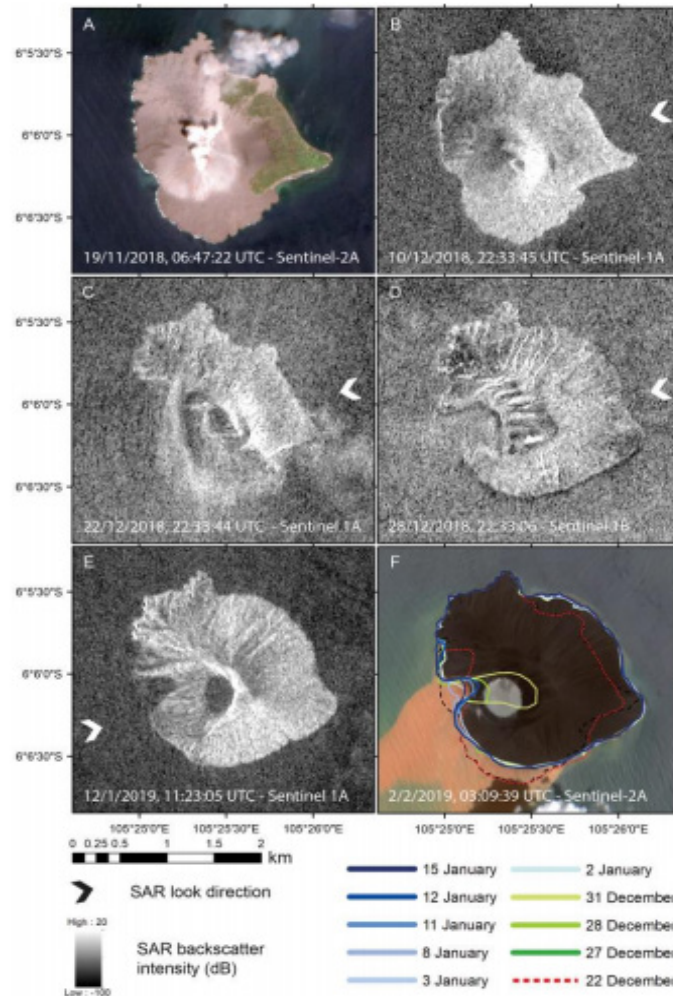
Figure 34: Satellite imagery shows the evolving geomorphology of Anak Krakatau due to the December-January eruptive activity and the 22 December 2018 tsunami; (A-B), island morphology before the flank failure; (C), 8 hours after the tsunami, flank failure and collapse of the summit; (D), destruction of the summit; (E), subsequent regrowth of the island; (F), changes in island surface area through this period. (A-F), are Sentinel-2A true colour images; (B-E), are Sentinel-1A and -1B SAR backscatter images; Arrows show the radar looking direction (Williams et al., 2019).

The aerial photographs showed a sharp, steep-sided cut of the coastal lava deltas to the NW and SE of the pre-collapse vent site. These breaks in the coast constrain the margins of the primary collapse scar on the Sentinel-1A satellite radar images from December 23 (Grilli et al., 2019). The same authors, thanks to the interpretations of radar images, proposed that the opening angle of the headwall scar was very wide, defining a broadly linear collapse that cut behind the vent and, considering the photographs and radar images, they also proposed that to produce such a dramatic change in the volume and shape of the island (reduced area by 49%), the collapse plane evidently extended below sea level. The full extent of the sector collapse initially remained hidden owing to intense post-collapse eruptive activity but became visible when the eruption intensity decreased by 27 December 2018. As a result, a new and steep amphitheater enclosing a deep valley became visible on the southwestern side of the island (Walter et al., 2019).
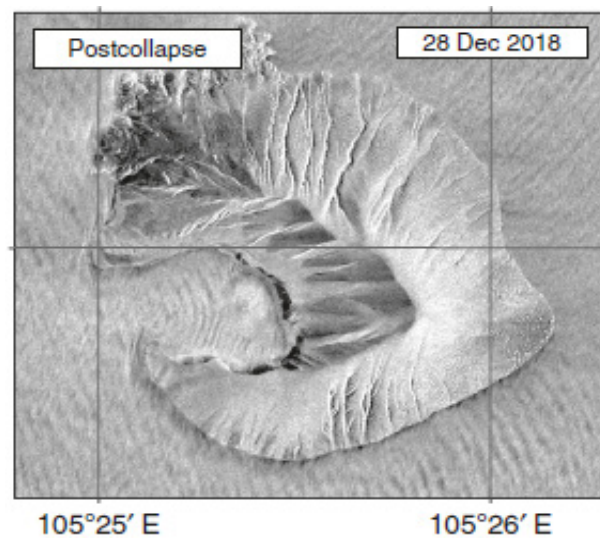
Figure 35: *Terra SAR-X satellite radar images in high-resolution spotlight mode showing the 2018 sector collapse (Walter et al., 2019).*

Profound changes continued to occur in the weeks following the catastrophic event. Numerous small slumps deposited material into the landslide amphitheater and an explosion tuff ring formed inside the decapitated volcano conduit area. The eruption site appears slightly shifted to the SW, hosting a new 400-m-wide water-filled crater (Walter et al., 2019).

(Walter et al., 2019) estimated the erupted volume from thermal data and they obtained that the eruption phase produced 25.5 ± 8.4Mm^3 of deposits, implying a mean output rate of 1.7 ± 0.8m^3 s−1 from June 2018 to just prior to the collapse event; Thus, the load on the summit and especially on the southern flanks of the island, progressively increased over this time by ~ 54 million tons (assuming a mean density of 2110 kgm^{-3}). Instead, considering the volume of the lateral collapse, it is possible to observe that there are several recent works that tried to obtain it.

(Giacchetti et al., 2012) modeled a failure of 0.28 km^3 of the western flank. This value was calculated on 2012 considering only a hypothetical flank collapse directed southwestward. (Grilli et al., 2019) performed a model of the collapse obtaining a volume of 0.27 km^3. This value was calculated considering their best-estimated failure surface. Instead, (Williams et al., 2019) estimated that the flank failure was much smaller in volume; They calculated volumes of 0.004 km^3 (range 0.003 to 0.0045 km^3) for the subaerial failure and in the order of 0.1 km^3 (range 0.086 - 0.093 km^3) for the submarine failure. Finally, (Walter et al., 2019) estimated also a collapse volume of 1.02×10 m^3 (0.102 km^3). For these authors this value is a minimum estimate because was not consider the volume gained by new eruptive deposits which may exceed another 1×10^8 m^3 (0.1 km^3).

Considering all these data, it is possible to observe that the event occurred is not yet clear. With this work, we will try to clarify the lateral collapse occurred and we will try to understand the trigger/triggers of the event through numerical models and interpretation of satellite images.

5 Methods

The procedures adopted to collect the data and the programs used for the development of this thesis project will be explained in detail in this chapter.

5.1 Acquisition of the volcanic activity data

In order to obtain detailed information regarding the activity of Anak Krakatau, therefore regarding its evolution and its morphological changes, different types of data were used. The decision to analyze different types of data is due to the strong activity of the volcano which often obscured the satellite images or made them unclear, preventing the acquisition of the data necessary to understand the occurred events and therefore necessary to build an accurate temporal evolution of the activity of Anak Krakatau before and after the 2018 sector collapse.

In this phase of work to collect the data were used high-resolution satellite images obtained from Planet Labs and Google Earth, satellite instruments based on the use of different sensors able to acquiring thermal emission data or sulfur dioxide emission data (SO_2) which were obtained from MODIS and OMI and it was also used the Global Volcanism Program (GVP)**.** The use of the sensors allowed to acquire data also when the images were obscured. This permitted to collect a large and detailed dataset that was used for the subsequent work phases. All the data used in this thesis project were obtained within the time window between 01/01/2016 to 02/28/2019 which includes the pre and post collapse periods. Methods, software and satellite sensors used will be explained in detail below.

5.1.1 MODIS - MODVOLC

MODIS (Moderate Resolution Imaging Spectroradiometer) sensors are the base of the space-based system for autonomously searching the surface of the Earth for thermal emissions from erupting volcanoes using data acquired from NASA's EOS platforms. MODIS flown onboard the first two EOS platforms, Terra and Aqua, respectively launched in 1999 and in 2002. MODIS can provide 24 h of 'always on'

imaging capability and high temporal resolution, characteristics indispensable for detecting and catalog thermal unrest of eruptions. In addition, MODIS images the Earth using a middle infrared thermal channel centered at 3.959 μm, which allows to make high-fidelity measurements of the spectral radiance emitted by high-temperature targets. This middle infrared spectral passband is used to quantify the energy radiated by active lavas, even when those lavas are much smaller than the 1 km ground sampling size of the MODIS instrument (Wright., 2016).

The data acquired by MODIS are useful to study the global volcanoes activity. For creating a global volcano monitoring system was important to make the data collected easily available to the users. For this reason, some MODIS data products including MODVOLC were created. These products are 'direct readout' products, whereby direct broadcast data are processed in real-time upon reception at the ground to ensure low latency. MODVOLC is an algorithm that became operational on 28 February 2000 and it still operational. It uses infrared satellite data acquired by NASA's MODIS instrument to monitor Earth's surface for the thermal emission signature of volcanic eruptions. Precisely, it analyzes every pixel within every MODIS image that is acquired, and it uses a simple multispectral threshold to detect which pixels within those images contain high-temperature radiators. For each pixel, the details of these "hot spots," including the geodetic location, observation time, and emitted spectral radiance at one midwave infrared (3.959 μm) and two long-wave infrared (11.03 μm and 12.02 μm) wavelengths are recorded. Once the 3.959 μm spectral radiance emitted from each hot spot pixel is collected, it is converted to an estimate of the radiant flux (Wright et al., 2015).

The MODVOLC data give for each thermal anomaly detected: Field 1. Time of observation in Unix time; Field 2. Whether the anomaly was detected by the Terra or Aqua MODIS sensor; Fields 3 to 7. Time of observation in universal time; Fields 8 and 9. Latitude and longitude of the center of the hot-spot pixel (decimal degrees, registered to WGS-84); Fields 10 to 14. At-satellite spectral radiance in the five noted MODIS wave channels in units of W/m2/sr/micron; Fields 15 to 18. The sun-sensor viewing geometry at the time of detection (in degrees); Fields 19 and 20.

The line and sample location in the original MODIS L1B granule; Field 21. The Normalized Thermal Index computed for the anomaly; Field 22. The sun-glint vector (in degrees); Field 23. An estimate of the excess radiant flux in W for that hot-spot pixel; Field 24. The decadal-averaged temperature of Earth's surface at that location computed from the monthly MODIS Land Surface Temperature Product (in K). Field 25. Accuracy of the temperature on field 24. In these files, the saturation of a particular wave-channel is denoted by a flag value of -10.000 (http://modis.higp.hawaii.edu/). Considering some of these channels, the 3.959 µm spectral radiance data and the Radiant Flux data have been collected within the time window between 01/01/2016 to 02/28/2019. Precisely, using the MODVOLC website was set the analyzed time, both MODIS sensors (Terra and Aqua), the daytime and nighttime were considered and finally was set the observation geometry (the sunglint angle and the scan angle) which was left as by default. After downloading the data, they were plotted in Excel for a better view of the whole dataset. This procedure allowed us to obtain daily information regarding thermal emissions of Anak Krakatau therefore regarding lava flows occurred on the island also when the volcanic activity was not visible in satellite images.

5.1.2 Ozone Monitoring Instrument (OMI)

The Ozone Monitoring Instrument (OMI) is one of the instruments presents on the AURA platform. AURA is the chemistry mission of NASA with the overall objective to study the chemistry and dynamics of Earth's atmosphere from the ground. This instrument can distinguish between aerosol types, such as smoke, dust, and sulfates, and measures cloud pressure and coverage. OMI observes Earth's backscattered radiation with a wide-field telescope feeding two imaging grating spectrometers. Each spectrometer employs a CCD detector (780 x 576 pixels) which acquires both visible (350 – 500 nm) and UV (UV-1, 270 to 314 nm, UV-2, 306 to 380 nm) data. The spectral resolution and the spectral sampling are respectively 1.0 - 0.45 nm FWHM and 2-3 for FWHM. Onboard calibration includes a white light source, LEDs, and a multi-surface solar-calibration diffuser. At the end, a depolarizer removes the polarization from the backscattered radiation (https://so2.gsfc.nasa.gov/).

Considering the thesis work, was decided to use OMI because this instrument can detect volcanic ash and sulfur dioxide emission produced in volcanic eruptions with up to at least 100 times more sensitivity than TOMS (NASA's Total Ozone Mapping Spectrometer). The Sulfur dioxide data were obtained using The Global Sulfur Dioxide Monitoring Group website. This group primarily uses UV satellite data from the Ozone Monitoring Instrument (OMI) on NASA's EOS-Aura satellite and the Total Ozone Mapping Spectrometer (TOMS) on multiple satellites. Using this website was possible to set the studied area and the analyzed time window. In this way the program allowed to visualize daily images of the area under examination with the associated SO_2 mass values measured. An example of data obtained is shown below (Figure 36).
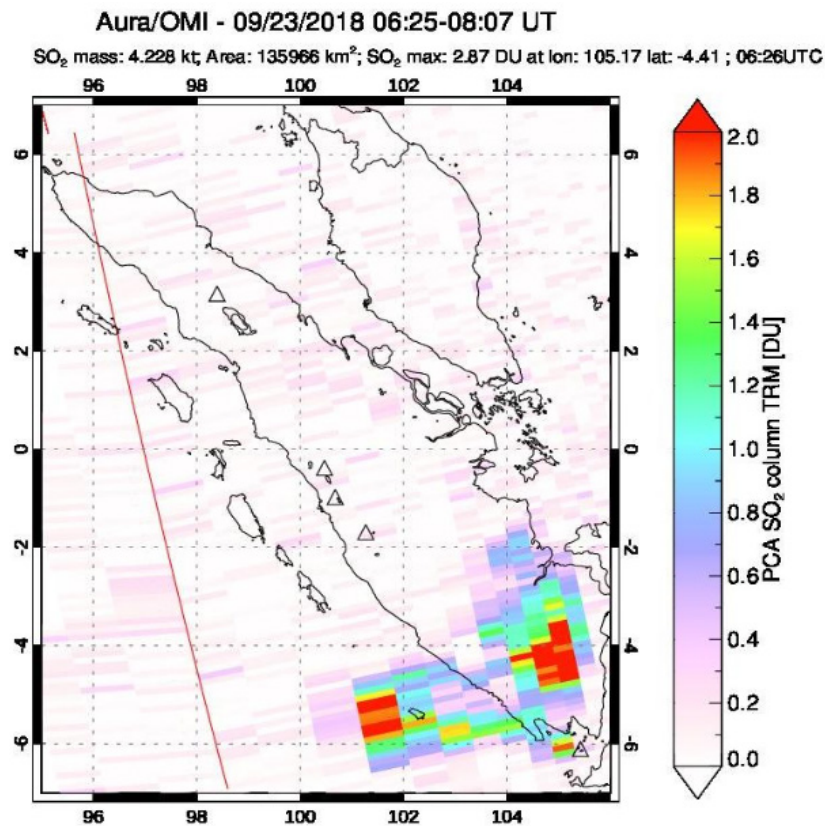
Figure 36: *SO_2 mass detected by Aura/OMI on 23 September 2018 (OMI website).*

This procedure allowed to obtain detailed information regarding the sulfur dioxide emissions (SO_2) from Anak Krakatau and so detect lava flows events occurred on the island also when the images were not clear or were obscured.

5.1.3 Planet Labs

Planet Labs is an American private Earth imaging satellite company based in San Francisco, (CA). Their goal is to image the entirety of the planet daily to monitor changes and evolutions. The company designs and manufactures Triple-CubeSat miniature satellites called Doves that are then delivered into orbit as secondary payloads on other rocket launch missions. Each Dove is roughly 10x10x30cm size, orbiting in two near-polar, Sun-synchronous (SS) orbits with ~8° and ~98° inclination at an altitude of ~475 km and is equipped with a high-powered telescope and a 6600 × 4400 pixel CCD array, which acquires both visible (red–green–blue or RGB) and near-infrared (NIR) PS data with 12-bit radiometric resolution (Aldeghi et al., 2019). Considering all Doves, they form the largest satellite constellation in the world (the CubeSat constellation), that provides a complete image of Earth once per day at 3–5 m optical resolution. The images gathered by Doves are frame images with approximate dimensions of 25 – 30 × 8 – 10 km, and a native spatial resolution of 3.7 m, resampled to 3 m for delivery (Aldeghi et al., 2019). These satellites can provide three types of images; orthorectified multi-spectral 16-bit images, orthorectified 3-bands visual only 8-bit images and not-orthorectified multi-spectral 16-bit images. These images are composed of a variable number of image segments acquired a different time but with the same source. The bands of images cover a variable area and they can be activated or deactivated allowing to download only those covering the desired area. These types of images can be accessed online and some of them are available under an open data access policy by Planet website. During this project, daily photo of Anak Krakatau from 1/1/2016 to 2/28/2019 were analyzed to visualize activity events such as lava flows and morphological or structural changes of the volcano. Every image that showed significant information was selected and then downloaded. Before searching an image, Planet website allows to set various parameters such as the amount of cloud cover desired (0–100%), the amount of the area covered by the image (0–100%), the sun azimuth (0°– 360°), the sun elevation (0°– 90°), the off-nadir angle (-60° - 60°), the sources used by the satellite during the image acquisition (RapidEye Ortho tile, 4band PlanetScope Scene etc.) and it allows also to decide what type of image you want to download (orthorectified

multi-spectral 16-bit, orthorectified 3-band visual only 8-bit or not orthorectified multi-spectral 16-bit). In this phase of work we selected only the image segments that covered Anak Krakatau island, we set up the whole interval of cloud cover as to have all available images, we left as by default all other parameters and we downloaded only images in the orthorectified multi-spectral 16-bit form. This procedure was performed for each image selected for a total of 26 orthorectified images which were considered significant for understanding the activity and the evolution of Anak Krakatau.

5.1.4 Google Earth

Google Earth is a program that renders a 3D representation of Earth based primarily on satellite imagery. The program maps the Earth by superimposing satellite images, aerial photography, and GIS data onto a 3D globe. Google Earth's imagery is displayed on a digital globe, which displays the planet's surface using a single composited image from a far distance. After zooming in far enough, the imagery transitions into different imagery of the same area with finer detail, which varies in date and time from one area to the next. The imagery are obtained from satellites or aircraft. Before the launch of the USGS's Landsat 8 satellite, Google relied partially on imagery from Landsat 7, which suffered from a hardware malfunction that left diagonal gaps in images. Google now uses Landsat 8 to provide imagery in higher quality and with greater frequency. Imagery resolution ranges from 15 meters to 15 centimeters. For much of the Earth, Google Earth uses digital elevation model data (DEM) collected by NASA's Shuttle Radar Topography Mission *(https://www.google.com/earth/)*.

In this thesis project, Google Earth was used to obtain information on the activity and evolution of the volcano when Planet showed obscured or insufficiently clear images. A tool present in the software was used to observe the historical images of a specific area and therefore it guarantees to observe the changes and the events that have occurred over time. This method permits to obtain information on the activity of the Anak Krakatau during the analyzed period.

5.1.5 Global Volcanism Program (GVP)

The Smithsonian Institution's Global Volcanism Program (GVP) is a program devoted to a better understanding of Earth's active volcanoes and their eruptions during the last 10,000 years. The goal of GVP is to document, understand, and disseminate information about global volcanic activity.

During this thesis work, using the Smithsonian website we were able to acquire data and information regarding the activity of Anak Krakatau due to the fact that this institute is able to provide accurate data, reports and images of an eruption. Precisely, Reports are released in two formats: the Smithsonian / USGS Weekly Volcanic Activity Report that provides timely information about current eruptions and the Bulletin of the Global Volcanism Network that provides comprehensive reporting on recent eruptions on a longer time horizon.

For obtain these data was possible to search within the GVP's database the analyzed volcano and so obtained information such as the volcano type, features, evidence of recent activity, location (set using a map), country, rock types present, population within various distance ranges, the availability of images, eruptive history, deformation history, and emission history. All this information allowed to enrich the already obtained database by adding new information or confirming events that occurred on the Anak Krakatau island. This work phase completes the process of acquiring data concerning the detailed understanding of the activity and the evolution of the analyzed volcano.

5.2 Photo interpretation of satellite images

The photo interpretation of satellite images is an accurate procedure that allows to understand what types of events occurred in a specific area, in which number and in what temporal order. For these reasons we decided to carry out the photo interpretation considering the satellite images downloaded from Planet. To interpret the satellite ortho-images was necessary to upload them on ArcMap. The images were delivered broken down into three bands (Red, Green and Blue) so, before performing

the photo interpretation was necessary use the "Composite Bands" tool to obtain the final satellite images. Once the bands have been overlapping was also necessary georeferenced the images because the data where not completely "clear" due to a metadata flag, which means that the areas were only partially rectified with a low alignment of the bands.

The locational accuracy of all the imagery products depends on the quality of the reference data used: Ground Control Points (GCPs) and Digital Elevation Model (DEMs). Additionally, the roll angle of the spacecraft during the image acquisition and the number, as well as the distribution of GCPs within the image, will impact the final product accuracy.

The georeferencing procedure was performed on ArcMap using the "Georeferencing" tool. Precisely, the ortho-image was overlapped on the Base Map (georeferenced global map provided by ArcMap) and it was moved to its correct position through the selection of similar points called Control Points. This process was performed for each image downloaded and to obtain more accurate results the same Control Points were selected.

Once corrected the images was possible to start the photo interpretation using the knowledge acquired during the entire course of study. Inside the ArcMap software all the observed events such as the change of the coastline, the boundaries of the new lava flows, new vents, new fractures were tracked with different colors, were associated with an identification code, were registered the date on which the change was observed and finally they were entered in the database present in the software with all of this information. Within the program the traces were drawn using a different shape (line or polygon) depending on what they identified; this division allowed to calculate the area of the polygon shapes like the lava flows and it allowed to obtain the total length of the segments of the line shapes. In this step, all 26 ortho-images which cover the time period under analysis were georeferenced and interpreted.

5.3 Bathymetry digitization

Once the images have been georeferenced and interpreted was necessary to obtain information about topography under the sea level to build the whole surface present before the lateral collapse. This information was acquired through the study and digitization of bathymetry charts. This procedure allowed to know the depths and geometric information present in the studied area. An example of this information acquired is the shapes of the 1883 caldera or the inclinations of the sides of the volcano. All the information obtained was the key to generate the submerged surface, indispensable for creating the 3D pre-collapse model of the 2018 sector collapse.

In this work phase three bathymetry charts concerning the area under examination were considered and subsequently digitized. Precisely, the bathymetry charts proposed by Izumi Yokoyama., 2015 and by Deplus et al., 1995 were used. Izumi Yokoyama elaborated the British Admiralty Charts surveyed before and after the 1883 eruption of Krakatau (respectively surveyed in 1854 and 1886). Instead, Deplus et al, 1995 elaborated a detailed bathymetric map of the submerged surface in the Krakatau area drawn from data gathered during the MENTAWAI cruise (1990) and from digitized data from existing bathymetric maps.

Once the bathymetric maps were acquired, it was necessary georeferencing them to obtain a correct representation and position of the studied area. Only after this step, was possible to digitalize the maps. The digitalization was performed through the selection and transformation in m (only if necessary) of each depth and through the tracking of each isobath which were represented in the maps with numbers and with solid lines, respectively. The Isobaths were also differentiated with colors according to the depth that they identify to get a better representation. Finally, all these digitalized data were registered in a database present in the software to create a digital file useful for the subsequent work phases. The georeferencing process and the digitization of the bathymetric charts were performed using ArcMap software. An example of what has been obtained is shown below (Figure 37).
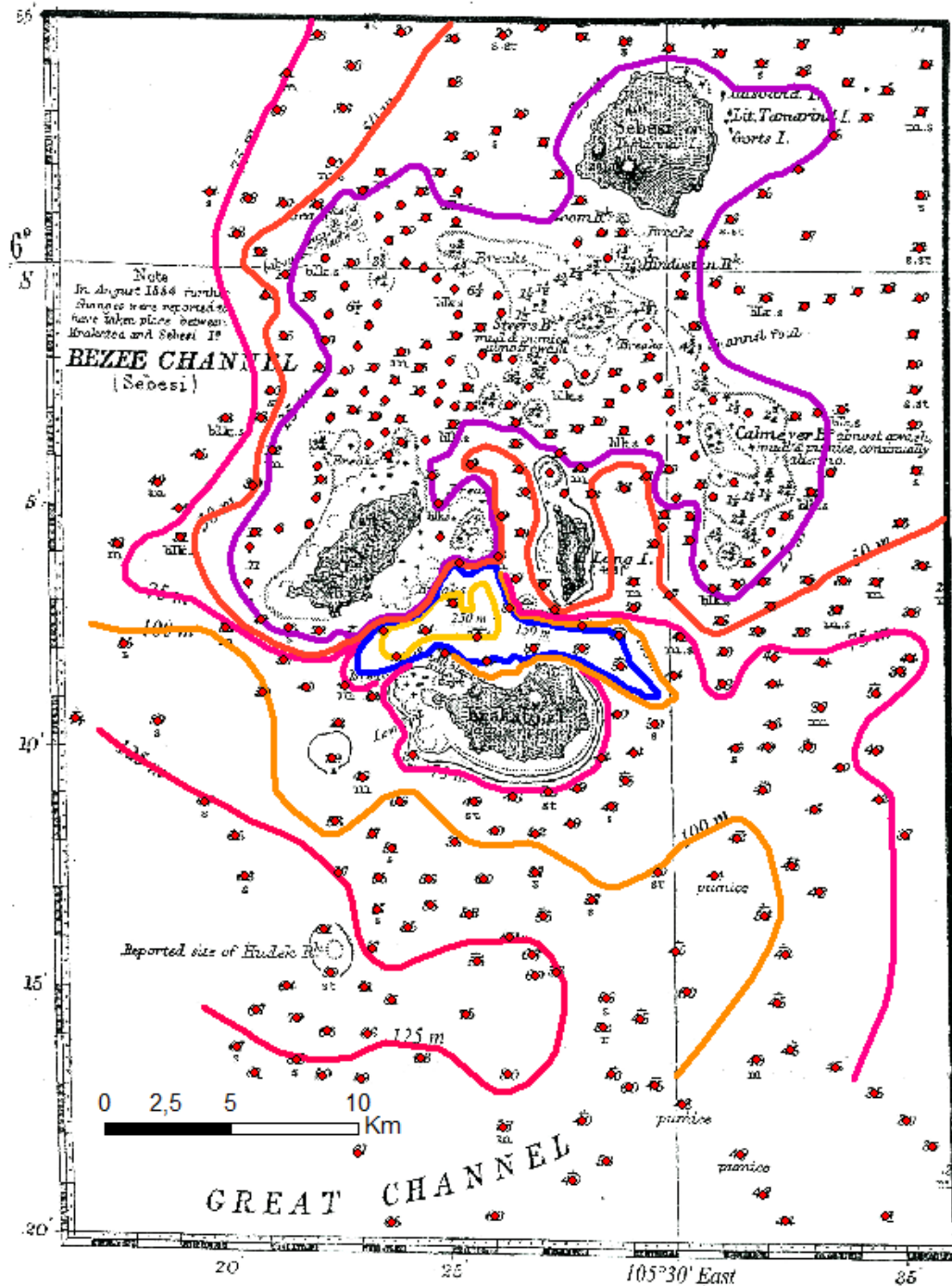
Figure 37: Digitalization of the British Admiralty Chart surveyed in 1886, after the 1883 eruption of Krakatau; The isobaths are added every 25 m by (Izumi Yokoyama., 2015) and the spot depths are in fathom (1 fathom = 1.83 m); Red dots and the colored isobaths are added by the present author during the digitization of the bathymetric chart.

5.4 2018 pre-collapse 3D model of Anak Krakatau

The generation of the pre-collapse 3D digital model of Anak Krakatau is an important phase of this thesis work because it allows to observe the geological, stratigraphical and structural setting that were present before the sector collapse occurred on 22 December 2018. The model was obtained using MIDAS GTS-NX Software.

For obtaining the model was initially necessary to reproduce in 3D the surfaces present in the studied area and below the volcano before the lateral collapse and then was necessary define, through the construction of the geological cross-sections, the geometric, structural and stratigraphical characteristics that were present on the island and below sea level. These data were essential to obtain an accurate reconstruction of the studied area. Methods used for the realization of the 3D surfaces and for the geological cross-sections will be explained in detail below.

5.4.1 Surfaces generation on MIDAS GTS-NX

MIDAS GTS-NX is a comprehensive finite element analysis software package that is equipped to handle the entire range of geotechnical design applications including dynamic and slope stability analysis. The graphical interface allows to create complex 2D and 3D models with high levels of precision and efficiency.

For obtaining the principal 3D surfaces on MIDAS GTS-NX (topographic surface and caldera-forming ignimbrite' surface) was initially necessary to work on ArcMap considering their Raster files which include their positional, geometrical and bathymetrical information and then was necessary to work on AutoCAD. Precisely, the contours lines with intervals every 20 m were obtained using ArcMap and then they have been transformed into 3D considering height (z) as the attribute. Once the 3D contour lines were obtained, was necessary to translate them into the local coordinate system. This process was essential for visualize the surfaces on MIDAS. In addition, in order to obtain a correct representation and a correct overlapping of all surfaces the same translation point was considered. Finally, the translated contour lines were uploaded into MIDAS thus obtaining the principal 3D surfaces of the studied area.

The last step to obtain the complete model was performed directly on MIDAS GTS-NX through the extrusion of the remaining surfaces. All information regarding the surfaces (thicknesses, extensions etc) was obtained considering the bibliography (for the extension of caldera-forming ignimbrite) and considering deep surveys carried out 30 km SE by the company Pertamina/Aminoil in 1973.

5.4.2 Geological cross-sections

Before being able to generate the model was necessary to obtain the geological and stratigraphical information of the studied area. This information was essential to obtain a correct representation of the conditions that were present before the 2018 sector collapse and that may have influenced the event. These lithological, geological, structural and stratigraphical data were obtained from the bibliography (for the extension of the caldera-forming ignimbrite) and from deep surveys and they were represented in two perpendicular geological sections suitably positioned to provide information on the collapsed flank.

The geological sections were obtained through the acquisition of the elevation profiles (profiles that show the emerged and submerged topographic surface and the positions of the principal surfaces under the volcano), directly on ArcMap through the tracing of the section's tracks on the raster files of the studied area. These files were used before and they contain all data obtained during the digitization of the bathymetric chart realized by Deplus and all the information regarding the position and the geometry of the principal surfaces under the volcano. Successively, the 1883 caldera was positioned through the digitization and georeferentiation of the sketch map of Krakatau Islands realized by Self., 1981 (Figure 13B) and afterwards it was slightly modified by the present authors to obtain a better representation of the ring faults (Figure 46). This process allowed to position a key element of the 2018 lateral collapse, and it allowed to obtain accurate geological cross-sections of the studied area.

Once the elevation profiles of the sections and the geometrical and position information of the principal surfaces under the volcano were obtained, they were exported into coordinates and then were uploaded on AutoCAD.

Successively, the remain surfaces were drawn directly on AutoCAD through the consideration of the information obtained from deep surveys and from the bibliography already exposed previously. This last step allowed to draw the two geological sections correctly and it allowed also to represent the materials, thicknesses and structures present in the studied area.

The geological cross-sections obtained allowed to understand the geological, stratigraphical and structural setting present in the area and therefore they allowed to generate an accurate model with all the characteristics and all the parameters that were present before the 2018 sector collapse. This information obtained may have influenced or controlled the occurred event.

6 Results

All the results obtained during this thesis work will be shown and described in this chapter. The results that will be explained were obtained with the methods exposed before and they will be shown as graphics, tables, and mapped satellite images.

6.1 Thermal data and SO_2 emission timeline

The graph shown is the result of the processing of 1221 data acquired by MODIS and 1156 data acquired by OMI within the time window from 1/01/2016 to 02/28/2019. These data represent the Volcanic Radiative Power (VRP) values and the SO_2 emission values measured on Anak Krakatau. The MODIS data includes multiple measurements effectuated on the same day. This graph consists of an x-axis and two y-axes due to the different scales of the considered data. The x-axis represents the analyzed time window, the left y-axis represents the VRP (MW) and the right y-axis represents the SO_2 emissions (kt). Both y-axes are in a logarithmic scale.

Observing the graph, it is possible to notice that the SO_2 data are distributed within the analyzed period except in three temporal intervals which are from 10/28/17 to 01/28/18, from 5/14/18 to 6/21/18 and from 01/19/19 to 02/28/19 in which the SO_2 values are null. Instead, observing the Volcanic Radiative Power data it is possible to notice that are distributed only in the temporal interval from 06/30/18 to 12/22/18 with an exception of two values recorded on 02/17/17 and on 02/18/17.

Analyzing the acquired SO_2 values it is possible to notice that in the period from 01/01/16 to 10/27/17 most of the values are between 0.001 kt and 0.100 kt with a greater concentration between 0.001 kt and 0.030 kt. In this interval, there are only six data that exceed 0.100 kt reaching the values of 0.144 kt, 0.105 kt, 0.891 kt, 0.140 kt, 0.116 kt e 0.147 kt, measured on 3/14/16, 5/10/16, 11/12/16, 11/14/16, 11/16/16 and 7/30/17, respectively. In the period from 01/29/18 to 5/13/18 most of the SO_2 values are between 0.001 kt and 0.250 kt with only two data that exceed 0.250 kt reaching the values of 10.647 kt and 1.400 kt measured on 2/20/18 and 4/7/18, respectively. Finally, observing the period from 6/22/18 to 01/18/19 most of the SO_2 values are between 0.001 kt and 0.540 kt with a greater concentration between 0.001 kt and

0.040 kt. In this period there are different values that exceed 0.500 kt reaching values of 1.144 kt, 4.228 kt, 1.410 kt, 3.712 kt, 6.596 kt, 2.126 kt, 5.070 kt, 4.005 kt, 1.499 kt, 0.736 kt e 0.593 kt, measured on 9/16/18, 9/23/18, 10/9/18, 12/23/18, 12/24/18, 12/25/18, 12/26/18, 12/28/18, 1/03/19, 1/04/19 and 1/06/19, respectively.

Analyzing in detail the Volcanic Radiative Power data it is possible to notice that the two values recorded in 2017 are respectively equal to 55.066 MW and 103.682 MW while most of the values recorded in the 2018 interval are between 1MW and 300 MW with a greater concentration between 1MW and 55 MW. In this period there are eighteen data that exceed 300 MW reaching values of 491.518 MW, 327.159 MW, 1350.740 MW, 699.456 MW, 480.264 MW, 665.317 MW, 1857.799 MW, 788.456 MW, 358.861 MW, 316.165 MW, 377.828 MW, 615.397 MW, 340.025 MW, 602.373 MW, 418.791 MW, 365.868 MW, 395.400 MW e 337.141 MW, measured on 07/12/18, 08/3/18, 9/09/18, 9/15/18, 9/16/18, 9/17/18, 9/22/18, 9/23/18, 9/30/18, 10/9/18, 11/17/18 and 11/18/18, respectively. Finally, within the graph there are 8 green stars that represent the lava flows identified in this project and they occurred on the Anak Krakatau island. Each star is positioned on its corresponding peaks.
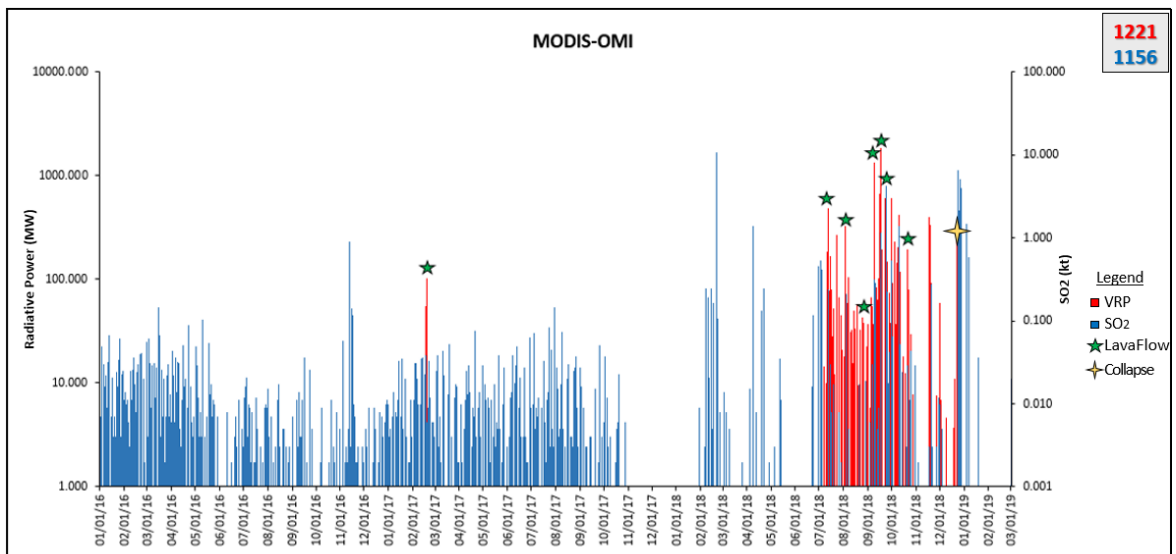
Figure 38: *Time series of the volcanic radiative power (VRP) (red) and SO₂ emission (blue) recorded by MODIS and OMI at Anak Krakatau within the time window from 01/01/16 to 02/28/19; Green stars, show the lava flows occurred on the island in the time window analyzed; Yellow star, represents the eruption day.*

6.2 Lava flows timeline and their features

The image below (figure 39) shows different types of data and information obtained from different sources. These data allow to confirm the lava flows occurred within the time window analyzed. In detail, it is possible to observe that the table is composed by eight columns and eleven rows. The columns represent each lava flow emitted and identified during this work, while the rows show all data obtained from the different sources used.

Considering the first and second rows it is possible to know the eruptive style that was present during the lava flows emission and it is also possible to know precisely the days in which the emission occurred.

Observing the third, fourth and fifth rows it is possible to know if each lava flow has been or has not been identified and therefore confirmed through the use of satellite images obtained by Planet or Google Earth or through the consideration of the information published by Global Volcanism Program (GVP). The confirmation or non-confirmation is indicated with a star or an x, respectively.

Considering the sixth, seventh and eighth rows, it is possible to observe the graphs obtained using the Spectral radiance data, the Radiative Power data and the SO_2 emission data acquired by MODIS and OMI. These graphs contain all values measured over a 6-days interval which it is around the emission day of each lava flow.

Observing in detail the spectral radiance graph it is possible to observe 8 peaks recorded on 18 February 2017, 12 July 2018, 3 August 2018, 31 August 2018, 9 September 2018, 16 September 2018, 22 September 2018 and 20 October 2018 with values equal to 6.652 $W/m^2/sr/\mu m$, 28.371 $W/m^2/sr/\mu m$, 20.067 $W/m^2/sr/\mu m$, 2.584 $W/m^2/sr/\mu m$, 73.844 $W/m^2/sr/\mu m$, 100.679 $W/m^2/sr/\mu m$, 34.729 $W/m^2/sr/\mu m$ and 12.579 $W/m^2/sr/\mu m$, respectively.

Successively, considering the Radiative Power graph, it is possible to observe 8 peaks recorded on the same days just described but with different values. The measured values are equal to 103.682 MW, 491.518 MW, 327.159 MW, 37.319 MW, 1350.740 MW, 1857.799 MW, 615.397 MW and 197.055 MW, respectively.

Instead, considering the Sulfur dioxide emission graph is possible to observe 7 peaks recorded on 17 February 2017, 12 July 2018, 4 August 2018, 9 September 2018, 16 September 2018, 23 September 2018 and 21 October 2018 with values equal to 0.039 kt, 0.237 kt, 0.208 kt, 0.317 kt, 1.144 kt, 4.228 kt e 0.03 kt, respectively. The ninth row allows to know the volume of emitted material from each lava flow identified.

The volumes were calculated by measuring the area of each lava flow on ArcMap and successively multiplying it by an average thickness of 10 m. The thickness was defined considering the basaltic nature of the erupted products.

Precisely, the lava flow of 18 February issued a volume equal to 649910 m^3, the lava flow of 12 July equal to 885880 m^3, the lava flow of 3 August equal to 978860 m^3, the lava flow of 31 August equal to 245830 m^3, the lava flow of 9 September equal to 749720 m^3, the lava flow of 16 September equal to 1613350 m^3, the lava flow of 22 September equal to 2728510 m^3 and the lava flow of 20 October equal to 414630 m^3. Considering all lava flows, the total issued volume and therefore the total load exerted on the volcano is $8.2x10^6$ m^3.

The tenth row allows to know the days analyzed for each lava flow and the eleventh row allows to observe the lava flows identified and analyzed in this work through the use of eight previews in which it is possible to observe the mapped lava flows, their dimensions and forms and the area where they flowed and cooled.

Eruptive style (a)	Strombolian	????	Strombolian	Strombolian	????	????	Strombolian	Strombolian
Lava Flows emission (a)	17-18 Feb 2017	12 July 2018	3-4 Aug 2018	30-31 Aug 2018	9 - 10 Sept 2018	16-17 Sept 2018	22 - 23 Sept 2018	20 - 21 Oct 2018
(GVP) (a)	★	★	★	✖	★	★	★	★
Google Earth (b)	✖	✖	✖	✖	✖	✖	✖	✖
Planet Data (c)	✖	★	✖	★	★	★	✖	★
$3.959\mu m$ Spectral Radiance (W/m2/sr/μm) (d)								
Radiative Power (MW) (d)								
Sulfure Dioxide Emission (kt) (e)								
Volume (m3) (f)								
Periods Analyzed	15-20 Feb 2017	10-15 Jul 2018	1-6 Aug 2018	29 Aug-3 Sept 2018	7-12 Sept 2018	13-18 Sept 2018	19-24 Sept 2018	18-23 Oct 2018
Preview (f)								

Figure 39: *Timeline of the Lava flows of Anak Krakatau and their main physical and volcanological features during the period from 01/01/16 to 02/28/19. Data sources: (a), Smithsonian Institution Global Volcanism Program (GVP); (b), Google Earth data coverage; (c), Planet Labs data coverage; (d), MODVOLC website; (e), OMI website; (f), ARCMAP data process.*

6.3 Lava flows

The images shown below allow to visualize the temporal sequence of the lava flows occurred in the time window analyzed. Eight lava flows were identified from 17 February 2017 to 21 October 2018. Precisely, the lava flows shown occurred on 17-18 February 2017, 12 July 2018, 3-4 August 2018, 30-31 August 2018, 9-10 September 2018, 16-17 September 2018, 22-23 October 2018 and 20-21 October 2018. These events are indicated in this project with the letters a, b, c, d, e, f, g, h, respectively.

The lava flows were identified as explained before and they were mapped on satellite images obtained by Planet using ArcMap software. It is important to notice that the satellite images acquired in the days of the lava flows' emissions were not always available or usable due to different causes such as the invisibility of the image due to the rise of the plume or unclear image which prevented the identification of the lava flow. For this reason, the first available images that had high resolution and sharpness were used in order to perform this step of work with the most precision and accuracy. Precisely, the images used for the mapping of the lava flows were those acquired on 03/09/18, 07/23/2018, 08/10/2018, 08/31/2018, 09/14/2018, 09/17/2018, 09/29/2018 and 10/22/18, respectively. The mapping of the lava flows was performed with precision by tracing the flow limits visible in the acquired satellite images. These flow limits have been represented using red polygons with a marked border to better highlight the shapes of the flows.

Analyzing the images, it is possible to observe that all mapped events affected the southwest, south-southwest and south sides of the volcano, creating an overlap of material and, only in one case, creating an expansion of the coastline. Comparing all the images it is also possible to observe that all lava flows were originated from the summit crater which was constantly moving and changing due to the rapid evolution of the volcanic edifice. Finally, analyzing the images individually, it is possible to observe that the lava flow that occurred between 17 and 18 February 2017 (Figure 40, a) flowed in the SE direction and it covered an older lava flow that is clearly visible in the image and it is identifiable by the dark red color. This new lava flow with an area equal to 64991 m^2 has flowed beyond the base of the volcanic cone but it has not reached the coastline.

The lava flow that occurred on 12 July 2018 (Figure 40, b), flowed in the S direction and it reached the coastline. This lava flow was larger than the previous one, precisely it had an area equal to 88588 m^2. Observing the third image (Figure 40, c), it is possible to notice that the lava flow that occurred between 3 and 4 August 2018 flowed in the SW direction and it has passed the coastline, creating an expansion of the island that is clearly visible in the satellite image. This lava flow had an area of 97886 m^2.

The lava flow that occurred between 30 and 31 August 2018 (Figure 40, d), flowed in the S direction and it has reached only the base of the cone. This lava flow with an area of 24583 m^2 was the smallest flow that occurred within the analyzed period. Considering the next lava flow that occurred between 9 and 10 September 2018 (Figure 41, e), it is possible to observe that it flowed in the SSE direction and it partially covered the first two lava flows analyzed. This lava flow had an area of 74972 m^2 and it reached the coastline.

Considering the lava flow that occurred between 16 and 17 September 2018 (Figure 41, f), it is possible to notice that it flowed in the S direction and it created the second largest event mapped in this work. This lava flow had an area of 161335 m^2 and it reached the coastline but did not cross it. The event just described was mapped on an unclear image which showed only the volcano partially. This image was chosen because it was the only available image that showed the lava flow. Unfortunately, the successive images could not be used due to the strong volcano activity which quickly covered this lava flow. In the missing side of the image there is the DEM's portion of the island used to georeferenced the image. This portion allows us to observe the perfect overlay obtained between the satellite image and the DEM of the island during this thesis work and that is present in all the images shown.

Considering the penultimate lava flow that occurred between 22 and 23 September 2018 (Figure 41, g), it is the largest lava flow produced in the time window analyzed. This lava flow had an area of 272851 m^2, it flowed in the S direction and it expanded in SW, SSW, SSE and SE directions until it reached the coastline in several points. Finally, considering the last lava flow that occurred between 20 and 21 October 2018 (Figure 41, h), it is a small lava flow with an area equal to 41463 m^2 and it flowed in the S direction, reaching the base of the volcanic cone. In conclusion, considering the whole analyzed period it is possible to notice an increase in the frequency of the lava flows' emission with events that have mostly happened since September 2018. This period coincides with the period of the greatest activity shown by the MODIS-OMI graph that preceded the 2018 sector collapse.

Figure 40: *PlanetScope Images collected between February 2017 and August 2018, showing the chronological sequence of the lava flows (red) that occurred on the island of Anak Krakatau within the analyzed interval. (a), 17-18 February 2017; (b), 12 July 2018; (c), 3-4 August 2018; (d), 30-31 August 2018; Lava flows were mapped with ARCMAP software.*
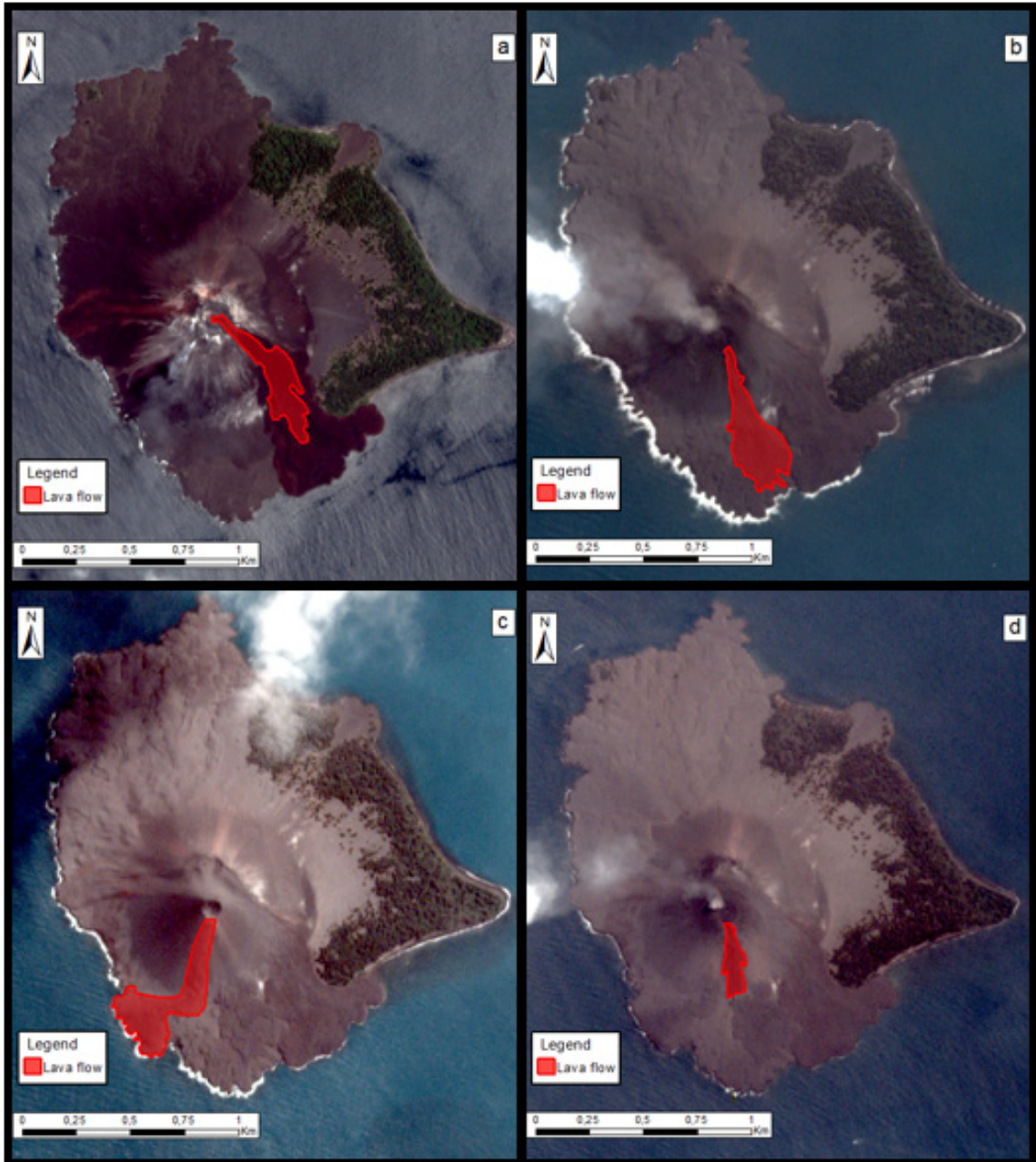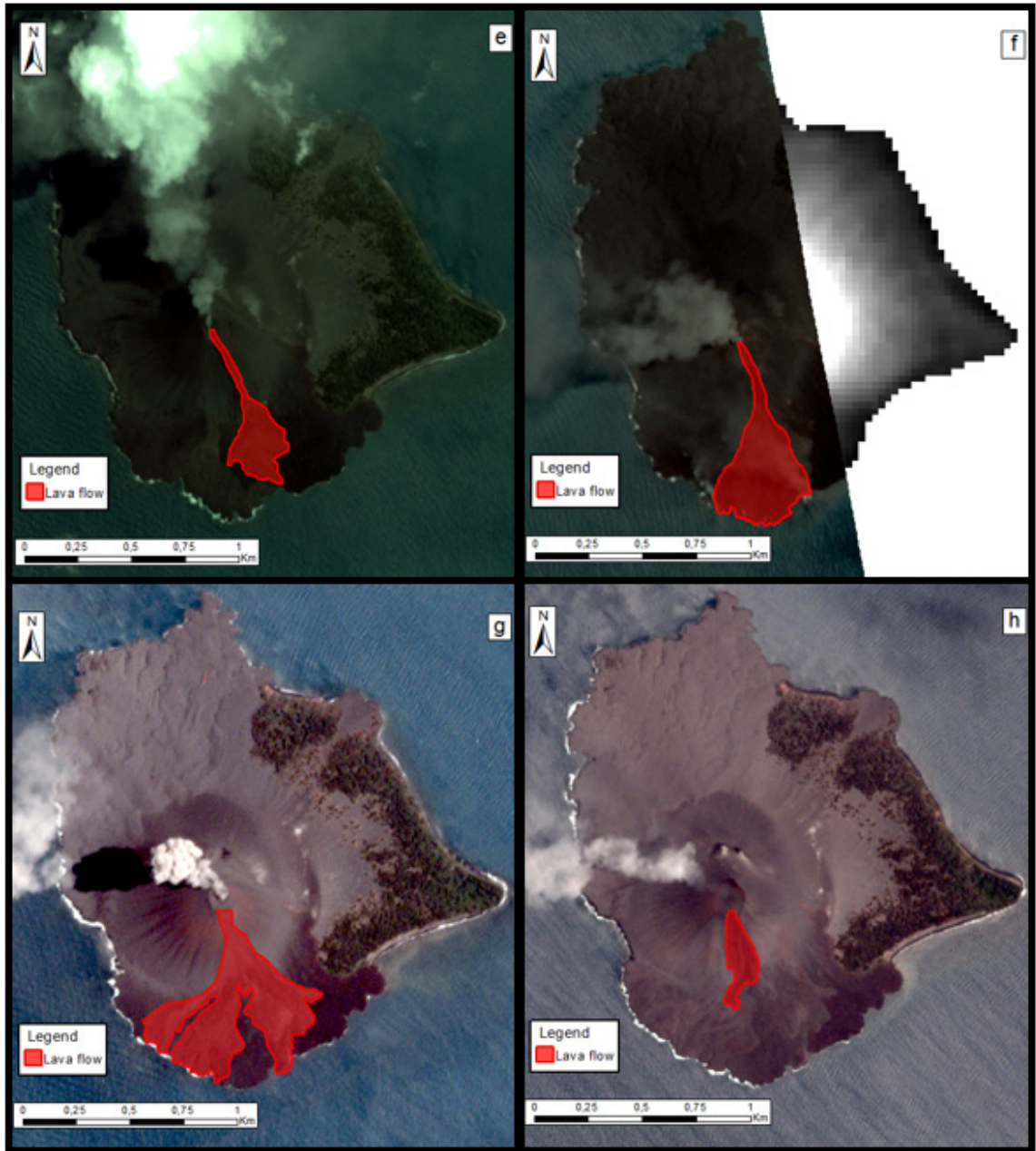
Figure 41: PlanetScope Images collected between September 2018 and October 2018, showing the chronological sequence of the lava flows (red) that occurred on the island of Anak Krakatau within the analyzed interval. (e), 9-10 September 2018; (f), 16-17 September 2018; (g), 22-23 September 2018; (h), 20-21 October 2018; Lava flows were mapped with ARCMAP software.

6.4 Spatial and temporal evolution of the upper cone area

Observing the data and the images considered in this thesis project it is possible to understand that Anak Krakatau is a highly active volcano which in the last three years has greatly increased its activity and its evolution.

Analyzing all acquired PlanetScope images, the morphological changes of the summit crater and the generation of new fractures are observable on the volcano during the whole analyzed period. Precisely, a continuous shift and modification of the position and shape of the summit crater and the creation of extensional fractures were observed. Both events affected only the upper portion of the volcanic cone. Craters and fractures will be explained in detail below.

6.4.1 Craters

The images below show all the craters with elongated shapes generated in the analyzed period and selected from the PlanetScope images. In these images the craters are represented using a chromatic yellow scale. The scale is based on the use of the dark yellow for the identification of the older crater and the light yellow for the identification of the most recent one. These procedures regarding the mapping and the use of a chromatic scale allowed us to know the spatial and the temporal evolution of the craters. The satellite image used was acquired on 08/31/2018 because it permitted a better visualization of all craters and their shapes.

Analyzing the images in detail, it is possible to observe that the image (a) allows to view all the selected craters, their shapes and their locations which always appears to be on the top of the volcanic cone. Considering the image (b), it is possible to observe a zoom of the upper part of the cone which allows a better observation and analysis of the eight selected craters. In this image is also indicates the development day of each crater considered. Precisely, the image (b) shows that the first selected crater (1) has formed on 11/27/16. This crater had an elongated shape in the E-W direction, and it was located on the top portion of the north flank of the volcanic cone. The crater (2) successively selected has formed on 09/03/18, it had an elongated shape in the

E-W direction, and it was positioned on the top portion of the SSW flank of the cone. The generation of two new craters (3 and 4) was observed on 6/20/18 which were positioned on the summit part of the W and NW flanks of the cone and they had elongated shapes in the E-W direction. The crater (5) successively selected has formed on 07/28/18, it was positioned on the summit part of the NE flank of the volcanic cone and it had an elongated shape in the NW-SE direction. This crater is the largest of those considered. The last three selected craters (6, 7, 8) have generated on 09/14/18, on 10/22/18 and on 11/24/18, they had similar elongated shapes in the N-S direction, and they were positioned in the same area on the top of the volcanic cone. Considering their similar shapes was possible to differentiate them only through the observation of their dimensions. Precisely, the crater formed on 09/14/18 was the smallest while the one formed on 10/22/18 was the largest.
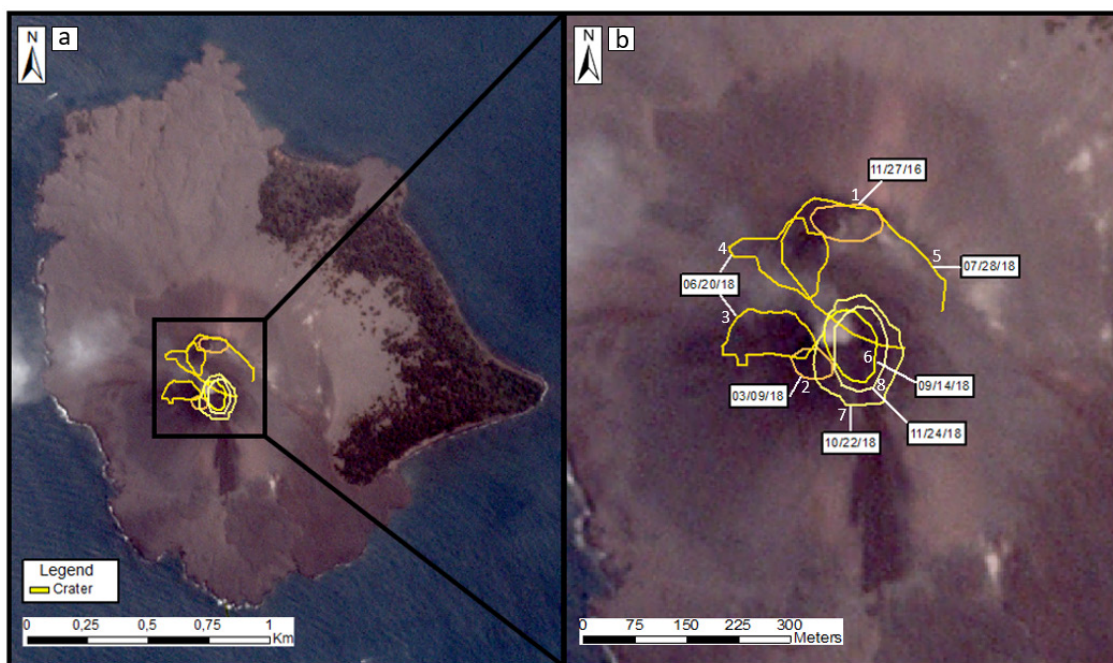
Figure 42: PlanetScope image shows the migration of the summit crater on Anak Krakatau from November 2016 to November 2018. (a) whole island with the location of the craters; (b), Zoom of the upper cone area. The craters generation timeline is represented by numbers and by the yellow chromatic scale (dark yellow = oldest crater; light yellow = recent crater); The dates show the days of crater development. The craters were mapped with the ArcMap software.

6.4.2 Fractures

The images below show the fractures generated in the analyzed period which were selected from the PlanetScope images and they represented using a chromatic orange scale. The scale is based on the use of the dark orange for the identification of the older fracture and the light orange for the most recent one. These procedures regarding the mapping and the use of a chromatic scale allowed us to know the spatial and the temporal evolution of the fractures. The satellite image used was acquired on 10/08/2018 because it permitted a better visualization of the fractures and their traces.

Analyzing the images in detail it is possible to observe that the image (a) allows to view all the generated fractures, shapes and directions and their locations which always appears to be on the top of the volcanic cone. Considering the image (b), it is possible to observe a zoom of the upper part of the volcanic cone which permits a better observation and analysis of the six fractures generated in the months before the collapse. In this image is also indicates the development day of each fracture. The image (b) shows that the first two fractures (1, 2) have developed on 07/01/18. These fractures were located on the Nord and Nord-West flanks of the volcanic cone. The fracture 1 was located on the Nord flank of the cone with 550 m long trace that began to propagate close to the NW base of the cone and it reached the middle of the E side of the cone, passing through the top of the volcano with an approximately constant NW-SE strike. The fracture 2 was located on the West flank of the cone with 228 m long trace that began to propagate close to the base of the cone and it reached the top with an SW-NE strike. This fracture ends in contact with the previous one. The fractures successively observed (3, 4, 5) have developed on 8/10/18. The fracture 3 has created in the same area of the fracture 1 but with a slightly different position and direction. This 336 m long fracture was most positioned on the summit part of the volcano with the trace that has developed from the upper part of the W flank to the half of the E flank and with a non-constant strike. Precisely, the direction was orientated to SW-NE on the west side of the trace, while the remaining part of the fracture was orientated towards NW-SE. The fracture 4 was located on the top of the NNE flank of the cone, it was 69 m long and it has developed in the SSW-NNE direction. This fracture intersected the traces of the fractures 1 and 3 just explained

and it has stopped immediately after. The fracture 4 is the smallest fracture identified and analyzed in this project. The fracture 5 has developed on the South flank of the volcanic cone with an SSW-NNE strike. This 373 m long fracture has developed from the S base of the cone to the top of the volcano with a 132 m long splay located in the lower part of the south side of the cone which had a N-S strike. Considering the position and the strike of this fracture, it is presumably to think that it is the continuation of the fracture 4. Finally, considering the last fracture identified (6), it is possible to observe that it was located on the summit of the volcanic cone with the end parts of the fracture trace that intersected the W and E side of the cone, reaching both the half of the flanks. This 400 m long fracture has W-E strike and, through the observation of the PlanetScope images, was possible to understand that it was an eruptive fissure and that it was the last fracture developed on the volcano before the lateral collapse.
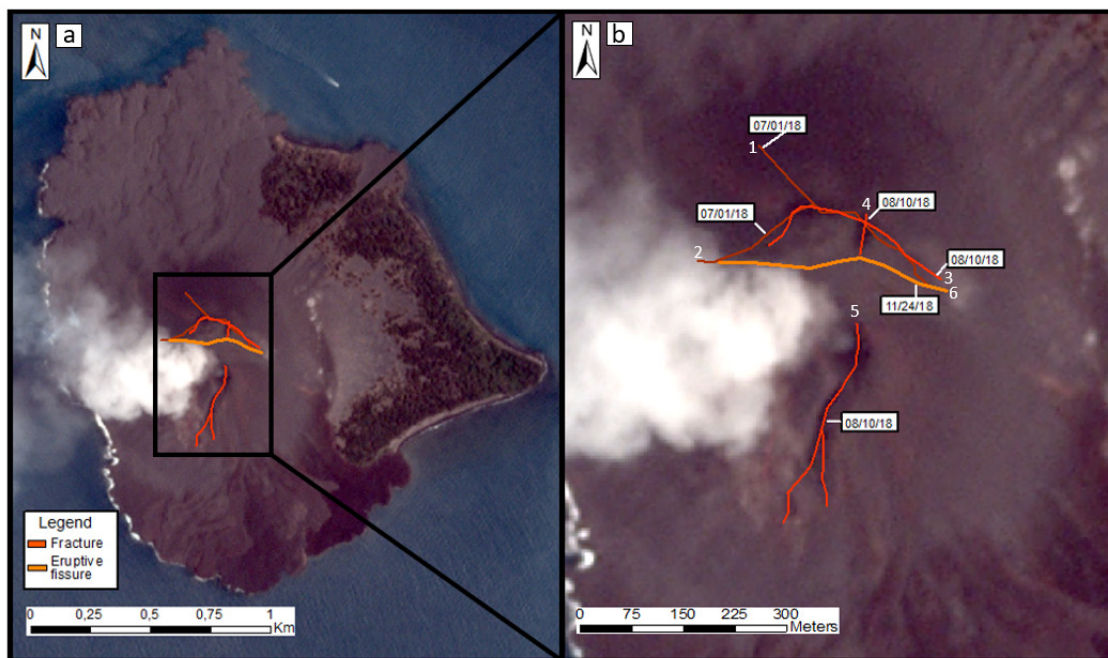
Figure 43: *PlanetScope image shows the fracture generation on Anak Krakatau from July to November 2018. (a) whole island with the location of the fractures; (b), Zoom of the upper cone area. The fracture generation timeline is represented by numbers and by the orange chromatic scale (dark orange = oldest fracture; light orange = recent fracture); The dates show the days of fractures development. The fractures were mapped with the ArcMap software.*

6.5 2018 pre-collapse 3D model

The results relating to the 2018 pre-collapse model of Anak Krakatau will be shown in this chapter. Precisely, the conceptual geological sections obtained and used for the construction of the model and the pre-collapse 3D model will be shown.

6.5.1 Geological cross-sections

The images below show the plane view of the geological cross-section's traces and the respective conceptual cross-sections obtained. Considering the image 44, it is possible to observe the presence of two perpendicular traces (A-A' and B-B') which are drawn on the bathymetric chart obtained by Deplus. These traces are respectively oriented in the SW-NE and SE-NW directions, intersecting the volcanic cone with the aim of showing and analyzing the collapsed flank. The choice to create geological sections which intersect the entire archipelago of Krakatau allowed to reconstruct the whole area that was present before the 2018 lateral collapse. The image shows also the strike and the dip of the structure presents on the analyzed volcano.

Figure 44: *Plan view of the geological section's traces (black); Letters show the tip points of the sections; Simbol and numbers show the strike and the dip of the structure; Solid red line show the 1883 caldera. The surface (grey) was generated on ArcMap considering the bathymetric chart of Deplus et al., 1995.*

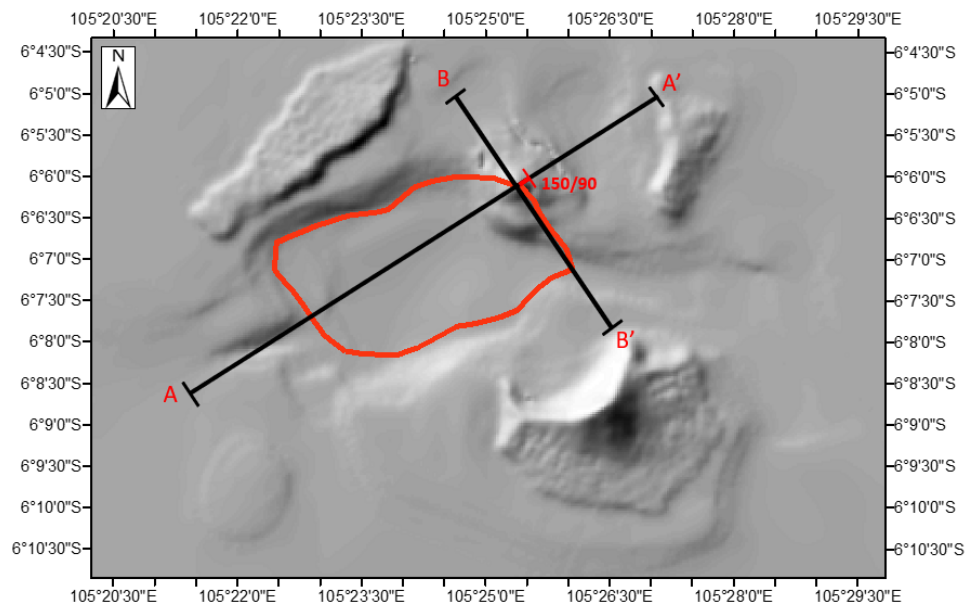The following images (Figure 45, 46) show the conceptual geological cross-sections obtained in this project. In these sections are represented the materials with their thicknesses and the structures (ring faults, magmatic plumbing system etc.) that were present on the volcano and in the whole analyzed area. The sections show also the 1883 caldera with its position and its geometry which was positioned through the digitization and georeferentiation of the sketch map of the Krakatau Islands realized by Self., 1981 (Figure 13B) and it was subsequently slightly readjusted to obtain the best position of the ring faults.

The conceptual geological cross-section (A-A') has a length of 11000 m and it extends for 9100 m below sea level and 400 m above it. Considering the emerged portion of the section it is possible to observe the 265 m hight Anak Krakatau island which is formed by basaltic material. The section shows also the structure located on the eastern side of the volcano, indicating its strike (N150°E) and its dip (90°). Considering the submerged portion of the section, it is possible to observe the submerged topographic surface that was present before the 2018 lateral collapse, the position and the geometry of the 1883 caldera with its ring faults, the materials with their thicknesses and their stratigraphical relationships and the magmatic plumbing system. Observing in detail the submerged topographic surface is notable that it is deeper to the west of the volcano rather than to the east, reaching depths of 240 m and 100 m, respectively. In addition, the surface present to the west allows to analize the slope of the southwest flank of Anak Krakatau which has an averege values of 22°. Instead, considering the southwest volcanic side and the submerged northeast sidewall of the 1883 caldera, it is possible to observe that the slope reaches an average value of 29°.

Considering the 1883 caldera is possible to notice that it is principally located to the west of the volcano with its vertical ring faults which reach the granit basment at a depth of 5000 m. The western fault is positioned at 1950 m from the origin of the section while the eastern fault is positioned at 7500 m from the same origin and it coincides with the east side of the magmatic ascent conduit. This caldera has a width of 5550 m.

Considering the stratigraphical information obtained from this section, it is possible to observe that in the areas outside of the caldera, which extend from 0 to 1950 m and from 7500 m to 11000 m along the x-axis, there is the same stratigraphical sequence except for the presence of pillow lavas with a variable thickness between 70 m and 240 m at the roof of the eastern portion. This stratigraphical sequence is composed of 60 m of caldera-forming ignimbrite that is stratigraphically above of 600 m of unconsolidated marines clays which reaches a depth of 660 m. Stratigraphically below there are 3400 m of clay-dominated siliciclastic rocks interbedded with volcanoclastic material which reaches a depth of 4060 m and then, below this layer there are 5000 m of granitic basement which extend to the bottom of the section.

Considering the 1883 caldera, which is between the ring faults explained before, it is possible to notice the presence of the same stratigraphical sequence with the same thicknesess just described but with a difference at the roof of it. Precisely, it is possible to observe the presence of the thicker portion of the pillow lavas (240 m) which are stratigraphically above of 200-230 m of caldera-formirming ignimbrite. This material is mostly depositated inside of the caldera rather than in the external areas, reaching thicknesess almost 4 times greater.

The caldera-forming ignimbrite fills the entire caldera reaching both the ring faults. It is important to notice that the entire stratigraphical sequence inside of the caldera is lowered by 300 m due to the displacement along the ring faults except for the caldera-forming ignimbrite and for the pillow lavas which are at the roof of the sequence. The caldera-forming ignimbrite was deposited during the strong activity associated with the 1883 eruption and the pillow lavas are post-calderic materials that are located only below the volcano and they constitute the last depositated materials which have welded the caldera.

In conclusion, a simplified vertical magmatic plumbing system was represented which is originates from a small reservoir located at a depth between 5000 m and 5500 m. This magmatic conduit develops until it reaches the summit of the volcano and it is positioned in contact with the eastern ring fault of the caldera.

Figure 45: *Conceptual geological cross-section (A-A') of Anak Krakatau. Distances and depths are represented in meters.*

The conceptual geological cross-section (B-B') has a length of 6900 m and it extends for 9100 m below sea level and 400 m above it. Considering the emerged portion of the section it is possible to observe the island of Anak Krakatau which has an height of 260 m and it is formed by basaltic material. Considering the submerged portion of the section, it is possible to obseve the submerged topographic surface that was present before the 2018 lateral collapse, the position and the geometry of the 1883 caldera with its ring faults, the materials with their thicknesses and with their stratigraphical relationships and the magmatic plumbing system. Observing in detail the submerged topographic surface is observable that it is deaper to the east of the volcano rather than to the west, reaching depths of 220 m and 50 m, respectively.

Observing the 1883 caldera is possible to notice that it is principally located to the east of the volcano with its vertical ring faults which reach the Granit basment at a depth of 5000 m. The western fault is positioned at 2520 m from the origin of the section and it coincides with the west side of the magmatic ascent conduit, while the eastern fault is positioned at 5000 m from the same origin. This caldera has a width of 2480 m.

Considering the stratigraphical information obtained from this section, it is possible to observe that in the areas outside of the caldera, which extend from 0 to 2520 m and from 5000 m to 6900 m along the x-axis, there is the same stratigraphical sequence except for the presence of pillow lavas with a variable thickness between 50 m and 25 m at the roof of the western portion. This stratigraphical sequence is composed of 60 m of caldera-forming ignimbrite that is stratigraphically above of 600 m of unconsolidated marines clays which reaches a depth of 660 m. Stratigraphically below there are 3400 m of clay-dominated siliciclastic rocks interbedded with volcanoclastic material which reaches a depth of 4060 m and then, below this layer there are 5000 m of granitic basement which extend to the bottom of the section.

Considering the 1883 caldera, which is between the ring faults explained before, it is possible to notice the presence of the same stratigraphical sequence with the same thicknesess just described but with a difference at the roof of it. Precisely, it is possible to observe the presence of 50 m of pillow lavas which are stratigraphically above of 230 m of caldera-forming ignimbrite. This material is mostly deposited inside of the caldera rather than in the external areas, reaching thickneses almost 5 times greater.

The caldera-forming ignimbrite fills the entire caldera reaching both the ring faults. It is important to notice that the entire stratigraphical sequence inside of the caldera was lowered by 300 m due to the displacement along the ring faults except for the caldera-forming ignimbrite and for the pillow lavas which are at the roof of the sequence. The caldera-forming ignimbrite was deposited during the strong activity associated with the 1883 eruption and the pillow lavas are post-calderic materials that are located only below the volcano, constituting the last deposited materials which have welded the caldera.

In conclusion, a simplified vertical magmatic plumbing system was represented which is originates from a small reservoir located at a depth between 5000 m and 5500 m. This magmatic conduit develops until it reaches the summit of the volcano and it is positioned in contact with the western ring fault of the caldera.
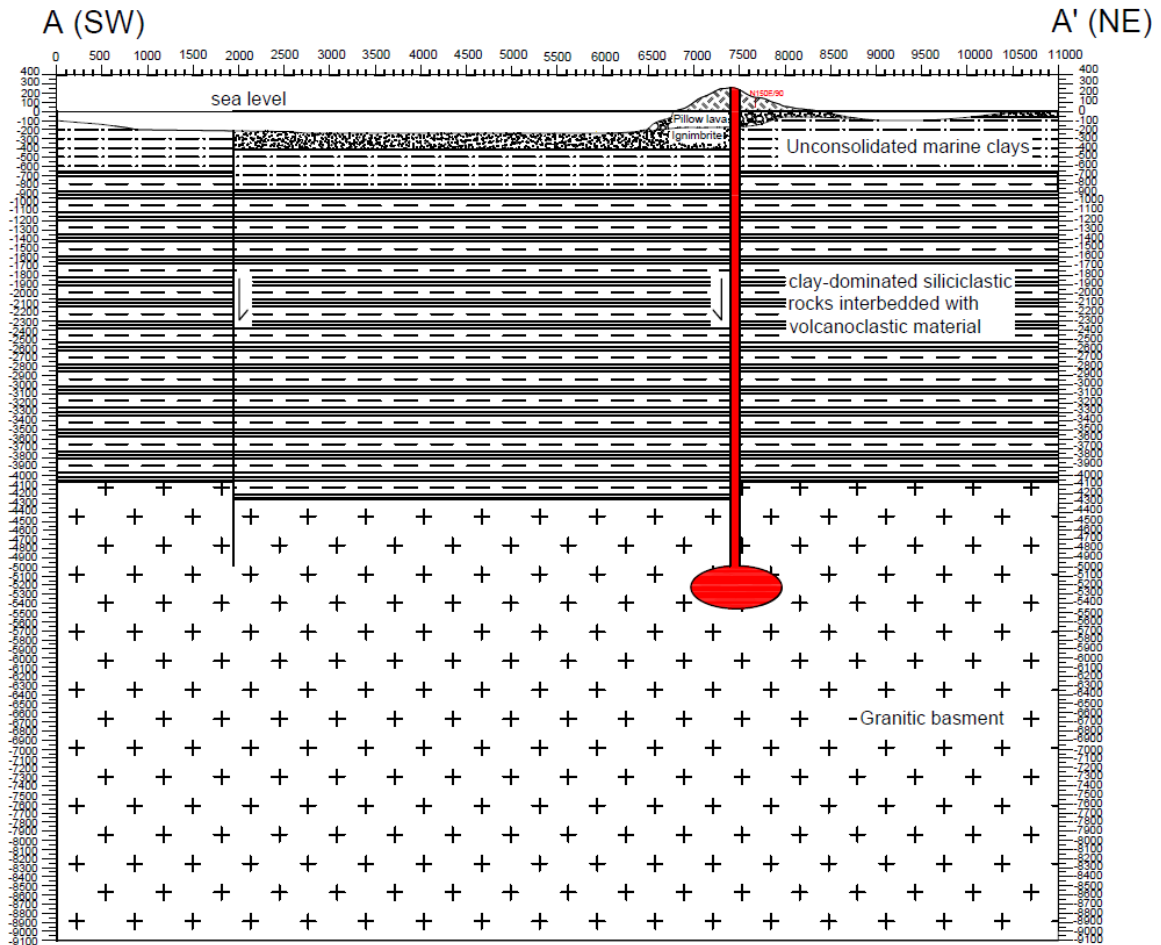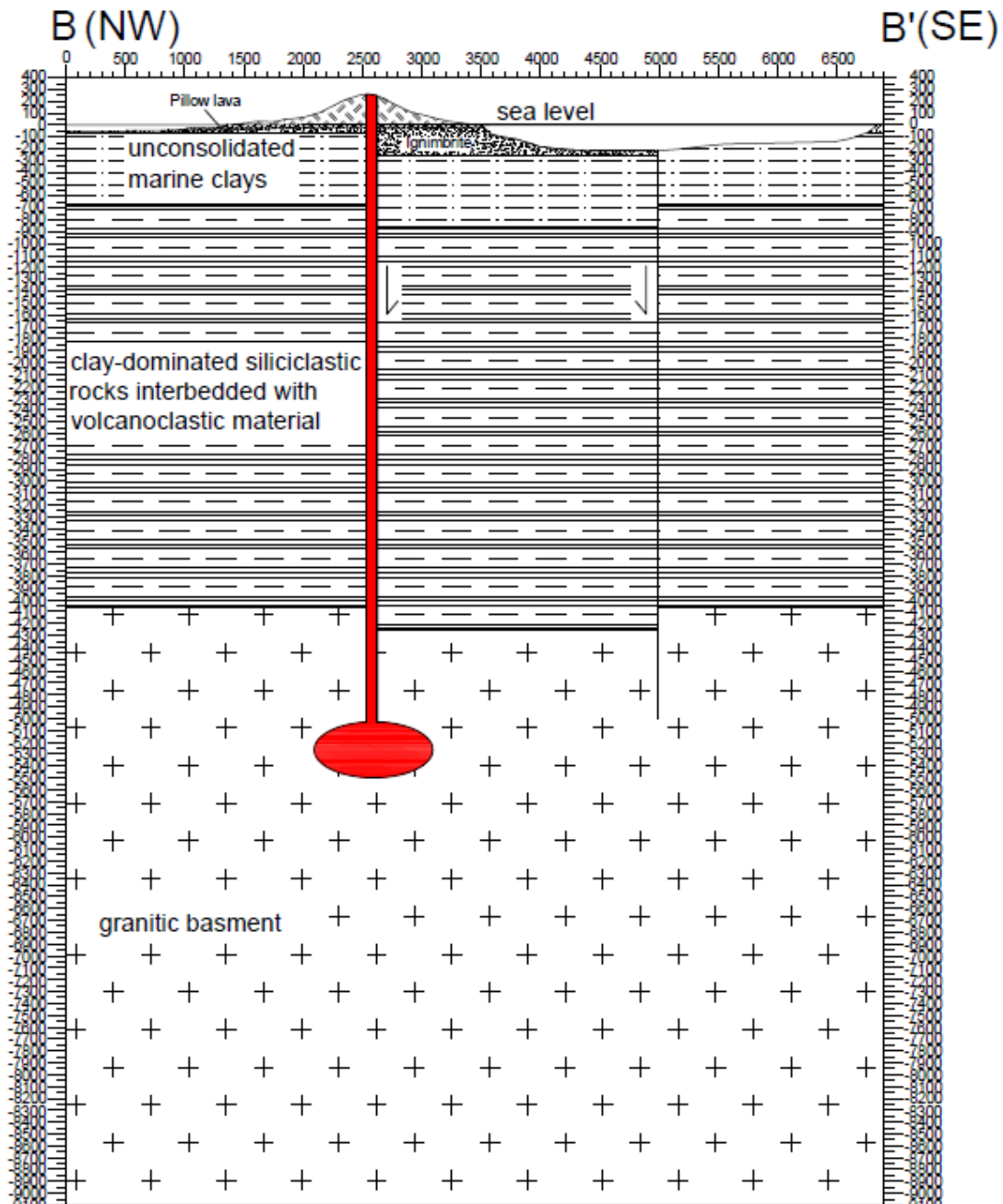

Figure 46: *Conceptual geological cross-section (B-B') of Anak Krakatau. Distances and depths are represented in meters.*

6.5.2 Pre-collapse 3D model

Once the geological cross sections were obtained, it was possible to extrapolate all the geological, geometric, structural and stratigraphical data necessary for the reconstruction of the area that was present before the sector collapse. The information obtained were included in the model in order to be able to carefully show the conditions and characteristics that were present before the collapse and thus be able to accurately reconstruct the analyzed area.

Considering the 3D model of Anak Krakatau, it is possible to observe the emerged and submerged pre-collapse topographic surface, the pre-collapse stratigraphy with its stratigraphic relationships and the position and shape of the 1883 caldera with its ring faults (figure 47a). The topographic surface represents the emerged and submerged areas of the Krakatau archipelago and it was obtained as explained above allowing to observe the pre-collapse situation. Considering the stratigraphic sequence, it is possible to notice that it represents what has been obtained from the geological cross-sections but with small variations due to the limitations imposed by the software used for the realization of the model. These variations concern the lack of the 60 m of caldera-forming ignimbrite positioned outside the 1883 caldera and therefore a slightly greater thickening of the unconsolidated marine clays which reach a maximum thickness of 660 m in the areas where they reach the sea level.

Observing the 1883 caldera, it is possible to notice that it reaches a granite basement and observing its plane view, it is possible also to notice that it intersects the volcano delimiting the area subsequently collapsed. In addition, for a better consideration of the conditions that were present before the collapse, a portion of 104m was represented inside the caldera. This volume allows to differentiate the mechanical properties of the materials present inside and outside the caldera, considering the lower values for the portions of materials that were translated along the ring faults. Finally, considering the entire stratigraphical sequence inside of the caldera is possible to notice that it is lowered by 300m due to the displacement along the ring faults except for the caldera-forming ignimbrite and for the pillow lavas which are at the roof of the sequence (Figure 47b).
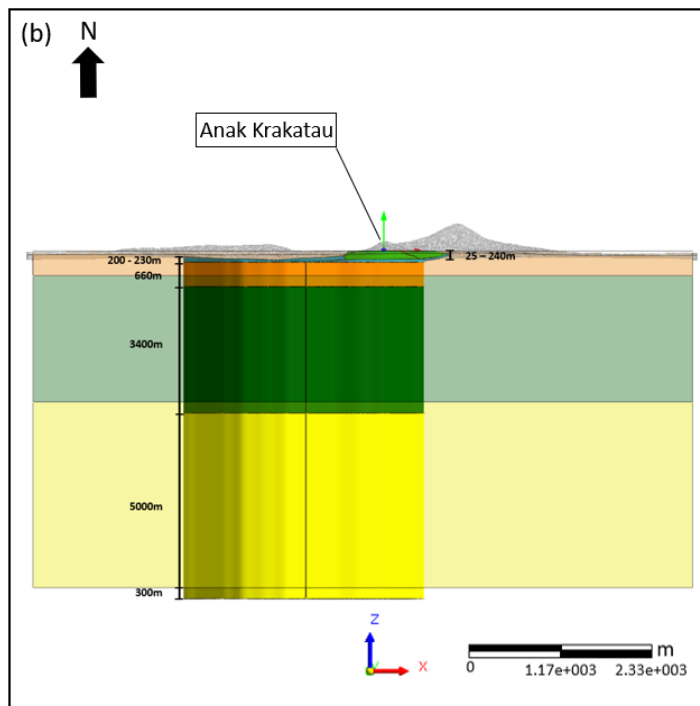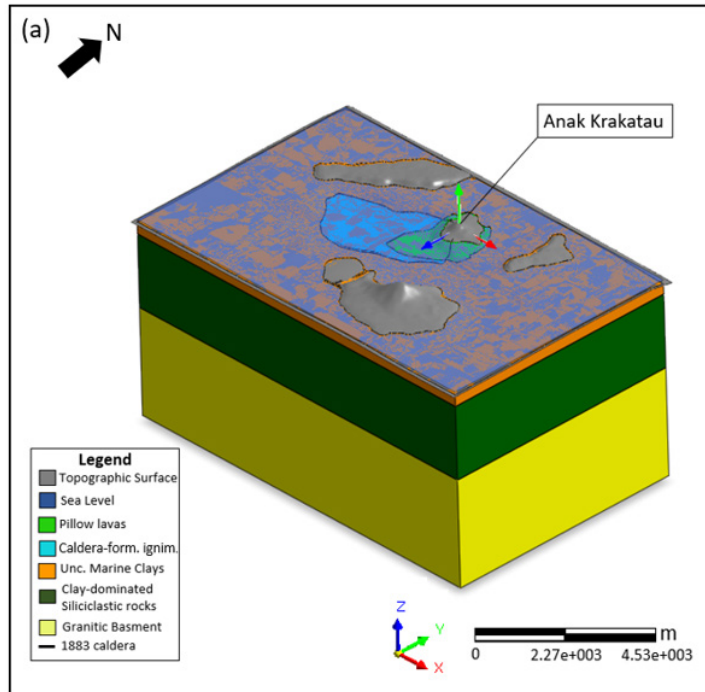
Figure 47: *2018 Pre-collapse 3D model; (a), view of the Krakatau archipelago, the stratigraphy and the 1883 caldera (Black solid line); (b), Front view of the 1883 caldera and of the stratigraphic sequence lowered by 300 m due to the displacement along the ring faults except for the caldera-forming ignimbrite and for the pillow lavas.*

7 Discussion

Some important aspects highlighted through the elaboration of the collected data will be discussed in this chapter. The thermal and Sulfur dioxide emission data with particular attention for the months preceding the sector collapse will be analyzed in detail. Successively, the positions and the strikes of the fractures and the migration of the summit crater will be also analyzed and finally, the 2018 pre-collapse models will be discussed in order to demonstrate the importance of the model and its usefulness. The whole project was carried out in order to observe if there were any relations between the volcanic activity and the evolution/modification of the volcanic edifice with the destabilization of the Southwest flank of the cone that culminated in the lateral collapse. It is important to explain that in the discussion phase comparisons will be made between our data and our hypothesis with those of other authors in order to find the best explanation of the phenomena that led to the current configuration of the volcanic edifice in exam.

From the analysis of 1221 thermal data and 1156 sulfur dioxide (SO_2) emission data collected by MODIS and OMI on Anak Krakatau, we conclude that the volcano started to increase its activity several months before the sector collapse that occurred on 22 December 2018. Considering the graph shown above (Figure 38) it is possible to observe that from 30 June 2018 the beginning of the new greatest activity phase of the volcano was recorded which continued through the six months that preceded the lateral collapse, reaching its climax in September. Indeed, from September to December 2018 the activity followed a general decreasing trend. This increment of the volcanic activity of Anak Krakatau which is shown by the thermal and SO_2 emission data analyzed, is perfectly compatible with the lava flows identified in this thesis work through the use of PlanetScope images, a new remote sensing technique which is based on the use of satellite images acquired from a constellation of over 150 CubeSats (Doves). Precisely, seven of the eight lava flows mapped and shown in this project occurred between July and November 2018, exactly in the months that preceded the sector collapse. The consideration of what has been explained allowed us to understand that Anak Krakatau showed clear signs of elevated volcanic activity

associated with important effusive eruption events during the whole period preceding the collapse. In other words, the volcano started a new important phase of evolution and modification of the entire volcanic edifice from several months before the collapse, influencing the balance and therefore the stability of the cone.

The results obtained during our work and just explained are supported by the analyzes performed by (Walter et al., 2019) which in a very recent work analyzed the thermal activity of Anak Krakatau in the period between 2000 and 2019, showing an important increase in the thermal activity of the volcano in the months preceding the sector collapse and showing also the climax of the new eruptive phase which was recorded in late September 2018.

Analyzing the lava flows identified, it was possible to observe that almost all these events developed along the southwest, south-southwest ad south slopes of the volcanic cone. The generation of these lava flows created an expansion of the coastline towards southwest and they created an increase in the lithostatic load on the slopes affected by these events which may have favored the destabilization of the southwest flank and the consequent sector collapse. Precisely, the deposited volume on that slopes are equal to $6.8 \times 10^6 \, m^3$. Instead, considering the total issued lava flows' volume, it results equal to $8.2 \times 10^6 \, m^3$. This value does not include all products erupted and deposited on the slopes of the volcanic cone during the recent eruption phase. Instead, (Walter et al., 2019) estimated the total eruptive volume trough the analysis of the thermal data, indicating that this eruption phase produced $25.5 \pm 8.4 \, Mm^3$ of deposits from June 2018 to just prior to the sector collapse event. Considering all this information, considering that the southwest side of the volcano has an average inclination of 22° and considering that from the base of the 1883 caldera to the top of the volcano the slope reaches an average value of 29°, we propose that this strong activity has favored a rapid development of the volcanic building, increasing the lithostatic load on a slope with high inclination (>20°). This increase of the lithostatic load may has favored the achievement of a critical stability condition of the southwest volcanic side. What has been observed is a common condition for triggering slope failures (Keating et al., 2000).

Another important aspect of this work was the analysis of the evolution of Anak Krakatau in detail from 1/01/2016 to 02/28/2019 using all acquired PlanetScope images. This new remote sensing method, recently using also by other authors (Aldeghi et al., 2019), allowed to carefully analyze the morphological and structural changes of the whole volcanic edifice with particular attention for the months that preceded the sector collapse. This step of the project was performed to try to understand if there were any precursor processes of the instability of the southwest flank of the volcano in the months prior to the event and therefore if the collapse could be anticipated. This idea was supported through the consideration that the destabilization of all or part of a volcanic edifice may be achieved over a period of weeks to months or may develop over thousands or tens of thousands of years (McGuire, 1996).

As explained above, all the craters with elongated shapes and the fractures that developed on Anak Krakatau were identified and they were mapped through the use of chromatic scales in order to allow us to obtain their spatial and their temporal evolution during the analyzed period (Figure 42, 43). During the analysis was observed a continuous shift and modification of the position and shape of the summit crater and the creation of extensional fractures only on the upper portion of the volcanic cone. Both these events were identified within the period of the greatest volcanic activity shown by the MODIS-OMI graph.

Observing the craters generation timeline, it is possible to notice an increase in the modification and shifting of the summit crater since June 2018. Precisely, the formation of one crater per month was observed in the months preceding the collapse. This underlines a rapid increase of the morphological changes of the volcano indicating a possible local instability of the summit area. This analysis is supported by (McGuire, 1996) which proposed that the development of instability and the potential subsequent failure is present at all types of volcano by the fact that actively growing edifices experience continuous changes in morphology, with the endogenetic (by intrusion) and/or andexogenetic (by extrusion) addition of material leading to oversteepening and overloading at the surface.

Considering the spatial evolution of the summit crater it is possible to observe that almost all the selected craters developed on the southwest portion of the volcanic cone which successively collapsed. For us this behavior indicates an instability of the Southwest flank of the volcano. This is supported by (van Wyk de Vries et al., 1997) which proposed that it is possible to identify a sector collapse if morphology and structures indicate one preferred spreading direction and if signs of the movement are observed.

Considering the fractures generation timeline, it was possible to notice that from July to August 2018 the number of fractures has gradually increased. This temporal sequence shows that the beginning of the fractures' development coincides with the months of the maximum activity of Anak Krakatau which preceded the lateral collapse. Instead, observing the spatial evolution of the fractures, it is possible to notice that all the fractures have developed on the summit part of the volcanic cone with non-constant strikes due to two principal factors: (1), the intersection of a fracture with a conical surface could generate an irregular trace (topographic effects); (2), the local heterogeneities of the volcano can influence the regular development of the structures. Considering their strikes, the fractures can be divided in three main groups: northwest-southwest; east-west and north-northeast-south-southwest. The fractures with northwest-southeast strike agree with the regional strike indicating that they were generated from the regional tectonic and therefore they played an important role in the collapse control (Tibaldi, 1995). Instead, the fractures with east-west and north-northeast-south-southwest strikes delimit the collapsed area, indicating the presence of an incipient collapse as demonstrated by the interferometry obtained by (Walter et al., 2019) which shows different velocities within the unstable area. In addition, considering their positions and their strikes is also observable that they identify the caldera which is under the volcanic building. All this information allowed us to propose that the southwest flank of the volcano was subjected to instability and extensional forces due to possible sliding along a failure plane from the months prior to the collapse. This idea agrees with what was proposed by (McGuire, 1996), which said that the detached area and the remainder of the edifice is typically marked by incipient or open fractures.

In conclusion, the configuration observed and just explained suggests that there were evident indicators of an instability of the southwest side of the volcano that subsequently collapsed. The sector collapse could be effectively anticipated by continuously monitoring of the various stages of volcanic evolution through the use of different remote sensing techniques currently available. Techniques that are very important to provide crucial and unique observations useful to identify pre-eruptive, syn-eruptive and post-eruptive signals (Pyle at al., 2013).

Finally, considering the 3D model created, it is important to note that it is the first pre-collapse 3D geological model of the Krakatau archipelago that shows the geological setting and the conditions that were present before the sector collapse which occurred on 22 December 2018. The model represents the pre-collapse stratigraphic sequence in detail with its stratigraphic relationships, the position and geometry of the 1883 caldera with its ring faults and the position and shape of Anak Krakatau before the event. This model was created in order to accurately reconstruct the studied area and therefore in order to obtain a key element for a future modeling of the occurred sector collapse. We believe that the generation of this accurate 3D model of the analyzed area is essential to allow the simulation of the 2018 sector collapse that occurred in order to understand the causes that allowed the development of the event.

In this project, the simulation of the collapse and therefore the definition of the factors that caused the event remain to be tested but, considering our data we propose three ideas related to the possible predisposing causes of the collapse which can be tested using our 3D model; these are:

1) The first possible trigger factor of the sector collapse is the increase of the lithostatic load on the southwest volcanic side, due to the deposition of the lava flows and of all products generated during the last phase of the volcano's activity, considering also its high inclination (>20°).

2) The second possible trigger factor of the sector collapse is related to the high magmatic activity which may have generated the intrusion of a dike into the shallow portion of the volcanic edifice.

3) The third possible trigger factor of the sector collapse is related to the external factors which are common predisposing causes that influence the stability of the volcanic slopes such as a failure plane, zones of weakness, hydrothermal activity and mechanical weakening by alteration.

The first hypothesis proposed is supported by a recent work published by (Walter et al., 2019). For these authors, the strong activity that preceded the sector collapse could have influenced the stability of the volcanic edifice. We are in agreement with this idea and we propose also that this increase of the lithostatic load, shown also by a coastline expansion towards SW, may have destabilized the southwest flank of Anak Krakatau, considering also its high inclination; unfavorable condition for slope stability.

The second hypothesis proposed is supported by (Tibaldi, 2001 and Acocella, 2005), which indicated that a dike intrusion is a common trigger of the sector collapses for basaltic volcanoes. Considering the strong volcanic activity recorded in the months preceding the collapse, we propose that an intrusion of a dike could have occurred. The dike, disturbing the states of stress inside the volcano, could have influenced the stability of the southwest slope of Anak Krakatau, which considering its precarious stability, could have reached the collapse condition. The consideration of the magmatic plumbing system within the model could be a key element to test this hypothesis.

The last hypothesis is supported by studies performed by several authors like (Delaney., 1992; Cecchi et al., 2004; Keating et al., 2000 and Paris, 2015). For these authors the stability of the volcanic slopes can also be influenced by external factors. We agree with this idea and analyzing our data we do not rule out that the collapse may have been triggered by external factors such as failure plane or by other causes such as zone of weakness, pore pressure changes, hydrothermal activity, and mechanical weakening by alteration which they are not related to the eruptive activity of Anak Krakatau.

8 Conclusion

Considering the data collected within the temporal interval between 1/01/2016 to 02/28/2019 and considering the data processing performed during this thesis work, it is possible to conclude that:

- From the analysis of 1221 thermal data (MODIS) and 1156 sulfur dioxide emission data (OMI), it was possible to observe that Anak Krakatau began a new and intense activity phase starting from 30 June 2018 which ended shortly after the collapse.

- Analyzing the thermal activity of the volcano and the PlanetScope images, eight lava flows were identified, seven of which occurred from 12 July 2018 to 21 October 2018 in agreement with the new and intense activity phase recorded. These lava flows mainly affected the southwest, south-southwest and south volcanic slopes, generating a volume equal to 6.8×10^6 m^3 and therefore a lithostatic load on the area subsequently collapsed.

- The remote sensing techniques used, allowed to identify for the first time the presence of precursor processes of the sector collapse which were observed within the period of the maximum volcano activity. Continuous monitoring of the various stages of evolution could have effectively anticipated the collapse.

- The accurate model generated is the first 2018 pre-collapse 3D model of Anak Krakatau which allows to simulate the sector collapse that occurred in order to understand the predisposing causes that influenced it. This model allows to test three hypotheses of possible predisposing causes of the collapse. These are:

1) The increase of the lithostatic load on the southwest volcanic side, due to the deposition of all products generated during the last phase of the volcano's activity, considering also its high inclination (>20°).

2) The high magmatic activity which may have generated the intrusion of a dike into the shallow portion of the volcanic edifice.

3) External factors which are common predisposing causes that influence the stability of the volcanic slopes such as a failure plane, zones of weakness, hydrothermal activity and mechanical weakening by alteration.

The study shows that the 2018 sector collapse of Anak Krakatau could have been anticipated monitoring the volcano and its activity through the use of different remote sensing techniques. Finally, we believe that the combination of 3D models, representing areas with signs of instability, and remote sensing techniques is an important method for predicting potentially disastrous events.

9 References

Abdurrachman, M., Widiyantoro, S., Priadi, B., Ismail, T. (2018) - Geochemistry and Structure of Krakatoa Volcano in the Sunda Strait, Indonesia. *Geosciences, Vol 8, pp. 111.*

Acocella, V. (2005) - Modes of sector collapse of volcanic cones: Insights from analogue experiments. Jour. OF Geophy. Res., VOL. 110.

Aldeghi, A., Carn, S., Escobar-Wolf, R., and Groppelli, G. (2019) - Volcano Monitoring from Space Using High-Cadence Planet CubeSat Images Applied to Fuego Volcano, Guatemala. Remote Sens. Vol.11, pp. 2151.

Allard, P., Jehanno, C., Sabroux, J-C. (1981) - Composition chimique et isotopique des produits gazeux et solides de l'activité éruptive du Krakatau (Indonésie) pendant la période 1978-1980. *C.R. Acad. Sci. Paris, 293 (II), pp. 1095-1098.*

Bani, P., Normier, A., Bacri, C., Allard, P., Gunawan, H., Hendrasto, M., Surono, Tsanev, V. (2015) - First measurement of the volcanic gas output from Anak Krakatau, Indonesia. *J. Volcanol. Geoth. Res. Vol. 302, pp. 237-241.*

Baroux, E., Avouac, J.-P., Bellier, O., Sèbrier, M. (1998) - Slip-partitioning and fore-arc deformation at the Sunda-Trench, Indonesia. *Terra Nova, Vol. 10, No. 3, pp. 139 – 144.*

Blake, S. (1984) - Volatile saturation during the evolution of silicic magma chambers as an eruption trigger. J. Geoph. Res., Vol.89, pp. 8237-8244.

Camus, G., Vincent, P.M. (1983a) - Discussion of a new hypothesis for the Krakatau volcanic eruption in 1883. *J. Volcanol. Geotherm. Res., Vol.19, pp. 167-173.*

Camus, G., Vincent, P. (1983b) - Un siècle pour comprendre l'éruption du Krakatao. La Recherche, 149, pp.1452-1457.

Camus, G., Gourgaud, A., Vincent, P.M. (1987) - Petrologic evolution of Krakatau (Indonesia): implications for a future activity. *J. Volcanol. Geoph. Res., Vol.33, pp. 299-316.*

Camus, G., Diament, M., Gloaguen, M., Provost, A., Vincent, P.M. (1992) - Emplacement of a debris avalanche during the 1883 eruption of Krakatau (Sunda Straits, Indonesia). Geojournal, Vol.28, No.2, pp. 123-128.

Carey, S., Sigurdsson, H., Mandeville, C., Bronto, S. (2000) – Volcanic hazards from pyroclastic flow discharge into the sea: Examples from the 1883 eruption of Krakatau, Indonesia. *Geological Society of America, Special paper, 345.*

Cecchi, E., van Wyk de Vries, B., Lavest, J.M. (2004) - Flank spreading and collapse of weak-cored volcanoes. *Bull. Volcanol. Vol. 67, pp. 72–91.*

Cloetingh, S., Wortel, R. (1986) – Stress in the Indo-Australian plate. *Tectonoph., Vol.132, pp.49-67.*

Curray, J., Moore, D., Lawyer, L., Emmel, F., Raitt, R., Henry, M., Kieckhefer, R. (1979) - Tectonics of the Andaman sea and Burma: Convergent Margins. *AAPG. Mem., Vol.29, pp.189-198.*

Dahrén, B. (2010) - Investigating magma plumbing beneath Anak Krakatau volcano, Indonesia: evidence for multiple magma storage regions. *Master's Thesis, Uppsala University. ISSN 1650–6553, no: 193.*

Dahrén, B., Troll, V.R., Andersson, U.B., Chadwick, J.P., Gardner, M.F. (2010) - Investigating magma plumbing beneath Anak Krakatau volcano, Indonesia: evidence for multiple magma storage regions. *Geoph. Res. Abstr. 12 EGU2010-6934-1.*

Dahrén, B., Troll, V.R., Andersson, U.B., Chadwick, J.P., Gardner, M.F., Jaxybulatov, K., Koulakov, I. (2012) - Magma plumbing beneath Anak Krakatau volcano, Indonesia: evidence for multiple magma storage regions. *Contributions to Mineralogy and Petrology*, Vol.163, No.4, pp. 631-651.

Decker, R.W., Hadikusumo, D. (1961) - Results of the 1960 expedition to Krakatau. *J. Geoph., Res. 66, pp. 3497–3511.*

Delaney, P. T. (1992) - Volcanoes; you can pile it only so high. *Nature Vol. 357, pp. 194–196.*

Deplus, C., Bonvalot, S., Dahrin, D., Diament, M., Harjono, H., Dubois, J. (1995) - Inner structure of the Krakatau volcanic complex (Indonesia) from gravity and bathymetry data. *J. Volcanol. Geotherm. Res. 64, pp. 23-52.*

Diament, M., Deplus, C., Harjono, H., Larue, M., Lassal, O., Dubois, J., Renard, V. (1990) - Extension in the Sunda Strait (Indonesia): a review of the Krakatau programme. *Oceanol. Acta, Vol. 10, pp. 31-42.*

Diament, M., Harjono, H., Karta, K., Deplus, C., Dahrin, D., Zen Jr, M.T., Gérard, M., Lassal, O., Martin, A., Malod, J. (1992) – Mentawai fault zone off Sumatra: A new key to the geodynamics of western Indonesia. *Geology, Vol.20, pp. 259-262.*

Engdahl, E.R., Van der Hilst, R., Buland, R. (1998) - Global Teleseismic Earthquake Relocation with Improved Travel Times and Procedures for Depth Determination. *Bull. Of the Seismol. Society of America, Vol. 88, No. 3, pp. 722-743.*

Engdahl, E.R., Villasenor, A., DeShon, H.R., Thurber, C.H. (2007) - Teleseismic Relocation and Assessment of Seismicity (1918–2005) in the Region of the 2004 Mw 9.0 Sumatra–Andaman and 2005 Mw 8.6 Nias Island Great Earthquakes. *Bull. Of the Seismol. Society of America, Vol.97, No. 1A, pp. S43–S61.*

Escher, B.G. (1919) - Veranderingen in de Krakatau groep na 1908. *Handelingen Eerste Ned. Ind. Natuurw. Congres- Weltevreden.*

Escher, B.G. (1928) - Krakatau in 1883 en in 1928. Tijds. Kon. Ned. Aardr. Genoot., 45,4, pp.715-743, 2 maps.

Escher, B.G. (1931b) - Gloedwolken en lahars. Vulkanische katastrophes in Nederlandsch-Indië. Tropisch. Nederl., 3,19, pp. 291-304; 3,20, pp. 307-320.

European Commission Joint Research Centre. (2018) - Indonesia - Volcanic Eruption & Tsunami. *GDACS Volcano RED Alert, JRC Emergency Reporting – Activation, No. 029.*

Fisher, R. V. (1979) - *J. Vo/can. geotherm. Res. 6, pp. 305-218.*

Francis, P. W., Self, S. (1983) - The eruption of Krakatau. *Sci. Amer., Vol. 249, pp. 172-187.*

Gardner, M.F., Troll, V.R., Hart, G., Gamble, J.A., Ellam, R.M., Wolff, J.A., Gertisser, R. (2007) - Shallow-level processes at Krakatau volcano: crystallization and late stage crustal contamination. *Geoph. Res. Abstract, EGU meeting Vienna, Austria, EGU07-A-08469.*

Gardner, M.F., Troll, V.R., Gamble, J.A., Gertisser, R., Hart, G.L., Ellam, R.M., Harris, C., Wolff, J.A. (2012) - Crustal Differentiation Processes at Krakatau Volcano, Indonesia. J. of Petrol., Vol. 54, No. 1, pp. 149 – 182.

Giacchetti, T., Paris, R., Kelfoun, K., Ontowirjo, B. (2012) - Tsunami hazard related to a flank collapse of Anak Krakatau Volcano, Sunda Strait, Indonesia. *Geological Society, London, Special Publications, 361, pp. 79–90.*

Google Earth. *Available online: (https://www.google.com/earth/).*

Grilli, S.T., Tappin, D.R., Carey, S., Watt, S.F.L., Ward, S.N., Grilli, A.R., Engwell, S.L., Zhang, C., Kirby, J.T., Schambach, L., Muin, M. (2019) - Modelling of the tsunami from the December 22, 2018 lateral collapse of Anak Krakatau volcano in the Sunda Straits, Indonesia. Scientific Reports, Nature Res. *9, 11946.*

Hall, R. (2009) - Indonesia, Geology. *Royal Holloway University of London.*

Hamilton, W. (1979) - Tectonics of the Indonesian region. *US Geologic. Survey Prof. Paper 1078.*

Harjono, H. (1988) - Géodynamique du Détroit de la Sonde (Indonésie): Apports des données de microsismicité et implications volcanologiques. *Thesis, Univ. Pans-Sud, pp. 262.*

Harjono, H., Diament, M., Nouaili, L., Dubois, J. (1989) - Detection of magma bodies beneath Krakatau volcano (Indonesia) from anomalous shear waves. *J. Volcanol. Geotherm. Res. 39, pp. 335–348.*

Harjono, H., Diament, M., Dubois, J., Larue, M. (1991) – Seismicity of the Sunda Strait: Evidence for Crustal Extension and Volcanological Implications. *Tectonics, Vol. 10, No. 1, pp. 17-30.*

Huchon, P., LePichon, X. (1984) - Sunda Strait and Central Sumatra Fault. *Geology, Vol.12, pp. 668-672.*

Jarrard, R.D. (1986 a) – Terrane motion by strike-slip faulting of fore-arc silvers. *Geology, Vol.14, pp. 780-783.*

Jarrard, R.D. (1986 b) – Relation among subduction parameters. *Rew. Geoph. And Space Physics, Vol. 24, pp. 127-284.*

Jaxybulatov, K., Koulakov, I., Seht, M.I., Klinge, K., Reichert, C., Dahren, B., Troll, V.R. (2011) - Evidence for high fluid/melt content beneath Krakatau volcano (Indonesia) from local earthquake tomography. *J. Volcanol. Geotherm. Res. 206, pp. 96–105.*

Judd, J.W. (1888) - On the volcanic phenomena of the eruption, and distribution of the ejected materials, In: G.J. Symons (ed.), The eruption of Krakatoa, and subsequent phenomena. pp. 1-56.

Katili, J.A., Hehuwat, F. (1967) - On the occurrence of large transcurrent faults in Sumatra, Indonesia. *J. Geoscience Osaka City university, Vol. 10, pp. 5-17.*

Keating, B.H., McGuire, W.J. (2000) - Island Edifice Failures and Associated Tsunami Hazards. Pure appl. *geophys. Vol. 157, pp. 899–955.*

Kopp, H., Flueh, E.R., Klaeschen, D., Bialas, J., Reichert, C. (2001) - Crustal structure of the central Sunda margin at the onset of oblique subduction. *Geoph. J. Int., 147, pp. 449-474.*

Krishna, K.S., Gopala, R., Ramana, M.V., Subrahmanyan, V., Sarma, K.V.L.N.S., Pilipenko, A.I., Shcherbakov, V.S., Radhakrishna Murthy, I.V. (1983) - Tectonic model for the evolution of oceanic crust in the northeastern Indian Ocean from the late Cretaceous to the early Tertiary. J. Geophys. Res. B, Vol., 100, pp. 20011–20024.

Lasitha, S., Radhakrishna, M., Sanu, T.D. (2006) - Seismically active deformation in the Sumatra–Java trench-arc region: geodynamic implications. *Current Science, Vol. 90, No. 5.*

Lelgemann, H., Gutscher, M., Bialas, J., Flueh, E., Weinrebe, W., & Reichert, C. (2000) -Transtensional basins in the western Sunda Strait. Geoph. Res., Lett. 27, pp.3545-3548.

Liu, C.S., Curray, J.R., McDonald, J.M. (1983) - New constraints on the tectonic evolution of the eastern Indian Ocean. *Earth Planet. Sci. Lett., Vol., 65, pp. 331–342.*

Lunt, P., Burgon, G., Baky, A. (2009) - The Pemali Formation of Central Java and equivalents: Indicators of sedimentation on an active plate margin. *J. Asian Earth Sci. Vol. 34, pp. 100-113.*

Mader, C.L., Gittings, M.L. (2006) - Numerical Model For The Krakatoa Hydrovolcanic Explosion And Tsunami. *Science of Tsunami Hazards, Vol. 24, No. 3, p. 174.*

Malod, J.A., Karta, K., Beslier, M.O., Zen Jr, M.T. (1995) - From normal to oblique subduction: tectonic relationships between Java and Sumatra. *J. SE Asian Earth Sci., Vol. 12, pp. 85–93.*

Malod, J.A., Kemal, B.M. (1996) - The Sumatra margin: oblique subduction and lateral displacement of the accretionary prism, in Tectonic Evolution of Southeast Asia. *eds Hall, R. & Blundell, D., Geologic. Society. Spec. Publ., Vol. 106, pp. 19–28.*

Mandeville, C.W., Carey, S., Sigurdsson, H.(1996a) - Magma mixing, fractional crystallization and volatile degassing during the 1883 eruption of Krakatau volcano, Indonesia. *J.Volcanol.Geotherm.Res.74, pp.243 -274.*

Mandeville, C.W., Carey, S., Sigurdsson, H. (1996b) - Sedimentology of the Krakatau 1883 submarine pyroclastic deposits. *Bull. Volcanol. Vol.96, pp. 512-529.*

McCaffrey, R. (1991) – Slip vectors and streaching of the Sumatra fore arc. *Geology, Vol. 19, pp. 881-884.*

McCaffrey, R. (2009) – The Tectonic Framework of the Sumatran Subduction Zone. *Annu. Rev. Earth Planet. Sci. 37, pp. 345-66.*

McGuire, W. J. (1996) - Volcano instability: a review of contemporary themes. In Volcano Instability on the Earth and Other Planets (eds. McGuire, W.J., Jones, A.P., and Neuberg, J.) Geol. Soc., London, Spec. Publ. 10, pp. 1-23.

Michel, G.W., Becker, M., Angermann, D., Reiber, C., Reinhart, E. (2000) - Crustal motion in E- and SE-Asia from GPS measurements. *Earth Planets Space, Vol.52, pp. 713–720.*

Minster, J.B., Jordan, T.H. (1978) - Present-day plate motions. *J. geoph. Res. Vol. 83, pp. 5331-5354.*

MODVOLC, near-real-time satellite monitoring of global volcanism using MODIS. *Available online: (http://modis.higp.hawaii.edu/).*

Müller, S. (1844) - Land- en Volkenkunde. In: C.I. Temminck (ed.) Verhandelingen over de natuurlijke geschiedenis der Nederlandsche overzeesche bezittingen, door de leden der Natuurkundige commissie in Indië en andere schrijvers. *S. & J. Luchtmans& C.C. van der Hoek, Leiden.*

Natawidjaja, D.H., Sieh, K. (1994) - Slip-rate along the Sumatra transcurrent fault and its tectonic significance. *Geologic. Society of London.*

Neumann van Padang, M. (1933b) - De Krakatau voorheen en thans. *Tropische Natuur, Vol.22, pp. 137-150.*

Newcomb, K.R., McCann, W.R. (1987) – Seismic history and seismotectonics of the Sunda arc. *J. of Geoph. Res., Vol. 92, pp. 421-439.*

Ninkovich, D. (1976) - Late Cenozoic clockwise rotation of Sumatra. EPSL. Vol.29, pp. 269-275.

Nishimura, S., Nishida, J., Yokoyama, T., Hehuwat, F. (1986) - Neotectonics of the Strait of Sunda, Indonesia. *Jour. SE Asian Earth Sci. 1, 81-91.*

Nishimura, S., Harjono, H. (1992) - The Krakatau Islands: The Geotectonic Setting. *Geojournal 28, pp. 87-98.*

Nomanbhoy, N., Satake, K. (1995) - Generation mechanism of tsunamis from the 1883 Krakatau eruption. *Geoph. Res., Lett., Vol. 22, No. 4, pp. 509-512.*

Noujiam, A. (1976) - Drilling in a high temperature and overpressured area Sunda Straits, Indonesia. *Proc. Fifth Annu. Conv. Indonesian Pet Assoc., Jakarta, pp. 211-214.*

Newcomb, K.R., McCann, W.R. (1987) - Seismic history and seismotectonics of the Sunda arc. J. Geophys. Res., Vol., 92, pp. 421–439.

Oba, N., Tomita, K., Yamamoto, M., Istidjab, M., Badruddin, M., Parlin, M., Sadjiman, Djuwandi, A., Sudradjat, A., Suhanda, T. (1982) - Geochemical study of lava flows, ejecta and pyroclastic flows from the Krakatau group, Indonesia. *Rept. Fac. Sci. Kagoshima Univ. Vol.16, pp. 21-41.*

Oba, N., Tomita, K., Yamamoto, M., Istidjab, M., Badruddin, B., Sudradjat, A., Suhanda, T., Kiyosaki, I., Nakamura, J., Inome, T. (1983a) - Chemical comparison of the 1883 Krakatau pumice flow, Indonesia, and the Ata and Aira "Shirazu" pumice flows, Japan. *Reports Fac. Sci. Kagoshima Univ., 16, pp. 43-54.*

Oba, N., Tomita, K., Yamamoto, M., Istidjab, M., Sudradjat, A., Suhanda, T., Parlin, M., Sadjiman, Djuwandi, A., Notodisuryo, D.N., Sulistiyo, Y., Hariadi, W., Muryowihardjo, S., Kiyosaki, S., Ishii, T., Nakamura, J. (1983b) - Geochemical study of volcanic products, in particular to pumice flows of the Krakatau group, Indonesia. *Reports Fac. Sci. Kagoshima Univ., 16, pp. 21-41.*

Oemaiya D.V., Santoso, D. (2019) - 3D model of Krakatau volcano subsurface structure based on gravity data. *Journal of Physics: Conf. Series, 1242 012049.*
OMI, Global sulfur dioxide monitoring, National Aeronautics and Space Administration (NASA). *Available online:* (https://so2.gsfc.nasa.gov/).

Paris, R., Wassmer, P., Lavigne, F., Belousov, A., Belousova, M., Iskandarsyah, Y., Benbakkar, M., Ontowirjo, B., Mazzoni, N. (2014) - Coupling eruption and tsunami records: the Krakatau 1883 case study, Indonesia. *Bull., Volcanol. Vol. 76, pp. 814.*

Paris, R. (2015) - Source mechanisms of volcanic tsunamis. Philos. Trans. Royal Soc. A, 373.

Planet Team, Planet Application Program Interface: In Space for Life on Earth. San Francisco, CA. 2017. *Available online: (https://api.planet.com).*

Scandone, R. (1990) - Chaotic collapse of calderas. *J. Volcanol. Geotherm. Res., Vol.42, pp.285-302.*

Schluter, H.U., Gaedicke, C., Roeser, H.A., Schreckenberger, B., Meyer, H., Reichert, C. (2002) -Tectonic features of the southern Sumatra-western Java forearc of Indonesia. *Tectonics, Vol. 21, No. 5, 1047.*

Self, S., Rampino, M.R. (1981) – The 1883 Eruption of Krakatau. *Nature, Vol. 294, pp. 699-704.*

Simkin, T., Fiske, R.S. (1983) - Krakatau 1883: The Volcanic Eruption and its Effects. *Smithsonian Inst. Press, Washington, D.C., pp. 464.*

Self, S. (1983) - Large-scale phreatomagmatic volcanism: a case study from New Zealand. *J. Volcanol. Geotherm. Res., Vol.17, pp. 433-469.*

Self, S. (1992) - Krakatau Revisited: The Course of Events and Interpretation of the 1883 Eruption*. GeoJournal, 28.2, pp. 109-121.*

Sieh, K., Natawidjaja, D.H. (2000) – Neotectonics of the Sumatran Fault, Indonesia. *J. of Geoph. Res. Vol. 105, No. B12, pp. 28, 295-28, 326.*

Sigurdsson, H., Carey, S., Mandreville, C., Bronto, S. (1991) - Pyroclastic flows of the 1883 Krakatau eruption. Eos 72,377, pp. 380-381.

Simons, W.J.F., Socquet, A., Vigny, C., Ambrosius, B.A.C., Haji Abu, S., Promthong, C., Subarya, C., Sarsito, D.A., Matheussen, S., Morgan, P., Spakman, W. (2007) - A decade of GPS in southeast Asia: resolving Sundaland motion and boundaries. *J. Geoph. Res. 112, B06420.*

Smithsonian Institution, Recent bulletin report. Bulletin of the Global Volcanism Program*. Available online: (https://volcano.si.edu/volcano.cfm?vn=342090).*

Špičák, Â., Václav, H. & Vaněk, J. (2002) - Seismic Activity Around And Under Krakatau Volcano, Sunda Arc: Constraints To The Source Region Of Island Arc Volcanics. *Stud. geoph. geod., Vol.46, pp. 545-565.*

Stehn, C.E. (1929) - The geology and volcanism of the Krakatau Group. *Proc. Fourth Pacific Sci. Congress (Batavia), pp. 1-55.*

Sudradjat, A. (1982) - The morphological development of Anak Krakatau Volcano, Sunda Strait. *Geology of Indonesia, 9, pp. 1–11.*

Susilohadi, S., Gaedicke, C., Djajadihardja, D. (2009) - Structures and sedimentary deposition in the Sunda Strait, Indonesia. *Tectonoph., Vol.467, pp. 55-71.*

Symons, G.J. (1888) - The Eruption of Krakatoa and Subsequent Phenomena. *Report of the Krakatoa Committee of the Royal Society, pp. 494, Trubner and Co., London.*

Tibaldi, A. (1995) - Morphology of pyroclastic cones and tectonics. *J. Geophys. Res., 100, 24, 521–24, 535.*

Tibaldi, A. (2001) - Multiple sector collapses at Stromboli volcano, Italy: How they work. *Bull. Volcanol., Vol. 63, pp. 112–125.*

Tregoning, P., Brunner, F.K., Bock, Y., Puntodewo, S.S.O., McCaffrey, R., Genrich, J.F., Calais, E., Rais, J., Subarya, C. (1994) – First geodetic measurement of convergence across the Java Trench. *Geoph. Res. Lett., Vol. 21, No. 19, pp. 2135-2138.*

Van Bemmelen, R.V. (1942) - Krakatau. *Bull. East Indian Volcanol. Surv., Vol., 18, pp. 53-60.*

Van Wyk de Vries, B., Francis, P. W. (1997) - Catastrophic collapse at stratovolcanoes induced by gradual volcanic spreading. Nature, Vol. 387, pp. 387–390.

Verbeek, R. D. M. (1884) - The Krakatau eruption. *Nature Vol.30, pp. 10-15.*

Verbeek, R. D. M. (1885) - Krakatau. 2 Vols., Batavia.

Vincent, P. M., Camus, G. (1986) - The origin of the 1883 Krakatau tsunamis, by P.W. Francis. Discussion. J. Volcanol. Geotherm. Res., Vol.30, pp. 169-177.

Walter, T.R., Haghshenas Haghighi, M., Schneider, F.M., Coppola, D., Motagh, M., Saul, J., Babeyko, A., Dahm, T., Troll, V.R., Tilmann, F., Heimann, S., Valade, S., Triyono, R., Khomarudin, R., Kartadinata, N., Laiolo, M., Massimetti, F., Gaebler, P. (2019) - Complex hazard cascade culminating in the Anak Krakatau sector collapse. *Nature Communications, 10, pp. 4339.*

Widiyantoro, S., Van der Hilst, R. (1997) - Mantle structure beneath Indonesia inferred from high-resolution tomographic imaging. *Geoph. J. Int. 130, pp. 167-182.*

Widiyantoto, S., Pesicek, J.D., Thumber, C. (2011) - Subducting slab structure below the eastern Sunda arc inferred from non-linear seismic tomographic imaging. *Geologic. society of London, Vol. 355, pp. 139-155.*

Williams, H. (1941) - Calderas and their origins. *Bull. Dept. Geol. Sci. Vol. 25, pp. 239-346.*

Williams, R., Rowley, P., Garthwaite, M.C. (2019) - Reconstructing the Anak Krakatau flank collapse that caused the December 2018 Indonesian tsunami. *Geology, Vol. 47 No.10, pp. 973–976.*

Wright, R., Blackett, M., Hill-Butler, C. (2015) - Some observations regarding the thermal flux from Earth's erupting volcanoes for the period of 2000 to 2014. *Geoph. Res. Lett., Vol. 42, pp. 282–289.*

Wright, R. (2016) - MODVOLC: 14 years of autonomous observations of effusive volcanism from space. *Geological Society, London, Special Publications, 426.*

Yokoyama, I. (1981) - A geophysical interpretation of the 1883 Krakatau eruption. *J. Volcanol. Geotherm. Res., Vol. 9, pp. 359-378.*

Yokoyama, I. (2014) - Krakatau caldera deposits: revisited and verification by geophysical means. *Annals of Geoph., Vol.57, No. 5, S0541.*

Yokoyama, I. (2015) - Eruption products of the 1883 eruption of Krakatau and their final settlement. *Annals of Geoph., Vol.58, No. 2, S0220.*

Zen, M.T. (1983) - Krakatau and the tectonic importance of Straits Sunda. Bull. Jurusan Geol., Vol.12, pp.9-22.